



IMPLEMENTATION AND ANALYSIS OF GENERALIZED CLOSED-LOOP CONTROLLER ON A GRID FORMING CONVERTER WITH LCL FILTER

Fábio Andrade Leite Alves

Dissertação de Mestrado apresentada ao Programa de Pós-graduação em Engenharia Elétrica, COPPE, da Universidade Federal do Rio de Janeiro, como parte dos requisitos necessários à obtenção do título de Mestre em Engenharia Elétrica.

Orientador: Maurício Aredes

Rio de Janeiro
Junho de 2022

IMPLEMENTATION AND ANALYSIS OF GENERALIZED CLOSED-LOOP
CONTROLLER ON A GRID FORMING CONVERTER WITH LCL FILTER

Fábio Andrade Leite Alves

DISSERTAÇÃO SUBMETIDA AO CORPO DOCENTE DO INSTITUTO
ALBERTO LUIZ COIMBRA DE PÓS-GRADUAÇÃO E PESQUISA DE
ENGENHARIA DA UNIVERSIDADE FEDERAL DO RIO DE JANEIRO COMO
PARTE DOS REQUISITOS NECESSÁRIOS PARA A OBTENÇÃO DO GRAU
DE MESTRE EM CIÊNCIAS EM ENGENHARIA ELÉTRICA.

Orientador: Maurício Aredes

Aprovada por: Prof. Maurício Aredes

Prof. Luís Guilherme Barbosa Rolim

Prof. Pedro Gomes Barbosa

Prof. Bruno Wanderley França

RIO DE JANEIRO, RJ – BRASIL

JUNHO DE 2022

Alves, Fábio Andrade Leite

Implementation and Analysis of Generalized Closed-Loop Controller on a Grid Forming Converter with LCL Filter/Fábio Andrade Leite Alves. – Rio de Janeiro: UFRJ/COPPE, 2022.

XXI, 97 p.: il.; 29, 7cm.

Orientador: Maurício Aredes

Dissertação (mestrado) – UFRJ/COPPE/Programa de Engenharia Elétrica, 2022.

Referências Bibliográficas: p. 80 – 94.

1. Generalized closed-loop controller. 2. Grid forming converters. 3. Virtual impedance. 4. Active resonance damping. 5. Power-flow enhancement. 6. Impedance analysis. I. Aredes, Maurício. II. Universidade Federal do Rio de Janeiro, COPPE, Programa de Engenharia Elétrica. III. Título.

*Dedico este trabalho ao meu pai,
Carlos Luiz Castilho Leite Alves
(in memoriam).*

Agradecimentos

Agradeço à minha mãe, Jeanne, e à minha avó Laura pelo apoio e amor durante todo o caminho trilhado durante o mestrado e na vida. Às minhas irmãs, Carla e Cláudia pelos cuidados e carinho por mim. À minha namorada e companheira Verônica, por todos os bons momentos, amor, e incentivo durante os meses de finalização do trabalho e escrita desta dissertação. À minha família também por todo conforto e torcida durante toda minha trajetória.

Ao meu orientador Maurício Aredes, pela confiança no meu trabalho e todo o apoio institucional e intelectual durante minha caminhada acadêmica. Aos meus amigos do LEMT Thiago Tricarico, Jorge Caicedo, André de Castro, e Marcello Neves por todas as discussões e conselhos para o desenvolvimento desta dissertação. Aos meus companheiros de turma e de mestrado Gustavo Leal, João Adolpho, Leonardo Francisco e Ana Carolina pela companhia e auxílio durante as disciplinas e projetos em que realizamos juntos. À todos os amigos do LEMT e aos bons momentos de descontração que tivemos.

Aos meus amigos da Ilha do Governador Matheus Castro e João Carlos, que com conselhos e risadas me ajudaram a seguir firme neste árduo caminho acadêmico. Às inúmeras pessoas que direta e indiretamente me ajudaram a finalizar esta etapa da minha vida.

A todos vocês, meu mais sincero MUITO OBRIGADO!

O presente trabalho foi realizado com apoio da Coordenação de Aperfeiçoamento de Pessoal de Nível Superior - Brasil (CAPES) - Código de Financiamento 001.

Resumo da Dissertação apresentada à COPPE/UFRJ como parte dos requisitos necessários para a obtenção do grau de Mestre em Ciências (M.Sc.)

IMPLEMENTAÇÃO E ANÁLISE DO CONTROLADOR GENERALIZADO DE
MALHA FECHADA EM UM CONVERSOR FORMADOR DE REDE COM
FILTRO LCL

Fábio Andrade Leite Alves

Junho/2022

Orientador: Maurício Aredes

Programa: Engenharia Elétrica

O aumento da presença de conversores eletrônicos de potência nas redes elétricas devido à fontes de energias renováveis, transmissão HVDC, sistemas de armazenamento de energia, carros elétricos, entre outros, pode reduzir robustez das redes elétricas. Uma forma de combater esse efeito é a utilização de conversores formadores de rede. Diferente das tecnologias mencionadas, que utilizam majoritariamente conversores seguidores de rede, os conversores formadores de rede promovem uma melhora na estabilidade de redes com menor índice de curto-circuito. Dentre as diversas formas de controlá-los, destaca-se o esquema Generalized Closed-Loop Controller (GCC) devido a sua flexibilidade de operação, pois utiliza-se de impedâncias virtuais embutidas como controladores auxiliares. A proposta original baseava o GCC para conversores formadores de rede com filtros LC apenas, porém cada vez mais se utiliza este tipo de conversor com filtros LCL. A proposta desta dissertação é a expansão da teoria do GCC para considerar conversores formadores de rede com filtros LCL. O modelo do GCC e suas impedâncias virtuais são apresentadas e, após isso, as propostas de projeto e aplicação são realizadas. Os resultados de simulação corroboram com as propostas e análises realizadas neste trabalho.

Abstract of Dissertation presented to COPPE/UFRJ as a partial fulfillment of the requirements for the degree of Master of Science (M.Sc.)

IMPLEMENTATION AND ANALYSIS OF GENERALIZED CLOSED-LOOP CONTROLLER ON A GRID FORMING CONVERTER WITH LCL FILTER

Fábio Andrade Leite Alves

June/2022

Advisor: Maurício Aredes

Department: Electrical Engineering

The increased presence of power electronic converters in electrical grids due to renewable energy sources, HVDC transmission, energy storage systems, electric cars, among others, can reduce robustness of electrical grids. One way to mitigate this effect is the use of grid-forming converters. Unlike the technologies mentioned, which use mostly grid following converters, grid forming converters promote an improvement in grid stability with lower short circuit rate. Among the various ways to control them, the Generalized Closed-Loop Controller (GCC) scheme stands out due to its flexibility of operation, as it uses embedded virtual impedance as auxiliary controllers. The original proposal was based on the GCC for grid-forming converters with LC filters only, but this type of converter with LCL filters is increasingly being used. The proposal of this dissertation is to expand the GCC theory to consider grid-forming converters with LCL filters. The GCC model and its virtual impedance are presented, and after that, the design and application proposals are carried out. Simulation results corroborate with the proposals and analysis performed in this dissertation.

Contents

List of Figures	x
List of Tables	xiv
List of Symbols	xv
List of Abbreviations	xx
1 Introduction	1
1.1 Motivation	3
1.2 Objectives	4
1.3 Description of the Following Chapters	5
1.4 Work-related Publications	5
2 Grid Forming Converters and Generalized Closed-Loop Controller	6
2.1 Literature Review on Grid-Forming Converters	7
2.2 The Generalized Closed-Loop Controller	11
2.2.1 The Inner Virtual Impedance	13
2.2.2 The Outer Virtual Impedance	18
2.3 Resonant Controllers Formulation	20
2.3.1 Proportional-Resonant Controller	20
2.3.2 Vectorial Proportional-Integral Controller	22
2.4 The Studied Converter	23
3 Inner Virtual Impedance Design	25
3.1 Inner Virtual Impedance Literature Review	26
3.2 Inner Virtual Impedance Design	28
3.3 Single Loop Voltage Design	32
3.3.1 Reference Generator	35
3.3.2 Capacitor Current Filter	37
3.4 Simulation Results	39
3.4.1 Dynamic Test	40

3.4.2	Power Injection Test	41
3.4.3	Disturbance Rejection Tests	46
3.5	Partial Remarks	49
4	Outer Virtual Impedance Design	51
4.1	Outer Virtual Impedance Literature Review	52
4.2	Methodology	53
4.2.1	Power Flow Analysis	54
4.2.2	Impedance Analysis	55
4.3	Outer Virtual Impedance Design	59
4.4	Simulation Results	65
4.4.1	Power Injection Test	65
4.4.2	Disturbance Rejection Tests	69
4.5	Partial Remarks	76
5	Conclusions	77
5.1	Future Works	78
	References	80
A	Bode Comparison for all of Outer Virtual Impedance	95

List of Figures

2.1	Generic control topology of a GFM converter.	7
2.2	Droop (a) and LPF-Droop (b) control schemes.	8
2.3	Synchronverter (a) and SPC (b) control schemes.	10
2.4	Generic cascaded multi-loop (a) and single-loop (b) block diagrams	11
2.5	Converter topology and its measurements.	11
2.6	GCC scheme for a GFM-LC converter (a) and for a GFL-LCL converter (b).	12
2.7	Studied GCC-GFM-LCL scheme.	13
2.8	Resulting virtual impedance when using inductor current I_L (a) and capacitor current I_C (b).	15
2.9	Complete inner VI control scheme.	15
2.10	LCL filter block diagram.	17
2.11	Thévenin's equivalent for the GCC-GFM-LCL controller	19
2.12	Converter topology.	23
3.1	Complete control diagram with I_C current feedback and V_{grid} feed-forward.	29
3.2	Bode diagram of $G_{LC}(s)$ for different values of H_{int} . As H_{int} decreases, the bandwidth ω_{LC} increases.	29
3.3	Bode diagram of $Z_{LC}(s)$ for different values of H_{int} . As H_{int} increases, the sensitivity for disturbances decreases.	30
3.4	Bode diagram of $G_{LCL}(s)$ for different values of H_{int}	31
3.5	Bode diagram of $Y_{LCL}(s)$ for different values of H_{int}	31
3.6	$G_{LC}(s)$ step response with and without the designed H_{int}	33
3.7	Step response comparison between $G_{LC}(s)$ and $G_{eq}(s)$	33
3.8	Tracking closed-loop Bode diagram for Analytical method (blue), Gao's method (orange) and VPI method (yellow).	35
3.9	Closed-loop converter output impedance Bode diagram for Analytical method (blue), Gao's method (orange) and VPI method (yellow).	36
3.10	Reference generator based on LPF droop controller.	36

3.11	Closed-loop converter with capacitor current filter tracking transfer function Bode diagram for Analytical method (blue), Gao's method (orange) and VPI method (yellow).	38
3.12	Closed-loop converter output impedance with capacitor current filter Bode diagram for Analytical method (blue), Gao's method (orange) and VPI method (yellow).	39
3.13	Thévenin equivalent of the simulated system for the GCC-GFM-LCL converter. The red point shows the location where P_{meas} and Q_{meas} are calculated.	40
3.14	Step response for the designed controllers, where the $V_{C\alpha}$ component is observed in (a) and $V_{C\beta}$ component in (b).	41
3.15	Step response for the designed controllers. The dynamics of $ V_C $ is observed in (a), while in (b) the voltage regulation of the controllers with respect to the reference $ V_{ref} $ is observed	42
3.16	Active (a) and reactive (b) powers injected by the converter during the <i>Power Injection Test</i> with $P_{set} = 1.0$ pu.	43
3.17	Comparison between $ V_C $ dynamics with PR-Analytical in blue, PR-Gao in orange, and VPI in yellow during the <i>Power Injection Test</i> with $P_{set} = 1.0$ pu.	44
3.18	Unfiltered capacitor current (blue) and filtered capacitor current (orange).	44
3.19	Active (a) and reactive (b) powers injected by the converter during the <i>Power Injection Test</i> with $Q_{set} = 1.0$ pu.	45
3.20	Comparison between $ V_C $ dynamics with PR-Analytical in blue, PR-Gao in orange, and VPI in yellow during the <i>Power Injection Test</i> with $Q_{set} = 1.0$ pu. Figure (a) exhibits the whole simulation time, while (b) depicts the voltage dynamics after the reactive step.	46
3.21	Voltage sag responses for the compared controllers, where (a) shows the voltage amplitude $ V_c $ and (b) the phase a I_2 current.	47
3.22	Active (a) and reactive (b) powers dynamics of each controller after the 7% voltage sag.	48
3.23	Frequency droop dynamics (a) for each compared controllers and active power injection responses (b) before and after the 0.3 Hz frequency step.	49
3.24	Frequency step responses for the compared controllers, where (a) shows the voltage amplitude $ V_c $ and (b) the phase a current.	50
4.1	Virtual impedance implementation using current coupling technique.	56

4.2	Area Ω_P where the maximum active power is bigger than P_{demand} (a), and area Ω_Q where the maximum reactive power is bigger than Q_{demand} (b).	60
4.3	Area Ω_{ratio} where the line ratio is greater than 100 (a), and area Ω of possible values that satisfy the constraints.	61
4.4	Closed-Loop poles and zeros from $Z_{cl}(s)$ for the PR-Analytical controller with H_{min} (blue), H_{max} (orange) (a). The zoom in the highlighted area is illustrated in (b)	62
4.5	Closed-Loop poles and zeros from $Z_{cl}(s)$ for the PR-Gao controller with H_{min} (blue), H_{max} (orange) (a). The zoom in the highlighted area is illustrated in (b)	62
4.6	Closed-Loop poles and zeros from $Z_{cl}(s)$ for the VPI controller with H_{min} (blue), H_{max} (orange) (a). The zoom in the highlighted area is illustrated in (b)	63
4.7	Bode diagram for negative (a) and positive (b) frequencies for $Z_{out}(s)$ with H_{min}	64
4.8	Bode diagram for negative (a) and positive (b) frequencies for $Z_{out}(s)$ with H_{min}	65
4.9	Active and reactive dynamics when $P_{set} = 1.0$ pu in steady-state and H_{min} (a) and H_{max} (b) are inserted.	66
4.10	$ V_C $ dynamics when $P_{set} = 1.0$ pu in steady-state and H_{min} (a) and H_{max} (b) are inserted.	67
4.11	Three-phase modulation index m_{abc} with $P_{set} = 1.0$ pu after the insertion of H_{min} for the PR-Analytical (a), PR-Gao (b) and VPI (c) controllers.	67
4.12	Three-phase modulation index m_{abc} with $P_{set} = 1.0$ pu after the insertion of H_{max} for the PR-Analytical (a), PR-Gao (b) and VPI (c) controllers.	67
4.13	Active and reactive dynamics when $Q_{set} = 1.0$ pu in steady-state and H_{min} (a) and H_{max} (b) are inserted.	68
4.14	$ V_C $ dynamics when $Q_{set} = 1.0$ pu in steady-state and H_{min} (a) and H_{max} (b) are inserted.	68
4.15	Three-phase modulation index m_{abc} with $Q_{set} = 1.0$ pu after the insertion of H_{min} for the PR-Analytical (a), PR-Gao (b) and VPI (c) controllers.	69
4.16	Three-phase modulation index m_{abc} with $Q_{set} = 1.0$ pu after the insertion of H_{max} for the PR-Analytical (a), PR-Gao (b) and VPI (c) controllers.	69

4.17	$ V_C $ and I_2 phase a current dynamics when a 7% voltage sag is applied with H_{min} (a) and H_{max} (b).	70
4.18	P_{meas} and Q_{meas} dynamics when a 7% voltage sag is applied with H_{min} (a) and H_{max} (b).	71
4.19	Frequency and P_{meas} after the 0.3 Hz frequency step with H_{min} (a) and H_{max} (b).	71
4.20	$ V_C $ and I_2 phase a current dynamics the 0.3 Hz frequency step with H_{min} (a) and H_{max} (b).	72
4.21	Grid voltage before and after the introduction of the harmonic distortion at 1.35 s.	73
4.22	Three-phase converter voltages V_C before and after the fifth and seventh harmonic distortion addition for the PR-Analytical (a), PR-Gao (b) and VPI (c) controllers with H_{min}	73
4.23	Three-phase converter voltages V_C before and after the fifth and seventh harmonic distortion addition for the PR-Analytical (a), PR-Gao (b) and VPI (c) controllers with H_{max}	73
4.24	Injected active power after the voltage harmonics insertion for H_{min} (a) and H_{max} (b).	74
4.25	Grid voltage before and after the introduction of the harmonic distortion at 1.35 s.	74
4.26	Three-phase converter voltages V_C before and after the fifth and seventh harmonic distortion addition for the PR-Analytical (a), PR-Gao (b) and VPI (c) controllers with H_{min}	75
4.27	Three-phase converter voltages V_C before and after the negative sequence addition for the PR-Analytical (a), PR-Gao (b) and VPI (c) controllers with H_{max}	75
4.28	Injected active power after the voltage unbalance for H_{min} (a) and H_{max} (b).	76
A.1	Bode plot of the $Z_{out}(s)$ for the 27 calculated values of $R_v + j\omega L_v$ with PR-Analytical controller. The blue color means the minimum Z_v , while the red color means the maximum $ Z_v $ value.	95
A.2	Bode plot of the $Z_{out}(s)$ for the 27 calculated values of $R_v + j\omega L_v$ with PR-Gao controller. The blue color means the minimum Z_v , while the red color means the maximum $ Z_v $ value.	96
A.3	Bode plot of the $Z_{out}(s)$ for the 27 calculated values of $R_v + j\omega L_v$ with VPI controller. The blue color means the minimum Z_v , while the red color means the maximum $ Z_v $ value.	97

List of Tables

2.1	Studied converter electrical parameters.	24
3.1	Controller Gains for the <i>LC</i> control Plant.	34
3.2	Simulated grid parameters.	39
4.1	Input values for Outer VI design.	59

List of Symbols

C	Filter capacitor, p. 12
$C(s)$	Single-loop controller transfer function, p. 13
$C_{inner}(s)$	Multi-loop inner controller transfer function, p. 14
$C_{outer}(s)$	Multi-loop outer controller transfer function, p. 14
D_p	Synchronous power control damping constant, p. 10
$G_{LCL_{ind,cap}}(s)$	LCL filter tracking function, p. 18
$G_{LC_{cap}}(s)$	LC filter transfer function using capacitor current feedback, p. 16
$G_{LC_{ind,cap}}(s)$	LC filter transfer function using either inductor or capacitor current feedback, p. 16
$G_{LC_{ind}}(s)$	LC filter transfer function using inductor current feedback, p. 16
$G_{PI}(s)$	PI transfer function, p. 20
$G_{PR}(s)$	Proportional resonant controller transfer function, p. 20
$G_P(s)$	Instantaneous power calculation low-pass filter transfer function, p. 8
$G_{SPC}(s)$	Synchronous power control transfer function, p. 10
$G_{\alpha\alpha}(s)$	Generic α axis self-transfer function, p. 56
$G_{\alpha\beta+}(s)$	Generic backward complex transfer function in $\alpha\beta$ frame, p. 57
$G_{\alpha\beta+}(s)$	Generic forward complex transfer function in $\alpha\beta$ frame, p. 57
$G_{\beta\alpha}(s), G_{\alpha\beta}(s)$	Mutual transfer functions between $\alpha\beta$ axis, p. 56

$G_{\beta\beta}(s)$	Generic β axis self-transfer function, p. 56
$G_{cl_{ind,cap}}(s)$	Closed-loop converter output impedance using either inductor or capacitor current feedback, p. 17
$G_{cl_{ind,cap}}(s)$	Closed-loop tracking transfer function using either inductor or capacitor current feedback, p. 17
$G_{eq}(s)$	Equivalent first order transfer function, p. 32
$H_{ext}(s)$	outer virtual impedance transfer function, p. 13
$H_{int}(s)$	inner virtual impedance transfer function, p. 13
I_1	Converter side current, p. 12
I_C	Filter Capacitor current, p. 12
I_2	Grid side current, p. 12
$I_{int,ref}$	inner multi-loop current reference, p. 14
I_{int}	inner multi-loop current feedback variable, p. 14
$I_{peak,phase}$	Peak phase base current, p. 15
J	Inertia Constant, p. 10
K	Generic first order transfer function final value, p. 21
K_0	Constant gain converter model, p. 12
K_I	Integral controller gain, p. 20
K_{PWM}	PWM gain, p. 15
$K_{decouple}$	Decouple coefficient between P-f and Q-V droops, p. 55
K_{eq}	Equivalent steady state value, p. 32
K_{int}	Internal VI per unit gain, p. 15
K_p	Active power droop constant, p. 7
K_q	Reactive power droop constant, p. 7
K_v	Voltage per unit gain, p. 15
L_1	Converter-side inductor, p. 12

L_2	Grid-side inductor, p. 12
L_g	Grid inductance, p. 39
L_v	Virtual inductance, p. 52, 53
M_f	Virtual mutual inductance, p. 9
P_{demand}	Maximum active power demanded by the grid, p. 55
P_{meas}	Measured instantaneous active power, p. 7
P_{set}	Active power reference, p. 7
P_{sync}	Synchronverter's synthesized active power, p. 9
Q_{demand}	Maximum reactive power demanded by the grid, p. 55
Q_{meas}	Measured instantaneous reactive power, p. 7
Q_{set}	Reactive power reference, p. 7
Q_{sync}	Synchronverter's synthesized reactive power, p. 9
R	Resistance, p. 3
R_1	Converter-side resistance, p. 12
R_2	Grid-side resistance, p. 12
R_g	Grid resistance, p. 39
R_v	Virtual resistance, p. 53
R_v	Virtual resistor, p. 52
T	Generic first order transfer function time constant, p. 21
T_{eq}	Equivalent time constant, p. 32
V_2	Voltage drop at L_2 and R_2 , p. 28
V_C	Filter capacitor voltage, p. 11
V_{PWM}	Voltage signal to be synthesized by the PWM, p. 13
V_{grid}	Grid voltage, p. 12
V_i	Generic voltage signal at the filter terminal, p. 16

V_{max}	Maximum admissible converter voltage magnitude, p. 55
$V_{peak,phase}$	Peak phase base voltage, p. 15
V_{ref}	Reference Voltage Magnitude, p. 7
X_2	L_2 inductive reactance for the fundamental frequency, p. 54
$X_{C,ref}$	Generic control reference variable., p. 13
X_C	Generic control feedback variable., p. 13
X_L	Inductive Reactance, p. 3
X_{ext}	Generic variable used by the outer virtual impedance, p. 13
X_g	L_g inductive reactance for the fundamental frequency, p. 54
X_{int}	Generic variable used by the inner virtual impedance, p. 13
X_v	L_v inductive reactance for the fundamental frequency, p. 54
Y	Line admittance phasor magnitude, p. 54
$Y_{LCL_{ind,cap}}(s)$	LCL filter output admittance, p. 18
$Z_{LC_{cap}}(s)$	LC filter output impedance using capacitor current feedback, p. 16
$Z_{LC_{ind,cap}}(s)$	LC filter output impedance using either inductor or capacitor current feedback, p. 16
$Z_{LC_{ind}}(s)$	LC filter output impedance using inductor current feedback, p. 16
$Z_{ext}(s)$	Resulting impedance due the outer Virtual Impedance, p. 19
$Z_{out}(s)$	Total output impedance of a grid-forming converter with a LCL filter, p. 19
ΔP	Active power difference, p. 7
ΔQ	Reactive power difference, p. 7
ΔV	Voltage difference, p. 7
$\Delta \omega$	Frequency difference, p. 7

Ω_P	Region in the impedance plane where P_{demand} criteria is valid, p. 60
Ω_Q	Region in the impedance plane where Q_{demand} criteria is valid, p. 60
Ω_{ratio}	Region in the impedance plane where line ratio criteria is valid, p. 60
$\langle \cdot, \cdot \rangle$	Internal product, p. 9
ω	Converter frequency, p. 7
ω_0	Resonant controller tuned frequency, p. 20
ω_n	Natural Frequency of a second order system, p. 21
ω_c	Controller bandwidth, p. 21
ω_{set}	Nominal grid frequency ($2\pi \times 60$ rad/s), p. 7
ϕ	Line admittance phasor phase, p. 54
$\tau_P(s)$	Power low-pass filter time constant, p. 8
θ	Converter power angle when the voltage grid is the reference, p. 54
θ_{max}	Maximum admissible power angle, p. 55
θ_{ref}	Reference Power Angle, p. 7
$\underline{u}_{\alpha\beta\pm}$	Generic system input in complex vector form in $\alpha\beta$ frame, p. 57
$\underline{u}_{\alpha\beta\pm}$	Generic system output in complex vector form in $\alpha\beta$ frame, p. 57
ζ	Damping ratio of a second order system, p. 21
e_{sync}	Synchronverter's synthesized internal voltage, p. 9
i_f	Virtual field current, p. 9
$p_{1,2}$	Complex conjugate poles, p. 21
t_s	Settling time, p. 32
$u_{\alpha\beta}$	Generic system input in $\alpha\beta$ frame, p. 56
$y_{\alpha\beta}$	Generic system output in $\alpha\beta$ frame, p. 56

List of Abbreviations

EPE	<i>Empresa de Pesquisa Energética</i> , p. 2
EPS	Electrical power systems, p. 2
ESS	Energy Storage Systems, p. 2
FACTS	Flexible ac transmission systems, p. 53
GCC	Generalized Closed-Loop Controller, p. 4
GFL	Grid-Following, p. 3
GFM	Grid-Forming, p. 3
HVDC	High Voltage Direct Current, p. 3
LCC	Line-Commutated Converter, p. 3
LCL	Inductor-Capacitor-Inductor filter, p. 4
LC	Inductor-Capacitor filter, p. 4
LEMT	Laboratory of Power Electronics And Medium Voltage Applications, p. 4
LPF	Low-pass filter, p. 7
MIMO	Multiple-input and multiple-output, p. 56
PDE	<i>Plano Decenal de Expansão</i> , Ten Year Expansion Plan, p. 2
PI	Proportional Integral Controller, p. 10
PRODIST	<i>Procedimentos de Distribuição de Energia Elétrica no Sistema Elétrico Nacional</i> , p. 37
PR	Proportional Resonant Controller, p. 10
PV	Photovoltaic, p. 2

PWM	Pulse width Modulation, p. 10
SISO	Single-input and single-output, p. 56
SPC	Synchronous power control, p. 10
USA	United States of America, p. 2
VISMA	Virtual synchronous machine, p. 8
VI	Virtual impedance, p. 4
VOC	Virtual oscillator control, p. 10
VPI	Vectorial Proportional-Integral controller, p. 22
VSC	Voltage Source Converter, p. 3

Chapter 1

Introduction

This chapter presents the work's contextualization, explaining introductory concepts and problems that motivated the author. Each chapter is described along with the document organization and the Dissertation's related published papers.

Electrical power systems (EPS) engineers are changing the system' topologies, equipment, protection systems, and control approaches. Motivated mainly by the worldwide race for green and sustainable energy sources, an increasing number of power electronics converters are being connected to PES.

As an example, the connection of solar and wind energy requires the use of power electronic converters for their connection to the utility grid. Countries such as the United States of America (USA) , Germany, Denmark, China and Brazil are exponents in the penetration of renewable energy in their electrical systems.

California and Texas are the states with the highest production of converter-based renewable energy in the USA. California has 14% of the total energy generation from utility-scale photovoltaic (PV) systems, 6% from small-scale PV systems, and 7% from wind power[1]. Texas, in other hand, has most of its converter-based generation from wind power, with aggregate value of 20% of all the state's generation capacity. Together with small and utility-scale PV, the total power generated from these sources amounts to 36 GW, and is expected to increase in the coming years [2].

Germany and Denmark are two European countries known for their high penetration of converters-based renewables in their grids. Germany has 25.5% of their generation compound by wind (17.3%) and PV (7.2%) sources [3]. Denmark has an even bigger percentage of their electricity generation, with 42.5% of wind energy and 2.5% of PV, adding up the total of 45% of converters-based renewable sources [4].

The rapid growth of converter-based generation in China is also an interesting point. In 2018, China noticed a 20% growth in wind power generation from 2017, becoming the largest producer of this energy globally, while PV generation had a 51% growth in the same period [5]. From 2019 to 2020, China saw a 15% growth in wind power and 16.1% in solar generation. China's National Energy Administration sets a goal that wind and solar energies combined become 16.5% of electricity output [6]. New investments in these types of energy are also expected due to the goals imposed for 2030 and 2050 [7].

In the Brazilian case, an increase in the penetration of this type of renewable energy is also predicted. Through the PDE (*Plano Decenal de Expansão*, Ten Year Expansion Plan) 2030 [8], published by EPE (*Empresa de Pesquisa Energética*) , an increase from 15.9 GW to 32.3 GW of wind generation and from 3.1 GW to 8.4 GW of PV generation is estimated. This represents a jump from 9% to 14% and from 2% to 3% the total Brazilian electrical matrix, respectively.

As the use of solar and wind energy grows, energy storage systems (ESS) are needed to mitigate their intermittent generation nature [9]. Battery banks, flywheels, and pumped storage hydropower plants are some examples of ESS that help

to reduce intermittency. The examples mentioned also require power electronics converters for proper operation.

High Voltage Direct Current (HVDC) Transmission also plays an important role in electrical grids with high penetration of power electronics. In the Brazilian scenario, the existing six HVDC links are used for bulk power transmission, in addition to importing power from the asynchronous system in Paraguay. In the Chinese and American cases, HVDC links are also used to connect their multiple asynchronous systems. This technology can also be used to connect Off-Shore wind power plants to the mainland power system. North Sea countries in Europe have plans to interconnect their electrical systems with the various Off-Shore plants via a Multi-terminal HVDC network [10].

The presence of the mentioned technologies indicates that the networks of the future will be dominated by power electronics equipment [11, 12]. Ensuring the stability, reliability and efficiency of both the converters and the network itself is of utmost importance for modern society.

1.1 Motivation

The majority of converters for PV and wind generation, HVDC transmission with both Line-Commutated Converter (LCC) and Voltage Source Converter (VSC) technologies, and battery ESS converters are referred to as Grid-Following (GFL) converters [13]. Excluding the HVDC LCC, which has a different converter topology, VSCs are called this way because they are current-controlled, and therefore can be modeled as a current source with a low admittance in parallel [13–15]. In addition, they use Phase-Locked Loops (PLL) as a synchronization unit for the proper injection of current and powers by the converter.

The GFL converter has the capability to achieve its best performance when connected to strong and stiff grids, i.e., that have high inertia and low equivalent impedance [13–15]. However, with the increased presence of GFL converters, electrical systems are getting lower inertia, weaker, and with a lower X_L/R ratio. It is reported in the literature that GFL converters with PLL connected to weak grids can lead not only to instability, but also to further weakening of the grid where they are connected [11, 15, 16].

Grid-forming (GFM) converters appear as a way to mitigate the problems described above [17]. They originated in the context of isolated grids, where there is no main system that imposes the grid operating voltage and frequency. Therefore, GFM converters take on the task of imposing these parameters [18]. GFL converters are not capable of this duty, since the PLL is responsible for tracking the grid parameters for proper power injection.

GFM converters behave as the dual of GFL: they are voltage controlled and can be modeled as a voltage source with a low output impedance [19]; they have their own synchronization capability, not depending on a PLL for continued operation; and they perform better operating in weak grids [20, 21], and can cause instabilities when connected to stiff grids [22, 23]. However, grid-connected GFM converter technology is not as mature and absorbed by the industry as GFL. The study of GFM control and stability is proving to be a trend of the last 5 years.

The Laboratory of Power Electronics And Medium Voltage Applications (LEMT) has a microgrid to study the different ways of controlling a VSC and the possible interactions of the future grids. The study of GFM converters is also an internal interest.

Among the various types of existing GFM controllers, the Generalized Closed-Loop Controller (GCC) , proposed by He and Li [24], has embedded in its mathematical model the use of virtual impedance (VI) . These VI units are extremely flexible and allow different types of applications, such as resonance damping, change in the X_L/R ratio of the line, negative sequence suppression, fault current limitation, among others [25].

Although He and Li's work proposes the GCC for both GFL converters with LCL filter and GFM converters with LC filter at their terminals, the major focus is on the GFL converter. Also, because it does not discuss GFM converters with LCL filter, the original proposal fails to cover the cases where this specific converter is applied.

1.2 Objectives

The objective of this work is to expand the understanding of GCC applied to GFM converters with LCL filters connected to grid, thus contributing for a better understanding of this control approach, as well as the design of the embedded VI.

To achieve this goal, the mathematical model of the GCC is presented and discussed. The two VI that compose the control scheme, called Inner and Outer VI, are also analyzed, and afterwards, their design is proposed and applied. The impact of different resonant controllers is also studied in this work, as they are directly related to the performance of the GCC as a whole.

The main objectives for the Inner VI is to damp the intrinsic resonances of the LCL filter, and to enable the design of controllers that use the zero-pole cancellation technique. The simulated converter is set up to normal operation, injecting both active and reactive powers. In this way, the intrinsic filter resonance absence is verified in both output current and capacitor voltage. Furthermore, voltage and frequency disturbances are simulated to verify the stiffness of the system.

For Outer VI, improving the reactive power injection of the converter is the goal, using negative values of virtual resistance and inductance. Although these negative impedance are tuned to the system's fundamental frequency, the implementation of this control structure impacts the whole frequency spectrum of the output impedance of the converter. Thus, voltage disturbances as harmonics and unbalances are also tested, in addition to voltage sags and frequency deviations. These sequences of tests and voltage disturbances are applied in order to verify the whole GCC controller.

1.3 Description of the Following Chapters

In Chapter 2 the original modeling proposed in [24] by He and Li is presented. The transfer functions of the model are presented, as well as the controllers that will be compared in a typical power converter. Chapter 3 discusses the proposed design method for the VI responsible for the active damping of the intrinsic resonance of the LCL filter. Simulation results are presented and partial remarks are discussed. Chapter 4 presents the mathematical background and design method for the virtual impedance responsible for improving the power flow of the converter. Simulation results are presented and partial conclusions are discussed. Chapter 5 summarizes the main findings of this dissertation and proposes future work.

1.4 Work-related Publications

During the development of this dissertation, the author published congress and journal articles. The article [26] is part of this dissertation and deals with the design of the Inner VI to be studied. The [27–32] articles have no direct correlation subjects to this dissertation.

Chapter 2

Grid Forming Converters and Generalized Closed-Loop Controller

This chapter presents the mathematical formulation of the GCC. In addition, a literature review on GFM converters and their different types of controls is provided to contextualize the GCC. Finally, the resonant controllers to be compared are described.

2.1 Literature Review on Grid-Forming Converters

As the grids are transforming and modernizing, mainly due to the presence of distributed resources connected by GFL converters, system weakening and a decrease in the total systemic inertia arise. GFM converters emerge as a possible solution to such problems. Several GFM control strategies have been proposed [18, 19, 33], all intended to ensure autonomous load sharing, inertia support, black start, and voltage and frequency regulation [34]. Figure 2.1 illustrates in a generic way the control topology of a GFM converter.

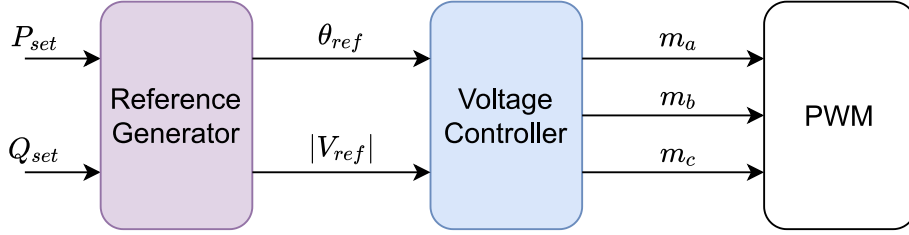


Figure 2.1: Generic control topology of a GFM converter.

The "Reference Generator" block is responsible for generating the references for the voltage controller, providing the reference voltage magnitude $|V_{ref}|$ and power angle θ_{ref} . Ancillary services usually are implemented in this structure.

The most mature way to generate such references is through the Droop controller [35–37], which aims to emulate the load sharing behavior of multiple synchronous generators operating in parallel. The basic equation for this controller is:

$$\begin{cases} \omega - \omega_{set} = -K_p(P_{meas} - P_{set}) \therefore \Delta\omega = -K_p\Delta P \\ |V| - |V_{set}| = -K_q(Q_{meas} - Q_{set}) \therefore \Delta V = -K_q\Delta Q \end{cases} \quad (2.1)$$

Where ω is the frequency of the converter, ω_{set} is the nominal frequency ($2\pi \times 60$ rad/s), K_p is the active power droop constant, P_{meas} is the measured instantaneous active power, and P_{set} is the reference active power set by a higher hierarchical controller. For the second line, $|V_{ref}|$ is the converter reference voltage amplitude, $|V_{set}|$ is the voltage amplitude reference, K_q is the reactive power droop constant, Q_{meas} is the measured instantaneous reactive power, and Q_{set} is the reference reactive power. $\Delta\omega$, ΔP , ΔV , and ΔQ are the difference between the system parameters and the reference values. The resulting θ_{ref} is obtained by integrating the calculated ω :

$$\theta_{ref} = \frac{1}{s}\omega \quad (2.2)$$

This droop implementation has no capability of providing inertial support to the grid. However, by adding a low-pass filter (LPF), an inertia emulation is added in the

droop controller [33, 38]. Furthermore, when an LPF is added in the instantaneous powers calculation, it is possible to remove the oscillatory components of P_{meas} and Q_{meas} that can lead the converter to instability [39]. Figure 2.2 exhibits both Droop control implementations. Rewriting equation (2.1) now with the presence of the LPF:

$$\begin{cases} \omega - \omega_{set} = -K_p G_P(s)(P_{meas} - P_{set}) \therefore \Delta\omega = -K_p G_P(s)\Delta P \\ |V_{ref}| - |V_{set}| = -K_q G_Q(s)(Q_{meas} - Q_{set}) \therefore \Delta V = -K_q G_Q(s)\Delta Q \end{cases} \quad (2.3)$$

Here $G_P(s)$ is the LPF transfer function for the instantaneous power calculation, where τ_P is the time constant for the power LPF:

$$G_P(s) = \frac{1}{\tau_P s + 1} \quad (2.4)$$

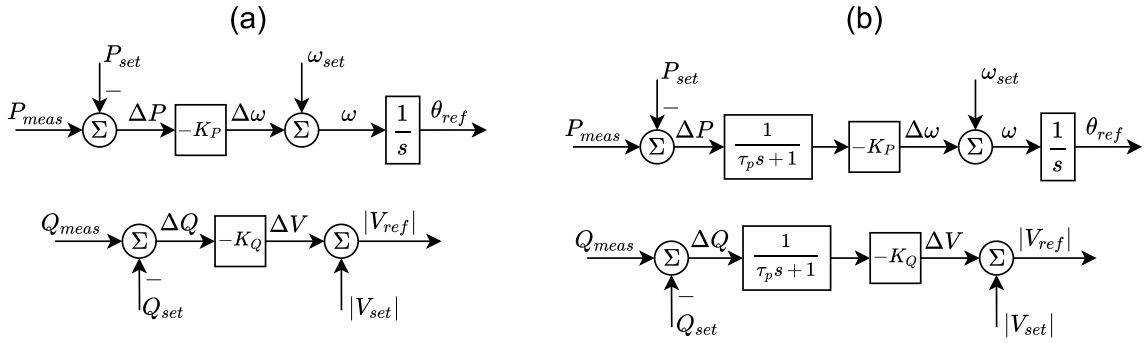


Figure 2.2: Droop (a) and LPF-Droop (b) control schemes.

The droop controller presented here is directly linked with the X_L/R ratio of the system where the converter will be connected. Assuming $X_L/R \approx 100$, characterizing a high voltage transmission system [40], the decoupling between $P - \omega$ and $Q - V$ is true, and there will be no error in the droop controller. However, when the X_L/R ratio decreases, such as medium voltage systems or microgrids, or when the branch impedance are not simplistic, the droop controller $P - \omega$ and $Q - V$ does not perform well. To mitigate this problem, both $P - V$ and $Q - \omega$ droop techniques [41] for mostly resistive networks, and universal droop techniques [42] for different types of grid impedance combinations have been proposed.

A second family of reference generators for GFM takes the next step from droop controllers. While droop controllers seek to emulate the steady-state load sharing behavior of synchronous generators, the so-called synchronous-machine-based control seek to emulate the dynamics of real synchronous generators [18].

First proposed for GFL converters, the virtual synchronous machine (VISMA) fully models a real synchronous machine, taking into account its various armature,

field and damping windings, and other inherent dynamics [38, 43]. This results in a high-order model, which can lead to extremely complex modeling that will not benefit the converter. In [44], VISMA is then proposed for a GFM converter, however the model still remains high order, not bringing benefits when analyzing the system [38].

The Synchronverter controller, on the other hand, is a much more popular implementation than VISMA. Proposed in [45], the Synchronverter uses the electromechanical equations of a two-pole, round rotor synchronous machine to realize the control [46]. As a result, its equivalent model is second-order, in contrast to VISMA's high-order ones, and it is not at risk of causing errors due to complex modeling [38]. In addition, the parameters of virtual inertia, damping, field excitation can be easily tuned and changed in full operation.

The electromagnetic equations of the Synchronverter are:

$$\begin{cases} e_{sync} = \omega M_f i_f \tilde{\sin}\theta & (2.5) \\ P_{sync} = \omega M_f i_f \langle i_{out}, \tilde{\sin}\theta \rangle & (2.6) \\ Q_{sync} = -\omega M_f i_f \langle i_{out}, \tilde{\cos}\theta \rangle & (2.7) \end{cases}$$

Where e_{sync} , P_{sync} and Q_{sync} are, respectively, the internal voltage, active power, and reactive power synthesized by the Synchronverter. They are calculated based on the virtual mutual inductance (M_f), the virtual field current (i_f), and the converter frequency (ω). The output three-phase current i_{out} is represented by a column vector, depicted in (2.8), while $\tilde{\sin}\theta$ and $\tilde{\cos}\theta$ represents, respectively, the sine and cosine column vectors of the three-phase voltage angles of the converter, as can be seen in (2.9) and (2.10). In (2.6) and (2.7), $\langle \cdot, \cdot \rangle$ denotes a internal product.

$$i_{out} = \begin{bmatrix} i_{out,a} \\ i_{out,b} \\ i_{out,c} \end{bmatrix} \quad (2.8)$$

$$\tilde{\sin}\theta = \begin{bmatrix} \sin\theta \\ \sin\left(\theta - \frac{2\pi}{3}\right) \\ \sin\left(\theta + \frac{2\pi}{3}\right) \end{bmatrix} \quad (2.9)$$

$$\tilde{\cos}\theta = \begin{bmatrix} \cos\theta \\ \cos\left(\theta - \frac{2\pi}{3}\right) \\ \cos\left(\theta + \frac{2\pi}{3}\right) \end{bmatrix} \quad (2.10)$$

By combining equations (2.5), (2.6) and (2.7) to the block diagram illustrated in Figure 2.3a (the block named as Electromagnetic Equations), the final synchron-

verter controller is obtained.

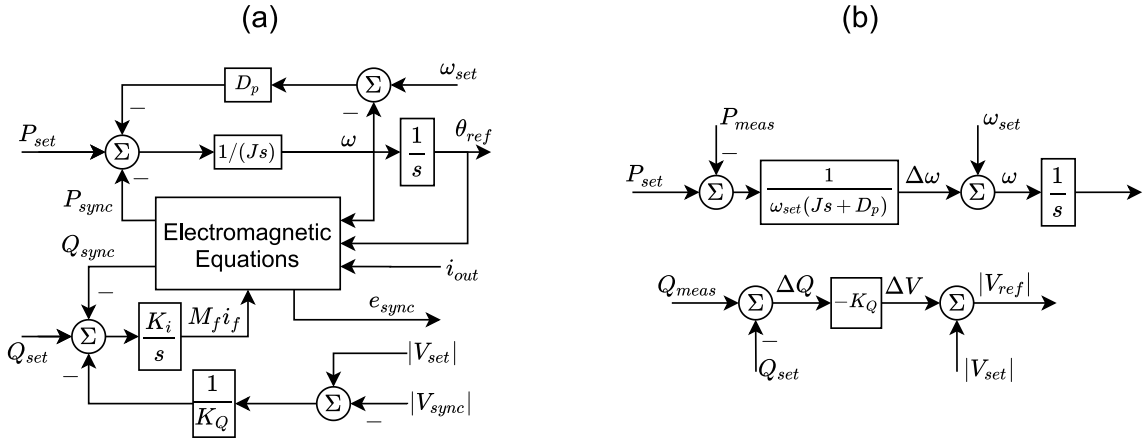


Figure 2.3: Synchronverter (a) and SPC (b) control schemes.

Another type of GFM control is denominated synchronous power control (SPC). The crux of its operation is to design the active power loop as an overdamped second order system, thus mitigating possible low-frequency oscillations [47, 48]. The transfer function $G_{SPC}(s)$ of this controller is:

$$G_{SPC}(s) = \frac{1}{\omega_{set}(sJ + D_p)} \quad (2.11)$$

Where J is the inertia constant and D_p is the damping of the controller. The SPC's block diagram is illustrated in Figure 2.3b.

It is reported in the literature that the LPF Droop, Synchronverter and SPC controllers have similarities between them, and their control parameters can be converted between these structures [19, 38, 49, 50].

Other unconventional controller structures are also present for GFM converters. Model predictive control has been proposed for GFM converters in [51, 52]. GFM controllers based on nonlinear oscillators have also been proposed in [53, 54]. This type of controller is called virtual oscillator control (VOC) and aims to mimic the dynamics of this type of circuit. Vander Pol oscillators are the most widely used models for VOC [18, 33, 55, 56]. It is worth to mention that the VOC has no inertia emulation capability [33].

In addition to reference generators, GFM converters can also be categorized according to the calculation method of the modulation signal [19]. The converter can have the named direct voltage synthesis method, where the reference signals are used directly for the pulse width modulation (PWM), without using a Proportional Resonant (PR) or Proportional Integral (PI) feedback control loop. It was proposed in [57], and a popular application is the Synchronverter controller, wherein its original design it uses only the Reference Generator loop.

A second structure for calculating the modulation signal uses only one feedback control loop and is referred to as Single-loop voltage control [19]. In this scheme, the filter capacitor voltage (V_C) is controlled. By only controlling this variable, and not having any kind of current limiting, this controller does not have good stability when facing network disturbances [58]. To overcome this problem, the Cascade Multi-loop control method is used, where two control loops are used. The outer one controls the capacitor voltage while the inner one controls the converter current, which can be either the capacitor current or the filter inductor current [59]. The Cascade Multi-Loop control and Single Loop voltage control are illustrated in Figures 2.4a and 2.4b, respectively.

The use of VI can also help the performance of cascade controllers [25]. The implementation of this scheme has vast flexibility, and will be discussed further in Sections 3.1 and 4.1 of this work.

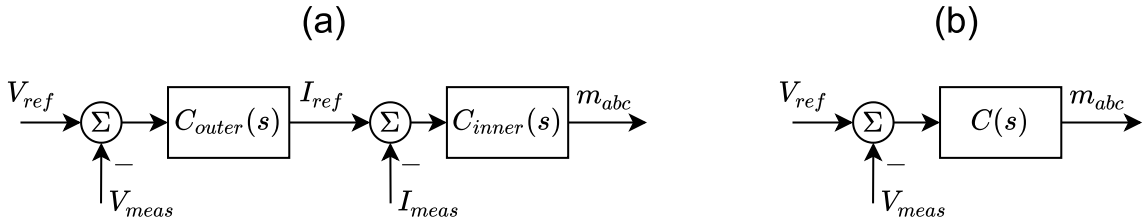


Figure 2.4: Generic cascaded multi-loop (a) and single-loop (b) block diagrams

2.2 The Generalized Closed-Loop Controller

The Generalized Closed-Loop controller is in a gray area between the Single-Loop and Cascaded Multi-loop controllers. This occurs because, in its original proposal in [24], GCC is a Single-loop controller that uses VI to overcome the disadvantages of a pure Single-loop controller. However, one of its VI can be interpreted as an internal feedback loop, as in a Cascaded Multi-loop controller. This will be further detailed in this section. Figure 2.6 illustrates the original GCC control scheme.

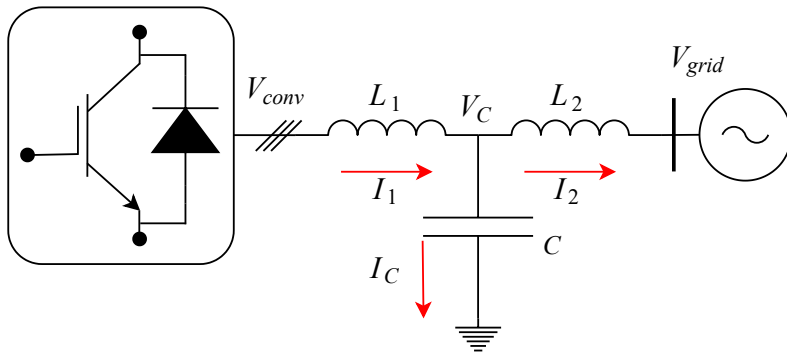


Figure 2.5: Converter topology and its measurements.

In Figure 2.5, L_1 and R_1 are respectively the converter-side inductance and its parasitic resistance, C is the filter capacitance, L_2 and R_2 are the grid-side inductance and its parasitic resistance. The currents I_1 , I_C , and I_2 are, respectively, the currents that flows through L_1 , C and L_2 , while V_C is the capacitor voltage.

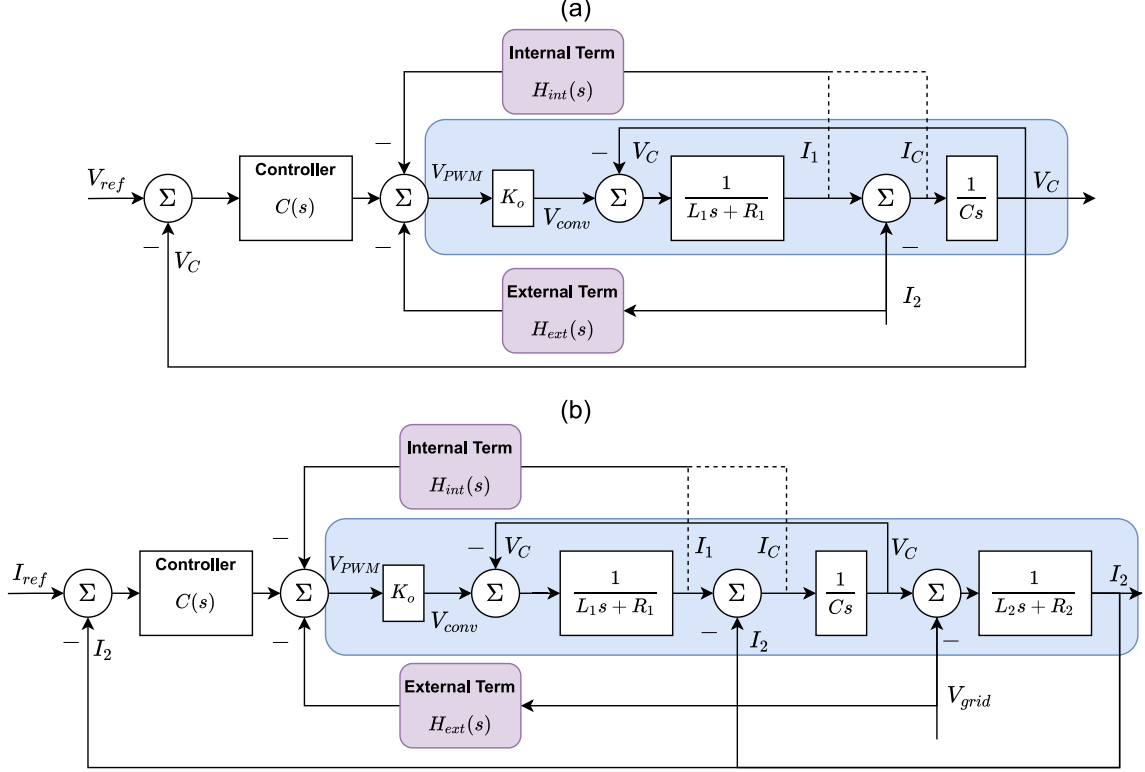


Figure 2.6: GCC scheme for a GFM-LC converter (a) and for a GFL-LCL converter (b).

Here, K_0 is the constant gain that models the converter according to (2.12). The two embedded VI are highlighted in purple in Figures 2.6a and 2.6b. They are named inner and outer VI, and they are categorized according to the electrical variables that are fed back [25].

$$K_0 = \frac{V_{DC}}{2} \quad (2.12)$$

The inner VI uses the feedback state variables, and its main function is to damp the converter filter resonance and to limit transient current, similar to an inner current loop of a Multi-loop controller [24]. Both converters, the GFL and the GFM, use as state variables the inductor currents on the converter side (I_1) and the capacitor current (I_C).

The outer VI, on the other hand, uses disturbance variables as feedback. In the case of GFL, the disturbance variable is the grid voltage (V_{grid}), while GFM uses the grid side current (I_2).

In this way, the generic equation for the GCC scheme can be written:

$$V_{PWM} = C(s)(X_{C,ref} - X_C) - H_{int}(s)X_{int} - H_{ext}(s)X_{ext} \quad (2.13)$$

Where V_{PWM} is the voltage signal to be synthesized by the PWM, $C(s)$ is the controller transfer function, $X_{C,ref}$ and X_C are respectively the generic control variable reference and measure, $H_{int}(s)$ and $H_{ext}(s)$ are respectively the inner and outer virtual impedance transfer function, and X_{int} and X_{ext} are the inner and outer generic feedback variable. Both the GFL and GFM with GCC scheme uses (2.13) as its core control equation.

He and Li proposed in the original paper the GCC scheme for both GFL and GFM converters, as shown in Figures 2.6a and 2.6b. As can be seen in these figures, the current-controlled GFL converter considers that the converter has an LCL filter at its terminals, while the GFM converter has an LC filter. The specific case of GFM with LCL filter was not covered in the article. Although the model of the GFM with LC filter was presented, the original article focused on the GFL converter with LCL filter.

He and Li's original work allows for new questions and research. The impact of different controllers on the final closed-loop system is a point of interest. As will be explained later, the controller $C(s)$ has a direct impact on the final behavior of the GFM converter. A goal of the present dissertation is to enhance studies on the in He and Li's original work. Figure 2.7 illustrates the simplified block diagram of the system to be analyzed. The complete mathematical model for the GFM with LCL filter will be considered in the next two subsections.

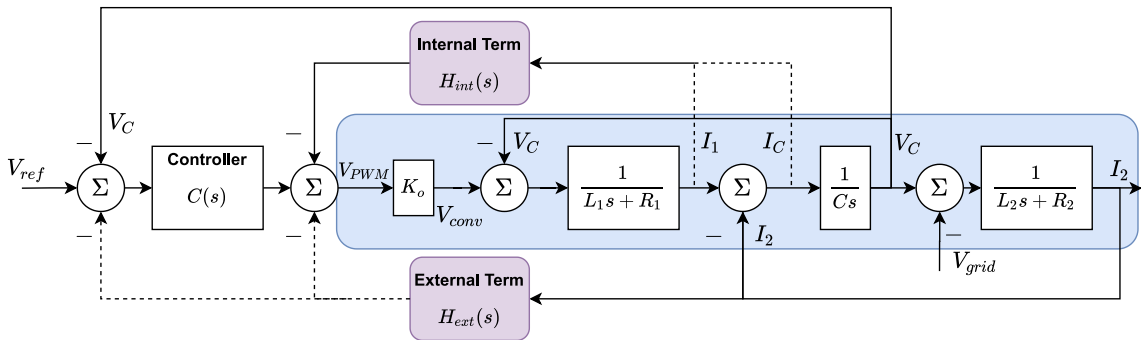


Figure 2.7: Studied GCC-GFM-LCL scheme.

2.2.1 The Inner Virtual Impedance

The inner VI has a similar function to an inner current loop of a multi-loop controller, which provides active damping of resonances, to control the feedback current, and to protect from current surges. Similarities between the two structures can be noted.

Assuming a multi-loop GFM control, as shown in Figure 2.4a, the internal current loop with controller $C_{inner}(s)$ and the outer voltage loop with controller $C_{outer}(s)$, each loop equation can be written as:

$$\begin{cases} I_{int,ref} = C_{outer}(s)(V_{ref} - V_C) & (2.14) \\ V_{PWM} = C_{inner}(s)(I_{int,ref} - I_{int}). & (2.15) \end{cases}$$

Where $I_{int,ref}$ and I_{int} are, respectively, the reference current and measured current of the converter (which can be either I_1 or I_C). Here, V_{pwm} is the same as m_{abc} depicted in Figure 2.4a. Substituting (2.14) into (2.15):

$$V_{PWM} = C_{inner}(s)C_{outer}(s)(V_{ref} - V_C) - C_{inner}(s)I_{int} \quad (2.16)$$

Equation (2.16) has a similar structure to (2.13), considering $H_{ext} = 0$. If the notation $C(s) = C_{inner}(s)C_{outer}(s)$ and $H_{int}(s) = C_{inner}(s)$ the multi-loop controller becomes a single-loop controller with an Internal VI. Some conclusions can be drawn from this algebraic manipulation.

The GCC has a parallel structure of the VI where they are easily removable when $H_{ext}(s) = H_{int}(s) = 0$, making it a simple single-loop controller. In the case of the multi-loop controller $H_{int}(s) = 0$ also means $C_{inner}(s) = 0$, i.e. the current loop is removed. Furthermore, the equivalent controller $C(s) = C_{outer}(s)C_{inner}(s) = 0$ would also be removed, i.e. there would be no control loop.

This example shows the flexibility of GCC concerning the Multi-loop controller. The voltage-tracking dynamics of the Multi-loop are directly affected by the dynamics of $C_{inner}(s)$, while in GCC independent design of $C(s)$ and $H_{int}(s)$ is possible. This also makes it easier to implement adaptive $H_{int}(s)$ if desired.

The feedback current used by $H_{int}(s)$ has a major role in the dynamics of the final system. According to the choice of either I_1 or I_C the positioning of the virtual impedance is changed, as well as the resonance damping capability. If I_1 is taken as the feedback variable the resulting VI is in series with L_1 , while if I_C is taken the resulting VI is in parallel with C_f [24]. Figures 2.8a and 2.8b illustrate the position of the VI when using, respectively, the currents I_1 and I_C . If $H_{int}(s)$ is a constant, i.e. has no dynamics (H_{int}), the virtual impedance will be equivalent to a resistance.

It is worth mentioning that although He and Li's original work cites only these two possibilities for state variables, other variable possibilities exist, and the resulting VI will also vary its position. However, in this section only He and Li's original propositions will be discussed. The discussion of the other possibilities will be carried out in the literature review on active damping and virtual impedance in Section 3.1.

Another point that was not discussed in the original publication is the complete

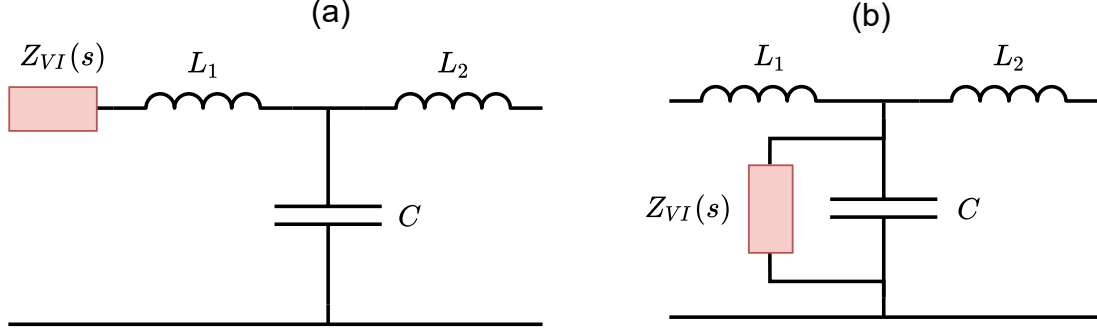


Figure 2.8: Resulting virtual impedance when using inductor current I_1 (a) and capacitor current I_C (b).

mathematical model for the GFM converter, either with LC filter or with LCL. The model that will be studied below will serve for the cases of GFM converter with the LC and LCL filters.

The GCC-GFM converter with LC filter is a particular case of GCC-GFM with LCL filter, where the grid-side inductance is zero. However, since the GCC-GFM uses only one loop controlling V_C , and the internal impedance if used I_1 or I_C currents, the second inductance does not interfere with the tracking control dynamics [25]. The inductance L_2 can be considered as a line impedance between the converter and the grid, affecting only the output impedance of the converter [60].

Figure 2.9 displays the block diagram of the system considering $H_{ext}(s) = 0$. In addition, L_2 and R_2 are also omitted from this block diagram since they do not directly impact the study of inner VI. These components will be taken into consideration when $H_{ext}(s)$ is considered.

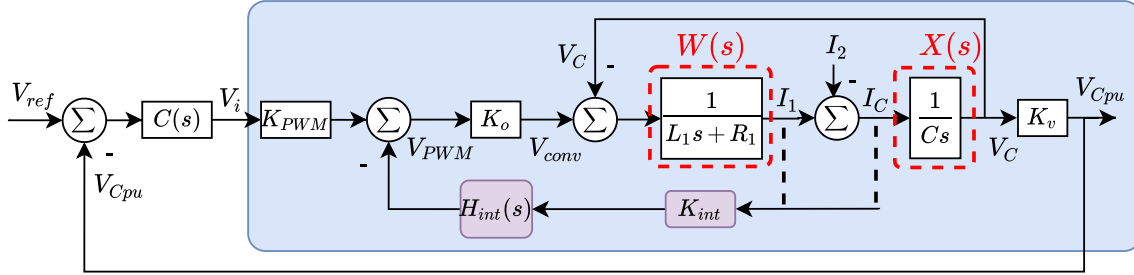


Figure 2.9: Complete inner VI control scheme.

In Figure 2.9 K_v is the voltage per unit gain, defined by the peak phase base voltage $V_{peak,phase}$, K_{PWM} is the PWM gain responsible for matching the converter's DC base to the AC base, i.e., the amplitude modulation index, and K_{int} is the per unit current gain defined by the peak phase base current $I_{peak,phase}$ times K_{PWM} .

$$K_v = \frac{1}{V_{peak,phase}} \quad (2.17)$$

$$K_{PWM} = \frac{2V_{peak,phase}}{V_{DC}} \quad (2.18)$$

$$K_{int} = \frac{K_{PWM}}{I_{peak,phase}} \quad (2.19)$$

The control plant is highlighted in blue. As can be seen, $H_{int}(s)$ is considered part of the plant, even though it is a control element. This can be interpreted as the control feedback through $H_{int}(s)$ is visualized by the controller $C(s)$ as an element of the plant. This assumption is valid since $C(s)$ and $H_{int}(s)$ are independent, as commented earlier. The dynamics of the capacitor's voltage are:

$$V_C = G_{LC_{ind,cap}}(s)V_i - Z_{LC_{ind,cap}}(s)I_2 \quad (2.20)$$

Where $G_{LC_{ind,cap}}(s)$ is the filter tracking transfer function using, respectively, either I_1 or I_C , V_i is a generic voltage signal at the filter terminal, and $Z_{LC_{ind,cap}}(s)$ is the disturbance transfer function, also described as the filter output impedance.

The interpretation regarding the nomenclature of "filter output impedance" can be made from the analysis of the transfer functions of the system. By the Superposition Theorem, if it is desirable to analyze the disturbance variable I_2 concerning the output voltage V_C , it is necessary to remove the generic voltage input V_i from (2.20). In this way:

$$V_i = 0 \therefore V_C = -Z_{LC_{ind,cap}}(s)I_2 \therefore \frac{V_C}{I_2} = -Z_{LC_{ind,cap}}(s) \quad (2.21)$$

Considering the current I_1 as the feedback variable for the inner VI, the $G_{LC_{ind}}(s)$ is:

$$G_{LC_{ind}}(s) = \frac{K_0 K_{PWM} K_v W(s) X(s)}{1 + W(s) X(s) + K_0 K_{int} H_{int}(s) W(s)}, \quad (2.22)$$

while the transfer of $G_{LC_{cap}}(s)$, using the current I_C , is:

$$G_{LC_{cap}}(s) = \frac{K_0 K_{PWM} K_v W(s) X(s)}{1 + W(s) X(s) + K_0 K_{int} H_{int}(s) W(s)}. \quad (2.23)$$

As can be noted in equations (2.22) and (2.23), $G_{LC_{cap}}(s) = G_{LC_{ind}}(s)$, i.e. the choice of inner VI feedback variables does not affect the tracking dynamics of the system. However, the same do not happen when analyzing $Z_{LC_{ind}}(s)$ and $Z_{LC_{cap}}(s)$, shown respectively in (2.24) and (2.25). This means that the choice between I_1 and I_C directly affects the output impedance of the filter.

$$Z_{LC_{ind}}(s) = \frac{X(s) + K_0 K_{int} H_{int}(s) W(s) X(s)}{1 + W(s) X(s) + K_0 K_{int} H_{int}(s) W(s)} \quad (2.24)$$

$$Z_{LC_{cap}}(s) = \frac{X(s)}{1 + W(s)X(s) + K_0K_{int}H_{int}(s)W(s)} \quad (2.25)$$

It is important to note that in case $H_{int}(s) = 0$, $G_{LC_{ind}}(s)$, $G_{LC_{cap}}(s)$, $Z_{LC_{ind}}(s)$, and $Z_{LC_{cap}}(s)$ transfer functions are equal to that of an LC filter without active damping.

An important issue about using I_C as feedback is the presence of high switching frequencies in this current. The capacitor naturally has a low impedance path for high frequencies. Therefore, in the LCL filter the high frequencies due to switching will flow through C . Then, it becomes necessary to use a low-pass filter in the controller to eliminate these frequencies from the I_C current, reducing the risk of GCC instability. This filter can be included in $H_{int}(s)$ transfer function. This topic will be discussed further in Section 3.3.2.

Once the transfer functions of the plant are obtained, the closed-loop model of the single-loop controller with the inner VI is described by:

$$V_C = G_{cl_{ind,cap}}(s)V_{ref} - Z_{cl_{ind,cap}}(s)I_2 \quad (2.26)$$

Where $G_{cl_{ind,cap}}(s)$ is the closed loop tracking transfer function and $Z_{cl_{ind,cap}}(s)$ is the converter closed loop output impedance. They are defined, respectively, in equations (2.27) and (2.28).

$$G_{cl_{ind,cap}}(s) = \frac{G_{LC_{ind,cap}}(s)C(s)}{1 + G_{LC_{ind,cap}}(s)C(s)} \quad (2.27)$$

$$Z_{cl_{ind,cap}}(s) = \frac{Z_{LC_{ind,cap}}(s)}{1 + G_{LC_{ind,cap}}(s)C(s)} \quad (2.28)$$

Thus, the inner VI will also affect the closed loop dynamics of the system, just as the model and design of the controller $C(s)$ affects the output impedance of the converter.

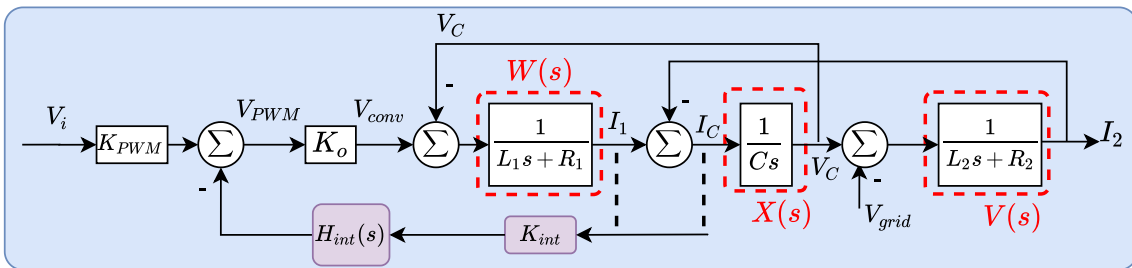


Figure 2.10: LCL filter block diagram.

Although the control plant is an LC filter, the LCL filter is still present internally in the converter. The excited resonances at I_2 must also be damped, as the open-loop equation (2.29) presents. Figure 2.10 depicts the block diagram for the open

loop LCL filter. This figure is the same of the blue box in Figure 2.9 plus the loop including L2 and R2 dynamics.

$$I_2(s) = G_{LCL_{ind,cap}}(s)V_i(s) - Y_{LCL_{ind,cap}}(s)V_{grid}(s) \quad (2.29)$$

Where $G_{LCL_{ind,cap}}(s)$ is the LCL filter tracking function and the $Y_{LCL_{ind,cap}}(s)$ is filter output admittance. For the I_1 current feedback, $G_{LCL_{ind}}$ and $Y_{LCL_{ind}}$ are respectively described in (2.30) and (2.31), while for the I_C current $G_{LCL_{cap}}$ and $Y_{LCL_{cap}}$ are shown in (2.32) and (2.33).

$$G_{LCL_{ind}}(s) = \frac{K_0 K_{PWM} W(s) X(s) V(s)}{1 + W(s) X(s) + X(s) V(s) + W(s) K_0 K_{int} H_{int}(s) + W(s) X(s) V(s) H_{int}(s) K_{int} K_0} \quad (2.30)$$

$$Y_{LCL_{ind}}(s) = -\frac{W(s) X(s) V(s) + V(s) + W(s) V(s) H_{int}(s) K_{int} K_0}{1 + W(s) X(s) + X(s) V(s) + W(s) K_0 K_{int} H_{int}(s) + W(s) X(s) V(s) H_{int}(s) K_{int} K_0} \quad (2.31)$$

$$G_{LCL_{cap}}(s) = \frac{K_0 K_{PWM} W(s) X(s) V(s)}{1 + W(s) X(s) + X(s) V(s) + K_0 K_{int} H_{int}(s) W(s)} \quad (2.32)$$

$$Y_{LCL_{cap}}(s) = \frac{V(s) + W(s) X(s) V(s) + K_0 K_{int} H_{int}(s) W(s)}{1 + W(s) X(s) + X(s) V(s) + K_0 K_{int} H_{int}(s) W(s)} \quad (2.33)$$

2.2.2 The Outer Virtual Impedance

With the closed loop model with inner VI in hand, adding $H_{ext}(s)$ and L_2 is a simple task. First, the addition of outer VI will be analyzed, and then L_2 will be added. Figure 2.7 exhibits the two possibilities for implementing outer VI.

The first implementation of outer VI, proposed in the original work by He and Li, uses the feedback signal from I_2 in the summation that generates V_{PWM} , next to the feedback from inner VI. However, in the vast majority of the literature, the implementation of outer VI is accomplished by changing the voltage V_{ref} of the controller $C(s)$. To be in line with the literature, the second implementation will be used in this paper, since both implementations are equivalent.

The outer VI does not affect the tracking transfer function $G_{cl_{ind,cap}}(s)$, only changing the converter output impedance $Z_{cl_{ind,cap}}(s)$ [25]. The equation governing the behavior of V_C in the presence of $H_{ext}(s)$ is:

$$V_C = G_{cl_{ind,cap}}(s)V_{ref} - K_z (Z_{cl_{ind,cap}}(s) + H_{ext}(s)G_{cl_{ind,cap}}(s)) I_2 \quad (2.34)$$

Where K_z is the impedance gain in per unit. Two major conclusions are drawn from (2.34). The first is that the resulting impedance $Z_{ext}(s) = K_z H_{ext}(s) G_{cl_{ind,cap}}(s)$ is in series with the impedance $Z_{cl_{ind,cap}}(s)$ [25, 60]. The second conclusion is that the closed loop transfer function $G_{cl_{ind,cap}}(s)$ directly affects the frequency shape of the resulting outer VI. Thus, different types of $C(s)$ operating with the same $H_{ext}(s)$ will result in a different outer VI. This comparative aspect of the impact of different $C(s)$ was not studied in either He and Li's original work or in subsequent virtual impedance studies.

The addition of the second inductance L_2 and its parasitic resistance R_2 proceeds similarly to the addition of $H_{ext}(s)$. Like outer VI, it will not affect the tracking dynamics of $G_{cl_{ind,cap}}(s)$ and, because it is a physical element of the converter, there will be no influence of $G_{cl_{ind,cap}}(s)$ on the resulting impedance. Equation (2.35) indicates the mathematical formulation governing this system.

$$V_{grid} = G_{cl_{ind,cap}}(s)V_{ref} - K_z (Z_{cl_{ind,cap}}(s) + H_{ext}(s)G_{cl_{ind,cap}}(s) + (L_2s + R_2)) I_2 \quad (2.35)$$

The equivalent impedance $L_2s + R_2$ is in series with $Z_{ext}(s)$, and the total output impedance of the converter $Z_{out}(s) = K_z (Z_{cl_{ind,cap}}(s) + Z_{ext}(s) + L_2s + R_2)$ [60]. Note that on the left side of the equation there is now V_{grid} instead of V_C . This occurs because (2.35) represents the Thévenin equivalent of the complete converter as seen by the grid at the point of common connection, while (2.34) presents the Thévenin equivalent as seen by the filter capacitor node. Figure 2.11 graphically displays the Thévenin equivalent of the GFM-GCC with LCL filter. The blue highlight indicates the output impedance of $Z_{cl_{ind,cap}}(s)$ in series with $Z_{ext}(s)$, while the purple one illustrates the total output impedance $Z_{out}(s)$ of the converter.

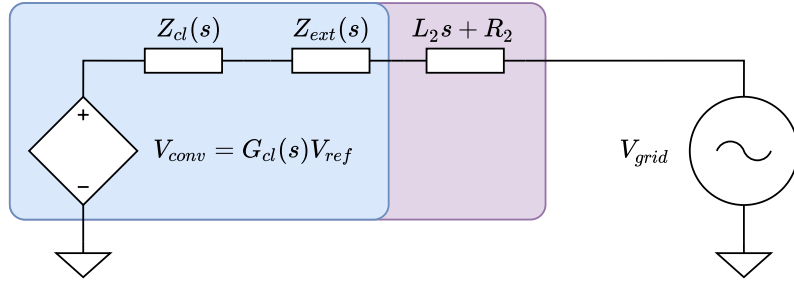


Figure 2.11: Thévenin's equivalent for the GCC-GFM-LCL controller

2.3 Resonant Controllers Formulation

The generic voltage controller $C(s)$ affects directly on the impedance shape of $Z_{ext}(s)$, and consequently the total output impedance $Z_{out}(s)$. Different controllers will generate different impedance shapes, as well as controllers that have the same mathematical model but different parameter design.

Impedance and phase reshape techniques have been studied for PI controlled systems in dq reference [61, 62]; and for systems controlled by resonant controllers in $\alpha\beta$ reference [63, 64]. However, none of these publications compare different controllers and design methods associated with the use of outer VI.

In He and Li's original work, the controller $C(s)$ is a resonant type. To maintain consistency with the original work, two different resonant controllers will be studied, as well as their design methods: the Proportional Resonant controller (PR); and the Vectorial Proportional-Integral controller (VPI). Both controllers will be explained in the following.

2.3.1 Proportional-Resonant Controller

Applications requiring zero steady-state tracking error for sinusoidal references employ the PR controller. Its mathematical model was inspired by the conventional PI controller, which is frequently employed in control systems with a dq -frame foundation. The parameterization of the PI controller is shown in equation (2.36).

$$G_{PI}(s) = K_P + \frac{K_I}{s} \quad (2.36)$$

Where $G_{PI}(s)$ is the PI transfer function, and K_P and K_I are, respectively, the proportional and integral controller gains.

However, PI controllers are not suitable for sinusoidal signal reference tracking. In order to develop an equivalent controller to track sinusoidal references, a transformation is therefore presented in [65].

As $G_{PI}(s)$ has a LPF behavior, using the frequency transformation $s = \frac{s^2 + \omega_0^2}{2s}$ and substituting it in (2.36), it results in a band-pass transfer function, described in (2.37).

$$G_{PR}(s) = G_{PI} \left(\frac{s^2 + \omega_0^2}{2s} \right) \quad (2.37)$$

Choosing ω_0 as the grid frequency, a sinusoidal controller equivalent to $G_{PI}(s)$ can be obtained. Thus the resultant proportional resonant controller $G_{PR}(s)$ is:

$$G_{PR}(s) = K_P + \frac{2K_I s}{s^2 + \omega_0^2} = K_P + \frac{K_R s}{s^2 + \omega_0^2} \quad (2.38)$$

By analyzing (2.38), it is possible to determine that the resonant gain K_R and the integral gain K_I are correlated: $K_R = 2K_I$. As mentioned in [65], a given PI controller can be converted into a PR using this relationship while keeping its dynamical features.

Gao's Design Method for PR controller

In [66], it is mentioned that a PI controller with $G_{PI}(s)$ transfer function is suitable for first-order plants, with a typical transfer function described in (2.39). By using the design procedure described in [66], a pole-zero cancellation results in the desirable dynamic response.

$$G_{plant}(s) = \frac{K}{Ts + 1} \quad (2.39)$$

Where K is the final steady-state value and T is the time constant.

Choosing a desirable bandwidth $\omega_c = \frac{1}{\tau_c}$, it is possible to calculate the PI controller gains, as illustrated in (2.40).

$$\begin{cases} K_P^{Gao} = \frac{T\omega_c}{K}; \\ K_I^{Gao} = \frac{\omega_c}{K}; \end{cases} \quad (2.40)$$

By calculating K_P^{Gao} and K_I^{Gao} by (2.40), a pole-zero cancellation results in a closed-loop transfer function with the desired ω_c in dq -frame. Finally, the relationship described in (2.38) can be used to determine the PR gains.

$$K_R^{Gao} = 2K_I^{Gao}. \quad (2.41)$$

Analytical Design Method for PR controllers

In [67] an analytical and straightforward approach was suggested. It is feasible to calculate the PR gains directly in $\alpha\beta$ -frame — without using the transformation used in (2.38) — by selecting and allocating the complex-conjugate pair of poles $p_{1,2}$ ($p_2 = p_1^*$). The damping ratio ζ and natural frequency ω_n of a second order system can be used to define poles, which are shown in the equation (2.42).

$$p_{1,2} = -\zeta\omega_n \pm j\omega_n\sqrt{1 - \zeta^2} \quad (2.42)$$

The two equations that compute directly the controller gains are:

$$\begin{cases} K_P = -\frac{\text{Im}(G_r(p_1)G_{plant}(p_1))}{|G_{plant}(p_1)|^2 \text{Im}(G_r(p_1))}; \\ K_R = \frac{\text{Im}(G_{plant}(p_1))}{|G_{plant}(p_1)|^2 \text{Im}(G_r(p_1))}. \end{cases} \quad (2.43)$$

Where, $G_r(s) = \frac{s}{s^2 + \omega_0^2}$ and G_{plant} can be any type of system transfer function. It is also important to emphasise that the allocation of the $p_{1,2}$ poles is not permitted by equations (2.43) such that the closed-loop system has 0% overshoot ($\zeta = 1$). The factor $\text{Im}(G_r(p_1))$, which is equal to 0 if $zeta = 1$, is present in the denominators of K_P and K_R , resulting in an indeterminate division.

2.3.2 Vectorial Proportional-Integral Controller

Originally, the Vectorial Proportional-Integral (VPI) was designed to operate in the synchronous components dq [68]. Positive and negative sequence harmonics are represented in this reference frame as sinusoidal signals with frequency $k\omega_0$, where $k = 6n$ and $n = [0, 1, 2, 3\dots]$. This happens because in the dq reference frame, sinusoidal signals with the harmonic order $k = 6n$ are seen to represent the positive and negative sequence harmonics, which are described as $k = 6n + 1$ and $k = 6n - 1$ respectively. As a result, the PI controller is given a frequency shift of $jk\omega_0$ to compensate these signals, leading to:

$$\begin{cases} G_{VPI+} = \frac{K_P s + K_I}{s - jk\omega_0}; \\ G_{VPI-} = \frac{K_P s + K_I}{s + jk\omega_0}. \end{cases} \quad (2.44)$$

As the final controller must be able to compensate both sequence components,

$$G_{VPI} = G_{VPI+} + G_{VPI-} = 2 \frac{K_P s^2 + K_I s}{s^2 + (k\omega_0)^2}. \quad (2.45)$$

Taking $k = 1$, the VPI controller is set to the fundamental frequency to compensate $\alpha\beta$ -frame systems.

Design Method for VPI controllers

Similar to the aforementioned Gao's method, the VPI parameters design results in a pole-zero cancellation with the plant. Contrastingly, this cancellation with VPI controllers occurs immediately on $\alpha\beta$ -frame [69]. Therefore, the VPI controller gains can be calculated using the following equations for the transfer function shown in (2.39):

$$\begin{cases} K_P^{VPI} = \frac{T\omega_c}{2K}; \\ K_I^{VPI} = \frac{\omega_c}{2K}; \end{cases} \quad (2.46)$$

In a similar way as in (2.41), and for later comparisons of the controllers:

$$K_R^{VPI} = K_I^{VPI}. \quad (2.47)$$

2.4 The Studied Converter

With the proper mathematical models of the filter, the GFM-GCC, and the controllers to be used, it is necessary to present the converter to which the proposed control will be applied.

The converter used in this study is based on a real equipment that exists in the laboratory with an *LCL* filter in its output. The electrical values and parameters of the converter and filter are listed in Table 2.1, and Figure 2.12 shows its topology. As the real equipment is a back-to-back converter, the simulated one is fed by a DC ideal source. Thus, the dc link dynamics are neglected in this work.

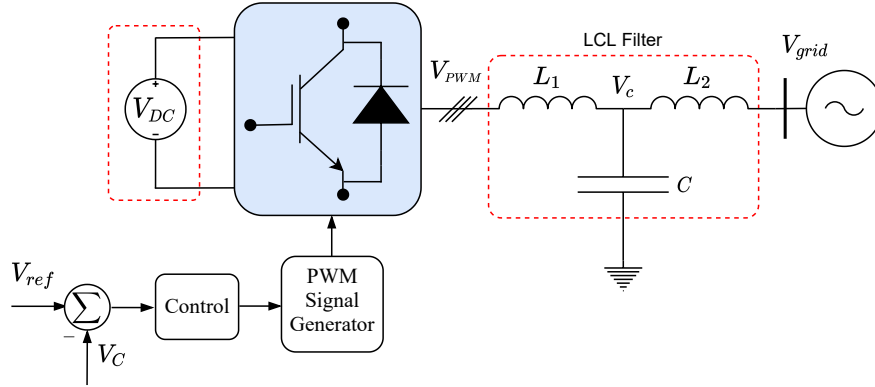


Figure 2.12: Converter topology.

Looking at both Table 2.1 and Figure 2.12, it can be seen that the filter does not have any proper resonance damper, neither in parallel nor in series with the capacitor C , relying only on the parasitic resistances R_1 and R_2 for this function. Thus, the implementation of inner VI will have the function of damping the filter's intrinsic resonance, as well as limiting the converter's current.

Another point to consider in this converter is its K_{PWM} value. Plugging the values from Table 2.1 into equation (2.48) results in:

$$K_{PWM} = \frac{2V_{peak,phase}}{V_{DC}} = \frac{2 \times 179.60}{406} \approx 0.885 \quad (2.48)$$

Table 2.1: Studied converter electrical parameters.

Converter Parameters	
Line Voltage (V_{rms})	220
DC Link Voltage (V)	406
Rated Current (A_{rms})	78.73
Rated Power (kVA)	30
Grid Frequency (Hz)	60
Switching Frequency (Hz)	5940
L_1 (mH)	0.6
R_1 (m Ω)	1.85
L_2 (mH)	0.17
R_2 (m Ω)	1.85
C (μ F)	90

This means that when the converter synthesizes a sinusoidal signal with amplitude 1 pu on the AC side of its terminals, the three-phase modulation index m_{abc} has amplitude equal to 0.885, i.e., it is in the linear PWM region and has a margin of 0.115.

In this work, the outer VI used will be negative for reactive power flow improvement. This implies that the voltage drop in the outer VI will add up with the output voltage value of the converter. This voltage gain associated with reactive power injection can exceed the 0.115 margin, overmodulating the converter. This phenomenon is analyzed in Chapter 4.

A possible increase in the DC link voltage — consequently a reduction in K_{PWM} — could solve this problem. However, this would change the performance of the LCL filter, since it is designed to operate at the specified DC voltage. Furthermore, it is not the goal of this work to make changes to the hardware and operation point of the converter, focusing only on the control.

Chapter 3

Inner Virtual Impedance Design

A review of active damping techniques for LCL filters is provided, due to its intrinsic connection with the Inner Virtual Impedance. The design and implementation of the Inner Virtual Impedance are presented, and simulation results are discussed comparing the resonant controllers.

3.1 Inner Virtual Impedance Literature Review

The relationship between active damping, the internal current loop of a cascade controller and the Inner VI was explained in the previous section. Active techniques have the advantage over passive techniques that they have no damping losses due to their application [70, 71]. This caution is even more latent in converters operating at medium and high powers [72, 73]. Two main families of active damping are described in the literature: filter-based and state-feedback-based techniques [74, 75]. State-feedback-based techniques are also known as virtual-impedance-based techniques [74]. From now on, virtual-impedance-based techniques will be the nomenclature used in this work.

Filter-based techniques use digital filters directly on the converter's control effort output. In this way, there is no need to use additional sensors for measuring a specific filter state [74]. The main digital filter used is the notch filter [76–79], but there are applications using low-pass filters [77] and all-pass filters [80]. The principle of operation of the notch filter is to generate an anti-peak resonance to cancel out the intrinsic resonance of the LCL filter. The low-pass filter, on the other hand, has its cutoff frequency set to the resonance of the LCL, thus causing a phase lag that stabilizes the system [77]. The all-pass filter operates in a similar way to the low-pass filter. Despite its qualities, this type of implementation has robustness problems due to its dependence on the resonance frequency of the filter, which can change over time due to depreciation of the filter's passive components. For this reason, virtual-impedance-based techniques are recommended in the literature [74, 75].

Virtual-impedance-based techniques use filter state variables to accomplish the desired damping. As a consequence, the proper measurement of these states is required through sensors, which can make the converter design more expensive. Although He and Li's GCC proposal only considers the currents I_1 and I_C for the Inner VI, the current I_2 and voltage V_C can also be fed back [74, 81]. Several types of implementation have been reported in the literature for these four electrical variables.

The converter-side current I_1 has a simple implementation, and can be accomplished as a proportional [24, 82] gain or via the Weighted Average Current control scheme [83, 84]. However, both implementations have the drawback of exciting new resonances in the filter or between the filter and the grid.

The grid-side current I_2 is normally fed back using high-pass filters with negative gains [85, 86]. The positive point of this technique is that most GFL converters have the sensor for this current, since this variable is the most stable for current control, cheapening the cost of application [81]. GFM converter also has this current measurement because it needs it to calculate the instantaneous power in its power

controller. However, this feedback technique using high pass filter has the drawback of amplifying high frequency noise and can decrease the system bandwidth [74].

The variables I_C and V_C , related to the filter capacitor, are the most widely used in the literature and have the greatest diversity of applications. For I_C , implementations using proportional gains [24], proportional and integral gains [87], first [88] and second order [89] high-pass filters are some examples. For V_C , high-pass filters [90], lead-lag controllers [91], proportional gains [92] and generalized integrator [93] are some examples. Despite the variety of implementations, the most used are proportional gain for I_C and the derivative action of the first order high-pass filter for V_C [75, 91, 94–98].

A study published in 2019 presents a lengthy comparison of virtual resistor implementations in virtual impedance-based techniques, that is, the focus is on comparing implementations that result in equivalent virtual resistors connected to the LCL filter [81]. In this paper, the four possible feedback states (I_1 , I_2 , I_C and V_C) are combined with the six possible equivalent positions in the filter: in series or parallel with L_1 ; in series or parallel with L_2 ; and in series or parallel with C_f . This results in 24 implementation possibilities. The transfer functions that result in these combinations are also presented. It is concluded that the best position for the virtual resistor to be allocated is in parallel with C [81, 99]. The recommended variables for allocation in this position are the currents I_2 , I_C , and the voltage V_C , with the best choice being I_2 . This decision making is based on the simplicity of application and the fact that the main current control uses I_2 as the feedback variable, thus saving on sensors. It is worth noting that the transfer function to accomplish this implementation needs a second order high-pass filter, which can amplify high frequency noise [81]. An equivalent transfer function is proposed in [81] to mitigate this problem.

Additional comparisons were made regarding the capacitor variables I_C and V_C in [75]. In this work, the proportional gain implementation of I_C was compared to the high-pass filter implementation of V_C . The major findings of the publication are the advantages and disadvantages of using each of the variables. Both I_C and V_C are robust when the converter is connected to a weak grid that can present issues related to voltage harmonics. However, when using V_C there is higher mitigation of current harmonics when compared to I_C feedback. The lead-lag network of V_C feedback can increase the computational effort of implementing this feedback, especially in large-scale and highly complex systems. Both I_C and V_C measurements are subject to the high frequencies and noise existing in C_f , since this component is a low-impedance path for these higher frequencies [75].

Both the virtual impedance-based and filter-based techniques have performance drops in the presence of the digital control delay, which also involves the sampling

frequency of the system [74, 100]. The presence of these effects can be modeled as a phase delay that can lead the system to instability [101]. Predictive control [102–104], modified sampling [105, 106], and filter-based techniques [107–109] are able to mitigate this problem. However, in this dissertation, the effect of digital delay will not be considered in the GCC analyses.

3.2 Inner Virtual Impedance Design

The literature review points out that the variables I_C and V_C are good options for implementing virtual impedances, once that there is proper sensing of these measurements. Nonetheless, there are some notes regarding this statement. Most of the work presented in the literature review is on GFL converters with LCL filters, i.e., they are current controlled. Therefore, it is not natural that these converters have sensors for C states. However, in the context of GFM converters, where the voltage V_C is the controlled variable, the measurements of this state is present. Furthermore, the converter on which this dissertation is based on has current I_1 and I_2 sensors in addition to the voltage V_C one. Thus, it is possible to achieve simply calculation of the current I_C by:

$$I_1 - I_2 = I_C \quad (3.1)$$

In [59], the authors compared different feedback variables in a cascaded multi-loop controller scenario for both GFM converters with LC filters and GFL converters with LCL filters. For the GFM-LC controller, the currents I_1 and I_C were compared. For the GFL-LCL controller, the currents I_1 and I_C were compared in addition to the voltage V_C , and the voltage drop V_2 at L_2 and R_2 . As a conclusion, the I_C current was the best choice for application in GFM-LC converters and also a good choice for GFL-LCL converters. This conclusion is also presented in [110].

Thus, in this dissertation, the current I_C will be used as the feedback variable. Moreover, the choice of this current is also in accordance with the proposition of the GCC by He and Li, which is the main reference in this work. From now on, for clarity of reading, the transfer functions of the GCC with inner VI using I_C presented in the previous chapter will be written without the subscript *cap*.

As mentioned in Section 2.4, the studied converter does not have passive damping in its construction, requiring the use of inner VI to mitigate this problem. In the GFM-LCL case, the inner VI should be able to damp simultaneously two resonances: the LC filter resonance, which is seen by the voltage control and can instabilize it if not damped; and the LCL filter resonance, since it is part of the power converter.

The resonance peak of the LC filter can be seen graphically through the Bode

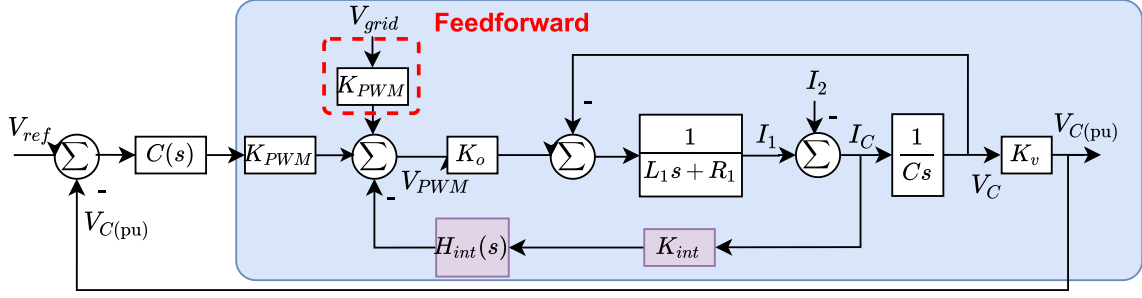


Figure 3.1: Complete control diagram with I_C current feedback and V_{grid} feedforward.

diagrams of the transfer functions G_{LC} , from (2.23), and Z_{LC} , from (2.25), in Figures 3.2 and 3.3, respectively. These Figures illustrate the frequency responses of the system varying the gain of $H_{int} = [0, 4, 6, 8, 10]$, meaning that a virtual resistor will be implemented. The minimum value of $H_{int} = 4$ was chosen because values below are not able to remove completely the resonance peak on the bode diagram of the LC filter.

The major impact of the inner VI insertion occurs in the surroundings of the resonance frequency. This occurs for both $G_{LC}(s)$ and $Z_{LC}(s)$. Figure 3.2 illustrates the Bode diagram of $G_{LC}(s)$, as H_{int} increases the flattening of the frequency response in the resonance region. As a consequence, this reduces the plant bandwidth ω_{LC} , which results in worse transient dynamics. However, the gain and phase margins of the plant do not change significantly. Therefore, the design of H_{int} for $G_{LC}(s)$ is a trade-off between damping and dynamic performance.

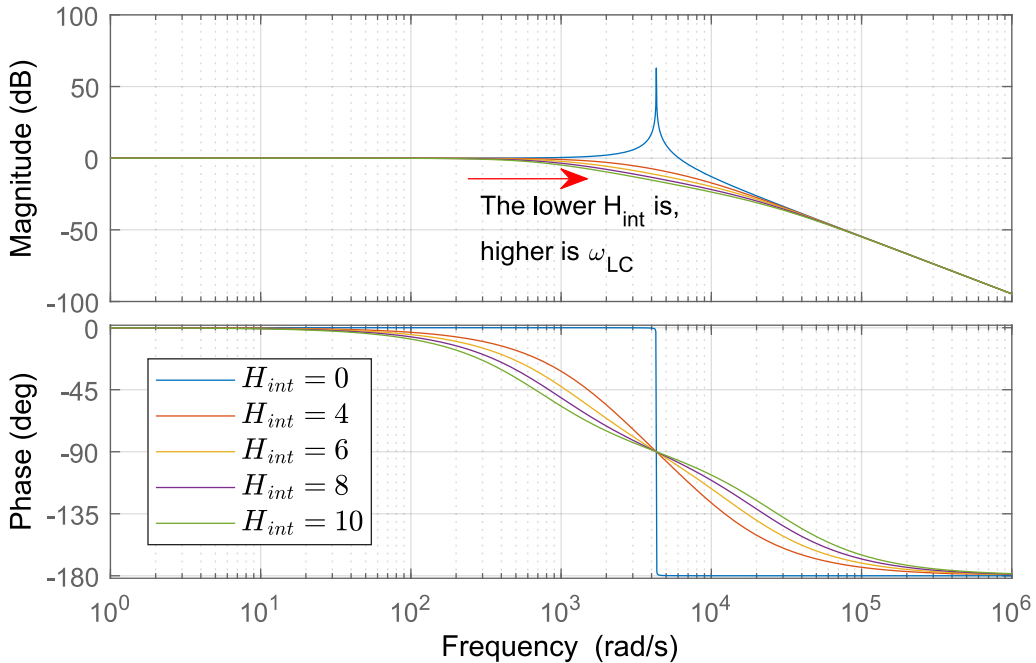


Figure 3.2: Bode diagram of $G_{LC}(s)$ for different values of H_{int} . As H_{int} decreases, the bandwidth ω_{LC} increases.

The opposite phenomenon happens when analyzing the Bode diagram of $Z_{LC}(s)$, in Figure 3.3. As one increases H_{int} , the sensitivity to disturbances at frequencies near resonance is also increased. This can also be interpreted as the equivalent impedance of the open loop LC plant decreasing as H_{int} increases, becoming closer to an ideal source. Thus, the design of H_{int} must consider a trade-off between dynamic response and disturbance rejection, when taking account both transfer functions $G_{LC}(s)$ and $Z_{LC}(s)$.

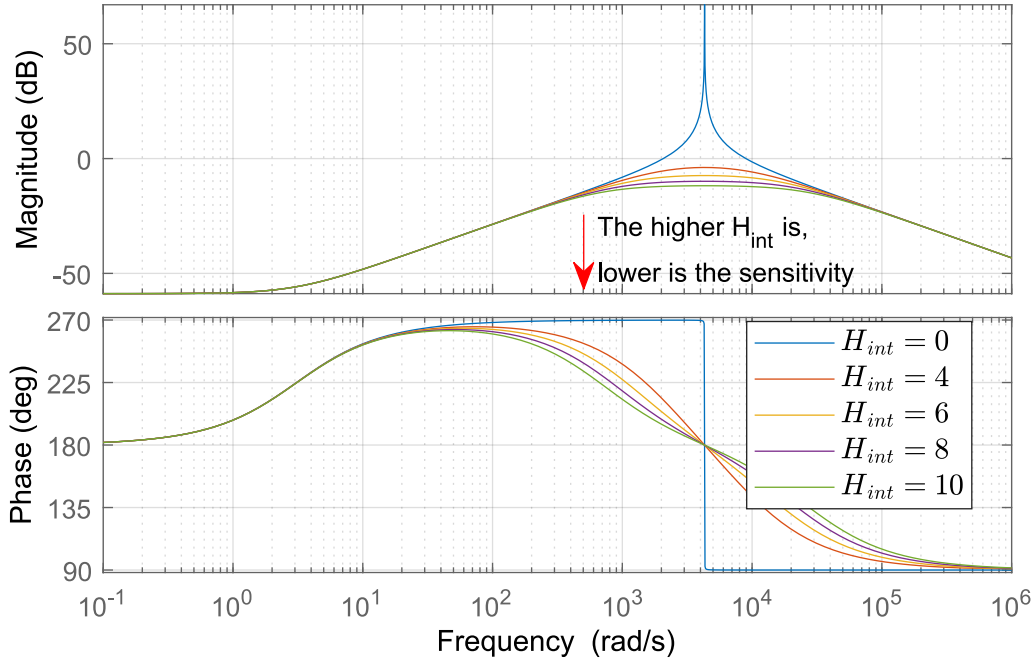


Figure 3.3: Bode diagram of $Z_{LC}(s)$ for different values of H_{int} . As H_{int} increases, the sensitivity for disturbances decreases.

Similarly, the Bode diagrams for the LCL filter can be analyzed for the same values of H_{int} as proposed. Figures 3.4 and 3.5 display the frequency responses of (2.32) and (2.33). For the tracking transfer function $G_{LCL}(s)$ in Figure 3.4, higher values of H_{int} provide better damping for the resonance peak at the cost of worse dynamic performance. As with the LC plant, there is no significant change in the gain and phase margin values.

For the output admittance of the LCL filter $Y_{LCL}(s)$, the analyzed values of H_{int} are able to damp both the positive and negative resonances of the filter. As H_{int} increases, the greater is also the damping in these resonances.

In general, the sizing of H_{int} involves a trade-off between dynamic response and disturbance rejection of the controlled plant. Smaller values of H_{int} indicate better dynamic response and worse disturbance rejection, while with larger values the opposite occurs. One way around this trade-off is to use feedforward signals from the disturbance variables to improve the disturbance rejection of the system [30]. As seen in Figure 3.1, the control system uses a feedforward of the voltage

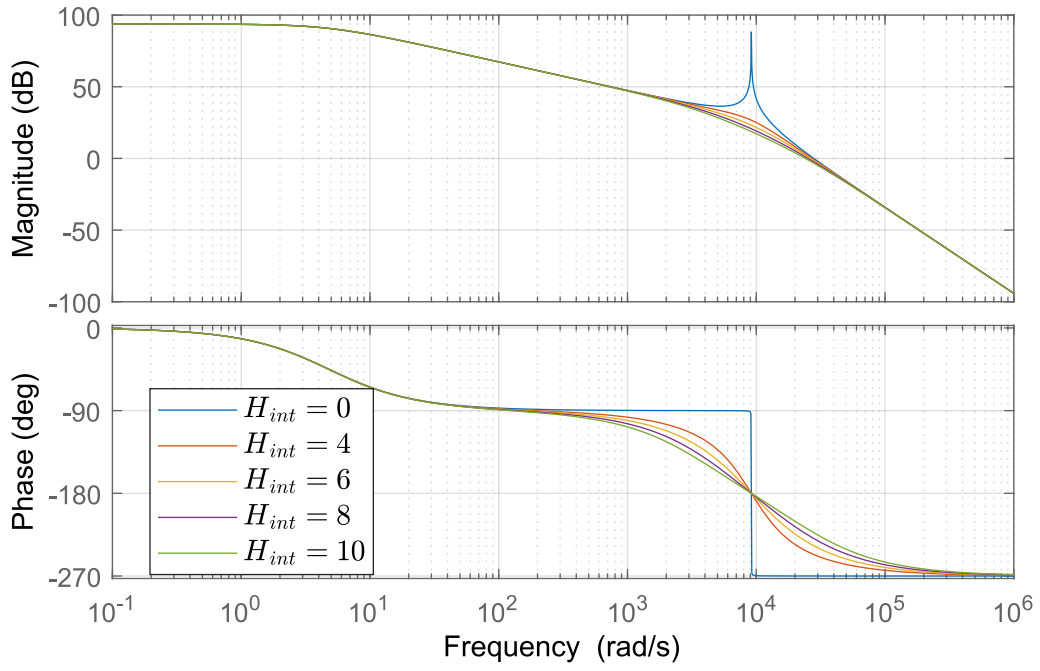


Figure 3.4: Bode diagram of $G_{LCL}(s)$ for different values of H_{int} .

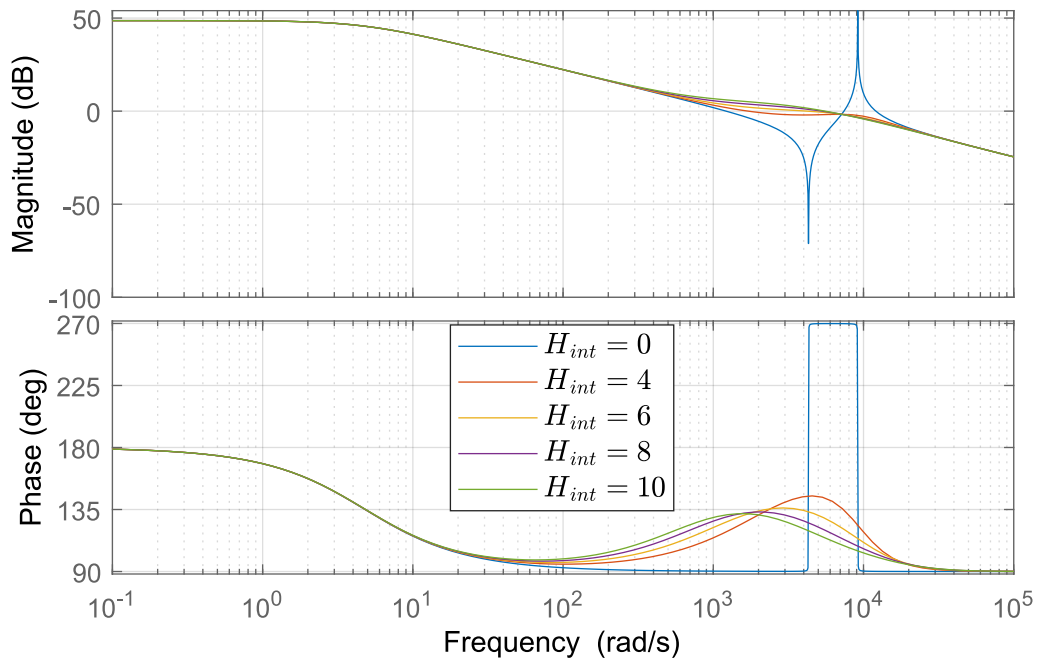


Figure 3.5: Bode diagram of $Y_{LCL}(s)$ for different values of H_{int} .

V_{grid} . Therefore, a better dynamical response is expected for this design, and the lowest value of H_{int} that can achieve the requirements is $H_{int} = 4$.

3.3 Single Loop Voltage Design

Once the value $H_{int} = 4$ has been chosen, the next step is to design the voltage single-loop resonant controller. Here the proper sizing of H_{int} will help in the calculation of this controller. As previously described in Section 2.2, three different types of controller will be sized and compared in this work. These three controllers are the PR ones designed by the Analytical and Gao methods, and the VPI controller designed by pole-zero cancellation, as detailed in Section 2.3.

Both Gao's method for PR and the VPI controller use pole cancellation with zeros as the basis for calculating their gains. However, for this cancellation to be performed, the plant to be controlled needs to be first order. The model of an undamped LC filter is a second order transfer function, so these methods cannot be applied to their full efficiency. The implementation of $H_{int} = 4$ mitigates this problem.

Figure 3.6 displays the step response of the plant to be controlled with and without H_{int} . The response of the system without H_{int} , in blue, is oscillating and has a settling time greater than 3 s, behavior that is not satisfactory and leads to the impossibility of calculating controller gains using the investigated methods. However, when using $H_{int} = 4$, in orange, in addition to the damping of the oscillation coming from the resonance frequency, the system response is much faster, with settling time close to 3 ms. In addition, the response is similar in shape to a first-order system. It is then possible to perform a first-order approximation for use with the pole-zero cancellation methods.

Figure 3.7 illustrates the comparison between the LC filter step response with $H_{int} = 4$, in blue, and first order transfer function $G_{eq}(s)$, in orange. The steady state value K_{eq} is obtained by observing the final step value of $G_{LC}(s)$, while the time constant T_{eq} is obtained by observing the settling time t_s of the step response, considering 98% of the final value, and through the relation $t_s = 4T_{eq}$ [111].

$$G_{eq}(s) = \frac{K_{eq}}{T_{eq}s + 1} = \frac{K_{PWM}K_0K_v}{6.11 * 10^{-4}s + 1} = \frac{1}{6.11 * 10^{-4}s + 1} \quad (3.2)$$

Using this first-order approximation it is then possible to calculate the gains of the PR controller using Gao's method and the VPI controller, plugging K_{eq} and T_{eq} in (2.40) and (2.46), respectively. The desired settling time t_s for the closed-loop system is 4 ms. For these methods the used bandwidth ω_c is calculated as:

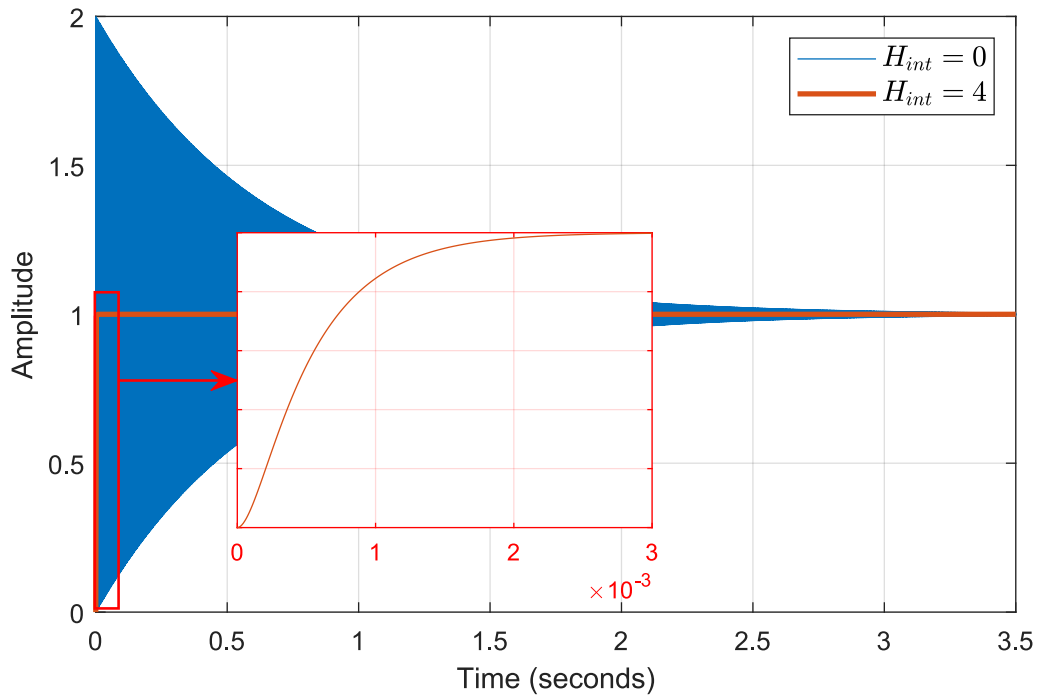


Figure 3.6: $G_{LC}(s)$ step response with and without the designed H_{int} .

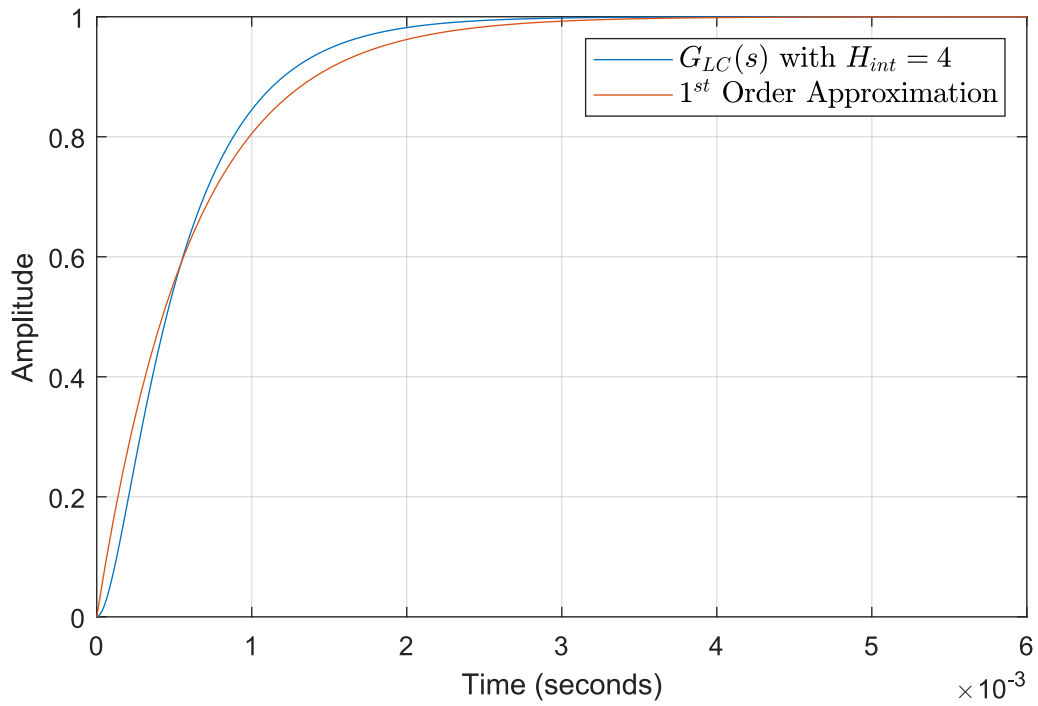


Figure 3.7: Step response comparison between $G_{LC}(s)$ and $G_{eq}(s)$.

$$\omega_c = \frac{4}{t_s} = 1000 \text{ rad/s}, \quad (3.3)$$

since $\omega_c = \frac{1}{\tau_c}$ and $t_s = 4\tau_c$ [111]. It is worth noting that the approximate transfer function $G_{eq}(s)$ is only used to calculate the gains K_P^{Gao} , K_R^{Gao} , K_P^{VPI} , K_R^{VPI} . The further closed-loop analyses use the actual plant $G_{LC}(s)$.

For the Analytic method, the transfer function G_{LC} is used, because there is no need to use a first-order transfer function. To calculate the allocated complex-conjugate poles, the equation (2.43) needs the damping constant ζ and the natural frequency ω_n . Here, $\zeta = 0.7797$ (equivalent to a 2% overshoot). The Analytical method equations do not allow critically damped dynamics (0% overshoot), as stated in Section 2.3, and values smaller than $\zeta < 0.7797$ would instabilize the system. Thus, ω_n is calculated [111]:

$$\omega_n = \frac{4}{t_s \zeta} = 1282.54 \text{ rad/s} \quad (3.4)$$

Table 3.1 exhibits the controllers parameters for the mentioned constraints and system.

Table 3.1: Controller Gains for the LC control Plant.

Design Method	Controller Gains	
	K_p	K_R
Analytical	0.1241	889.68
Gao	0.6110	2000
VPI	0.3055	500

The Bode diagrams for the closed-loop transfer functions $G_{cl}(s)$ – equation 2.27 – and $Z_{cl}(s)$ – equation 2.28 – are illustrated in Figures 3.8 and 3.9, respectively. In these figures, the PR-Analytical (blue), PR-Gao (orange), and VPI (yellow) controllers are compared.

For the Bode diagram of $G_{cl}(s)$, Figure 3.8, in the lower frequency region, the PR-Analytical and PR-Gao controllers have similar behavior, with a horizontal asymptote. The difference is the magnitude of these asymptotes, where PR-Analytical has higher damping compared to PR-Gao. The VPI controller, in turn, presents an increasing asymptote, which characterizes the existence of zeros in its closed-loop transfer function. This can also be verified by analyzing the phase diagram of the controllers, where the VPI starts at low frequencies with a phase equal to 90° and the PR controllers with phase 0° .

In the surroundings of the resonance frequency, approaching from the left, the three controllers have similar behavior. But when approaching from the right, it can be seen that the PR-Analytical controller has a lower cutoff frequency than

the other two controllers, thus meaning a smaller bandwidth. As the PR-Gao and VPI controllers were calculated aiming for the same bandwidth, their decreasing asymptotes are close to each other. This behavior is confirmed when analyzing the high frequencies, where the PR-Analytical controller has greater damping in this region, while the PR-Gao and VPI controllers have similar characteristics.

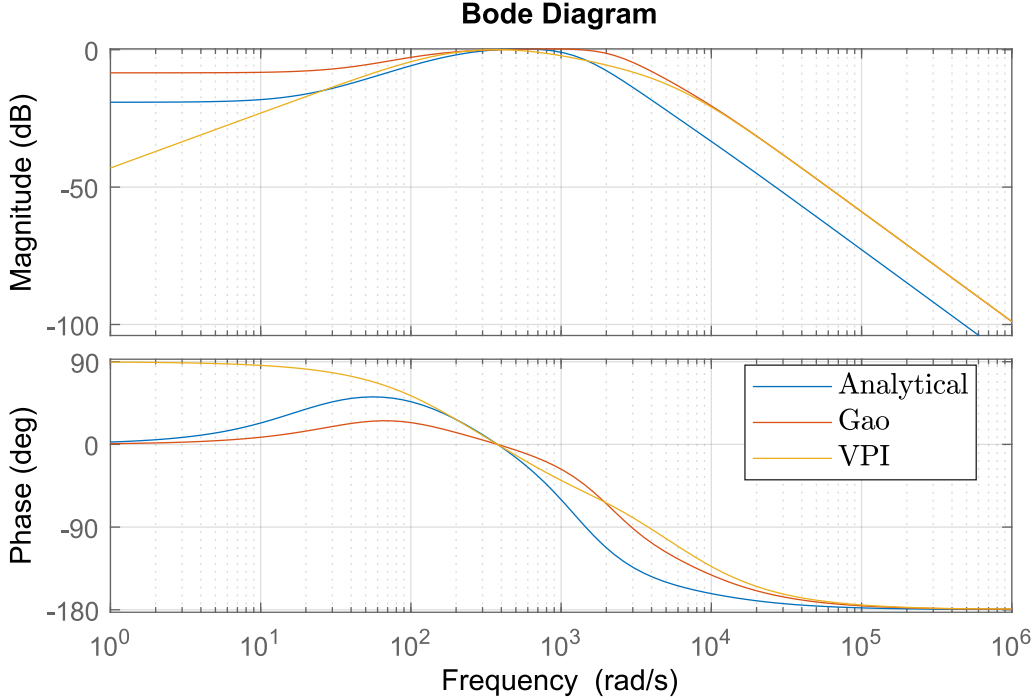


Figure 3.8: Tracking closed-loop Bode diagram for Analytical method (blue), Gao’s method (orange) and VPI method (yellow).

Unlike $G_{cl}(s)$, the Bode diagrams of the different $Z_{cl}(s)$ do not have large differences in both the low and high-frequency regions. It is possible to notice subtle differences in the surroundings of the controller resonance, but not enough to cause differences in the disturbance rejection. These three controllers will be compared dynamically in PSCAD-EMTDC simulation environment.

3.3.1 Reference Generator

The reference generator is responsible for providing the GCC with the voltage to be synthesized by the converter. For this, active and reactive power loops are used. Since the goal of this work is not to deeply analyze the dynamics between the reference generator and the GCC, the simple LPF droop – equation (2.3) – implementation was chosen. Figure 3.10 displays the used scheme.

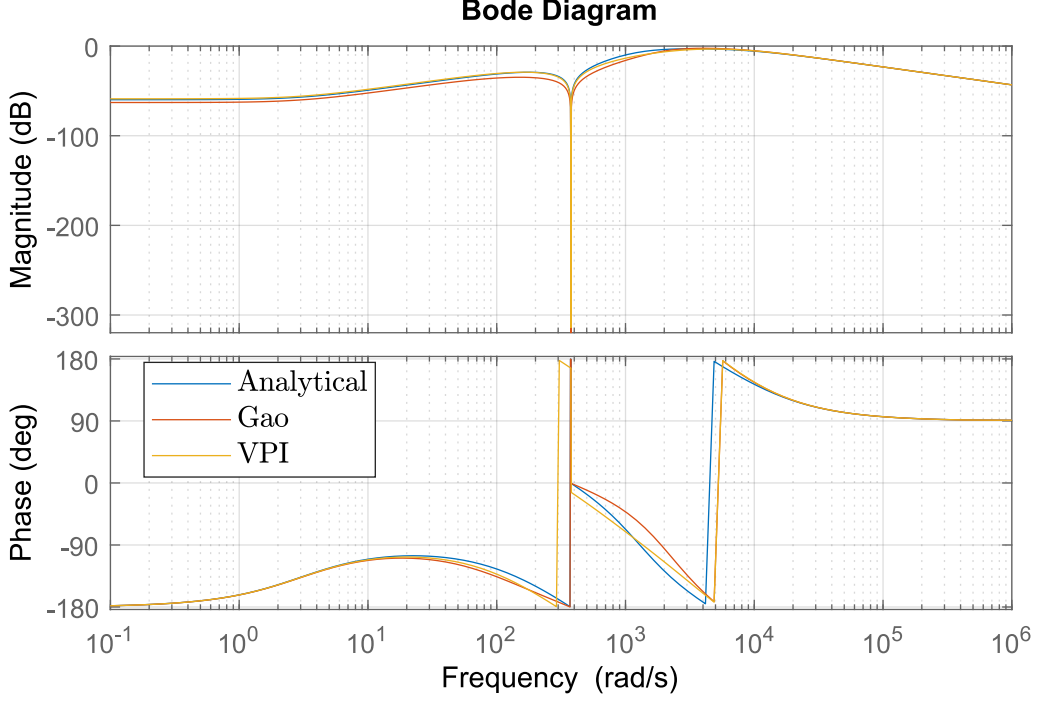


Figure 3.9: Closed-loop converter output impedance Bode diagram for Analytical method (blue), Gao’s method (orange) and VPI method (yellow).

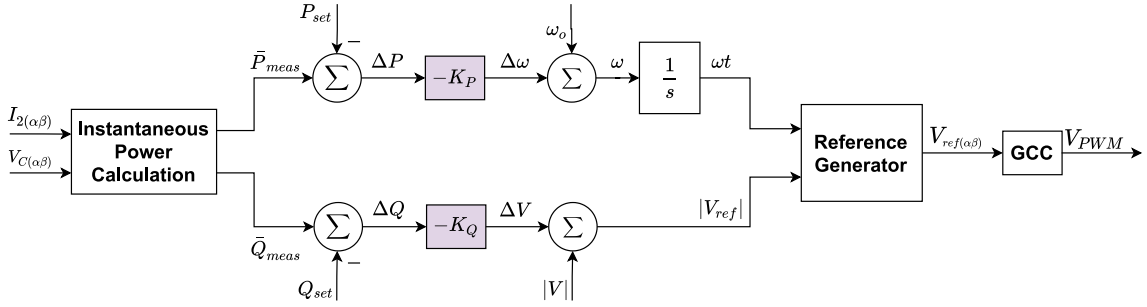


Figure 3.10: Reference generator based on LPF droop controller.

The first stage of the Droop controller is to calculate the instantaneous active (P_{meas}) and reactive (Q_{meas}) powers injected or absorbed by the converter. To do this, the three-phase I_2 and V_C measurements are transformed to the $\alpha\beta$ reference frame via the amplitude invariant Clarke Transform [39, 46]. The powers are calculated as:

$$P_{meas} = V_{C\alpha}I_{2\alpha} + V_{C\beta}I_{2\beta} \quad (3.5)$$

$$Q_{meas} = V_{C\beta}I_{2\alpha} - V_{C\alpha}I_{2\beta} \quad (3.6)$$

The powers P_{meas} and Q_{meas} are then filtered by $G_{LPF}(s)$, with $\tau_{LFP} = 0.001$ s, obtaining the mean values \bar{P}_{meas} and \bar{Q}_{meas} . This filter time constant value translates into a converter with a low ability to provide virtual inertia. However, it is out of

the scope of this work to analyze the impacts of virtual inertia on GCC dynamics.

The mean power values \bar{P}_{meas} and \bar{Q}_{meas} are then compared with the set values P_{set} and Q_{set} , resulting in the active and reactive power deviations ΔP and ΔQ . These deviations are then multiplied by their respective $P - f$ and $Q - V$ droop constants K_P and K_Q , respectively. Both droop constants are defined based on the Brazilian standard PRODIST, (in portuguese, *Procedimentos de Distribuição de Energia Elétrica no Sistema Elétrico Nacional*), which stipulates the operating limits for grid-connected converters [112]. For the frequency variation, the value of $\pm 0.5\%$ was adopted, while for the voltage amplitude, $\pm 7\%$ was adopted.

$$K_P = \frac{\Delta\omega_{max}}{\Delta P} = \frac{0.005}{1.0} = 0.005 \quad (3.7)$$

$$K_Q = \frac{\Delta V_{max}}{\Delta Q} = \frac{0.07}{1.0} = 0.07 \quad (3.8)$$

The value of 0.5% yields a minimum and maximum value of 59.7 Hz and 60.3 Hz, respectively. These frequency values are in accordance with the Brazilian standard for the connection of converters to the utility grid [112], where the electrical system can vary within the limits of 59.5 Hz and 60.5 Hz for a period of 30 s in case of severe contingencies. The more restrictive values for the converter were chosen due to the physical limitations of the real converter present in the laboratory. The same reason can be used for the voltage variations, where the Brazilian standard sets $\pm 10\%$, and the more restrictive value of $\pm 7\%$ was chosen.

The frequency ($\Delta\omega$) and voltage ($|V|$) deviations are then added to the center values ω_0 and $|V|$, respectively. Both $|V|$ and ω_0 were always kept equal to 1.0 pu. During the process of synchronizing and connecting the converter, these values can be received from a PLL for the safe connection of the equipment. Higher hierarchy levels can also change these central droop control values, but it is not the scope of this dissertation.

Once the final ωt and voltage amplitude $|V_{ref}|$ values are calculated, they are used by the GCC as a control reference.

3.3.2 Capacitor Current Filter

In the early stages of the implementation of the controller studied in the PSCAD-EMTDC environment, the high frequency harmonic components of the current I_C instabilized the control, as they were only multiplied by the gain $H_{int} = 4$. This problem of high switching frequencies in the I_C current has already been reported in the literature [75]. To overcome this problem, a first order low-pass filter was used as a solution. This filter would be inserted digitally into the micro-controller, filtering

the current measurements. In this work, this filter is inserted with a continuous transfer function, depicted in (3.9).

The switching frequency of the converter is 5940 Hz, and it is the frequency present at I_C that instabilizes the system. The filter cutoff frequency then is chosen to be at 594 Hz, i.e., ten times lower than the switching frequency. Thus, the time constant τ_f of the filter is calculated:

$$G_f(s) = \frac{1}{\tau_f s + 1} \therefore \tau_f = \frac{1}{2\pi \times 594} = 0.2679 \text{ ms} \quad (3.9)$$

The effect of the adopted low-pass filter can be seen in Figures 3.11 and 3.12, where the closed-loop Bode diagrams for $G_{LC}(s)$ and $Z_{LC}(s)$ of the system are shown, respectively.

For the tracking transfer function $G_{LC}(s)$, there is the addition of a poorly damped resonance peak. In the case of the PR-Gao and VPI controllers, the peak of this resonance is close to 0 dB, while for PR-Analytical this peak is attenuated. For the rest of the frequencies, there are no major changes in the response of the controllers. It is important to note that the addition of $G_f(s)$ was done after the controller gains were calculated, and these were not recalculated after the addition.

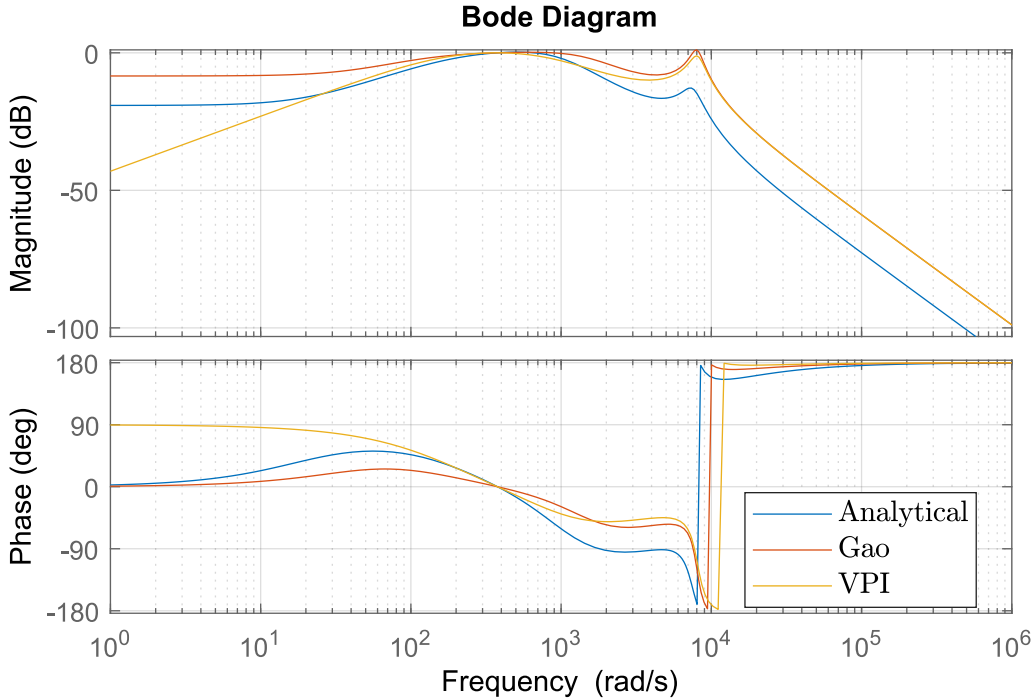


Figure 3.11: Closed-loop converter with capacitor current filter tracking transfer function Bode diagram for Analytical method (blue), Gao's method (orange) and VPI method (yellow).

The same resonance peak appears for the closed-loop output impedance of the $Z_{LC}(s)$ converter. Unlike the Bode diagram of $G_{LC}(s)$, the difference between the controllers in the resonance peak is not significant.

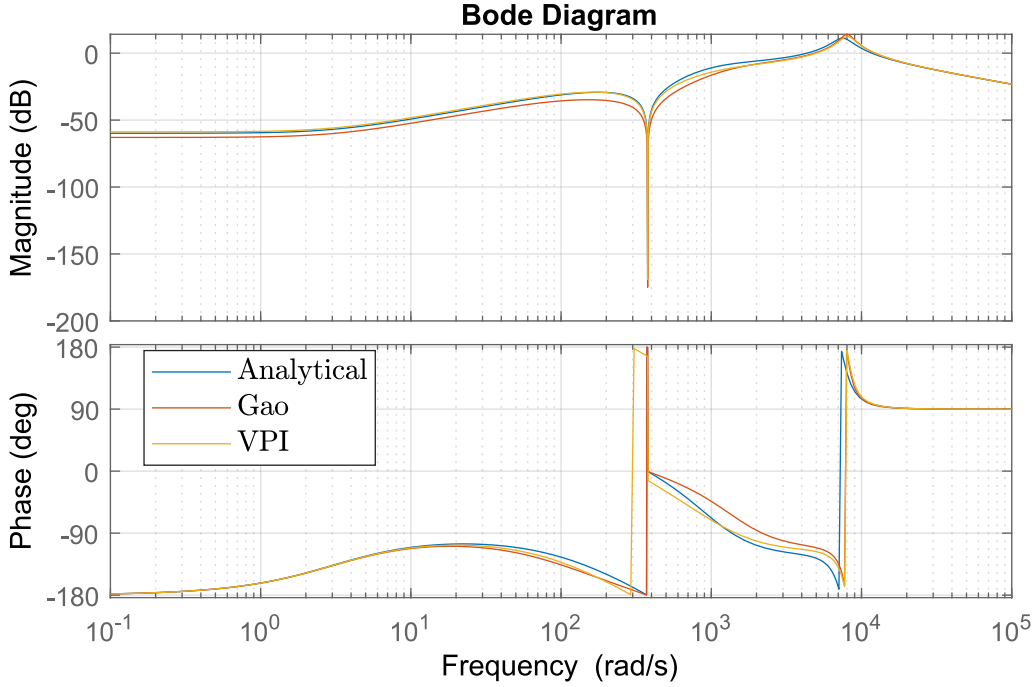


Figure 3.12: Closed-loop converter output impedance with capacitor current filter Bode diagram for Analytical method (blue), Gao’s method (orange) and VPI method (yellow).

3.4 Simulation Results

Simulations for validating the controllers and the inner VI were performed in the PSCAD environment. The simulated system consists of the converter connected to the grid, whose grid inductance L_g and resistance R_g values are arranged in Table 3.2. These values are intended to mimic the LEMT lab scenario, where the converter is connected physically close to the grid, where the impedance of the cables can be ruled out. Figure 3.13 displays the Thévenin equivalent of the simulated system. The simulation was carried on using the complete switched model of the converter, with its LCL filter.

Table 3.2: Simulated grid parameters.

Grid Parameters	
Grid Line Voltage (V_{rms})	220
L_g (mH)	0.214
R_g (m Ω)	4

Three tests were performed: *Dynamic Test*, where the voltage step response of the GCC is validated with droop dynamics disabled; *Power Injection Test*, where the response to the active power step is observed with droop dynamics enabled; and *Voltage Disturbance Test*, where different types of voltage disturbance are applied to compare the performances of the designed controllers.

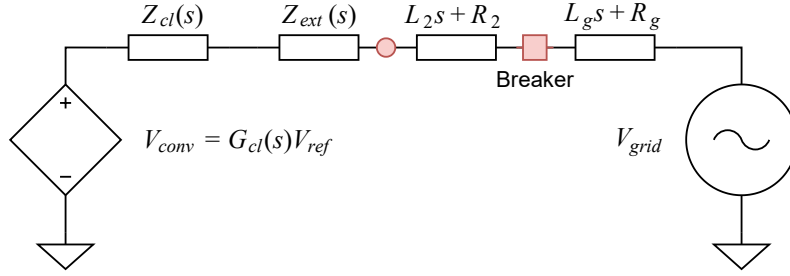


Figure 3.13: Thévenin equivalent of the simulated system for the GCC-GFM-LCL converter. The red point shows the location where P_{meas} and Q_{meas} are calculated.

3.4.1 Dynamic Test

The goal of the *Dynamic Test* is to verify the transient and steady-state behavior under simplified conditions. In this test, the converter will not be connected to the grid and its droop controller will be disabled. The references are then generic sinusoidal signals and there is no load connected at the terminals. In this way, it is isolated from any influence of the droop controller and the grid connection, and the single-loop controller with inner VI can be tested. The following sequence of events is performed during the *Dynamic Test*:

- 0.0 s: the GCC control is enabled, with $|V_{ref}| = 0$ pu;
- 0.05 s: a step of $|V_{ref}| = 1.0$ pu is applied;
- 0.1 s: simulation ends.

Figures 3.14a and 3.14b show the step responses of the $V_{C\alpha}$ and $V_{C\beta}$ components, respectively. From Figure 3.14a it can be seen that the PR-Analytical and VPI controllers have similar dynamics, while the PR-Gao controller has the shortest rising time among the three controllers. The same can be observed in Figure 3.14b. However, the response for the $V_{C\beta}$ component is more oscillatory. The influence of the phase of the reference sine is noticeable for the transient response of the resonant controllers, where $V_{C\alpha}$ is much smoother as it starts from zero and $V_{C\beta}$ is more the oscillatory as the phase corresponds to the negative peak of the sine.

Another way to analyze the response to the reference step is to use the amplitude $|V_C|$, so similar techniques used for DC signals can also be applied. $|V_C|$ can be calculated as:

$$|V_C| = \sqrt{V_{C\alpha}^2 + V_{C\beta}^2} \quad (3.10)$$

Similar conclusions to those obtained earlier can be drawn by analyzing the $|V_C|$ response, illustrated in Figure 3.15a. The PR-Analytical and VPI controllers have similar responses, while the PR-Gao controller has the shortest rise time. However,

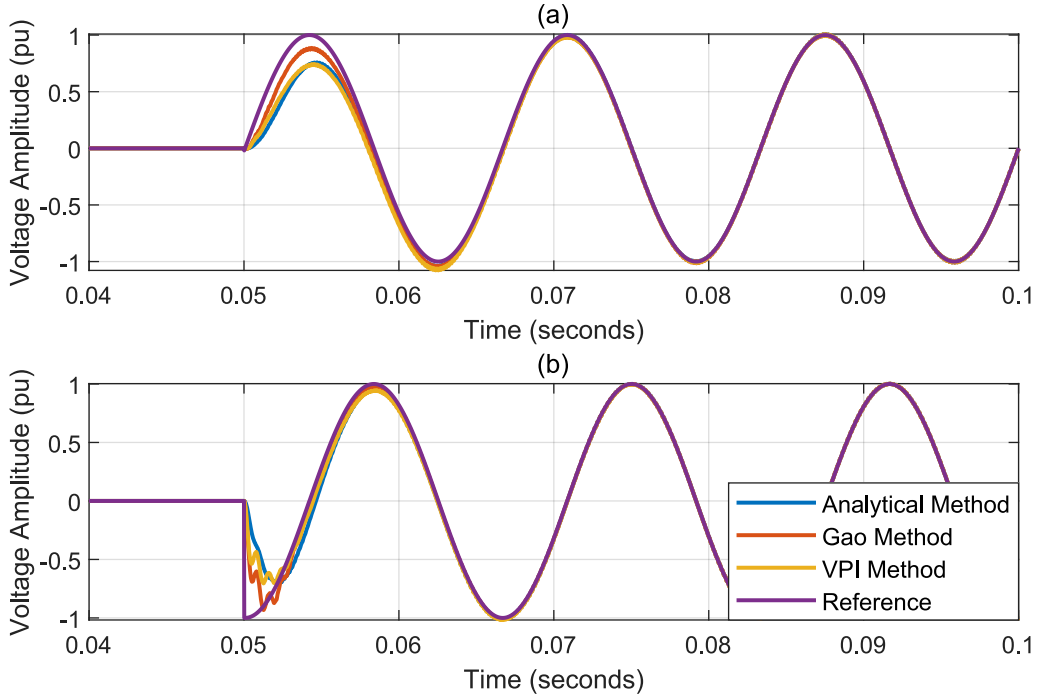


Figure 3.14: Step response for the designed controllers, where the $V_{C\alpha}$ component is observed in (a) and $V_{C\beta}$ component in (b).

it can be seen that the PR-Gao and VPI controllers have a violation to the 1.0 pu amplitude limit, which was not expected due to their resulting first-order behavior. Regarding the steady-state error regulation, illustrated in Figure 3.15b, the controllers are similar and with errors smaller than 1%.

None of the designed controllers achieved the desirable settling time of 4 ms, all of them presenting $t_s > 20$ ms, as illustrated in 3.15a. This type of problem with resonant controllers has already been reported in the literature, where these controllers have great behavior in the steady-state, but do not have the transient response equal to the desired one [110, 113]. The main reason for this is that there is no direct and linear relationship between step amplitude and phase with control quantities such as crossover frequency and bandwidth, as there is with DC signals [113]. The results found here corroborate the reports of these papers.

3.4.2 Power Injection Test

The purpose of the *Power Injection Test* is to test the converter by injecting power into the grid, and with this, all control structures are used. The sequence of events in this test is given by:

- 0.0 s: the GCC control is disabled, and V_{grid} feedforward provides the reference for the PWM;

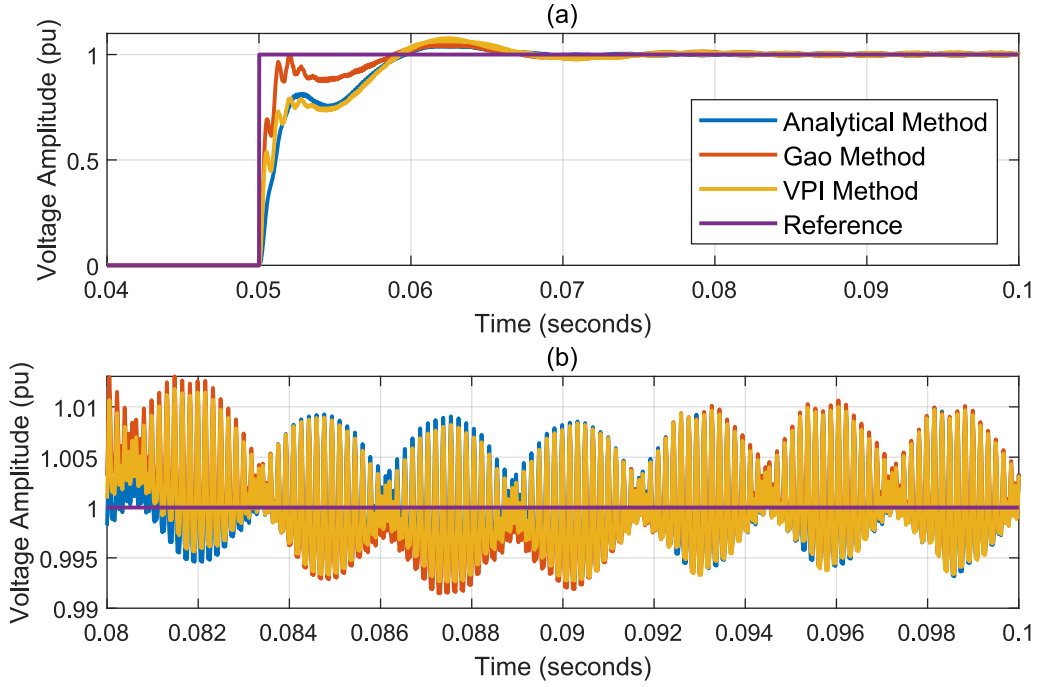


Figure 3.15: Step response for the designed controllers. The dynamics of $|V_C|$ is observed in (a), while in (b) the voltage regulation of the controllers with respect to the reference $|V_{ref}|$ is observed

- 0.05 s: the GCC control is enabled with the PLL generating the voltage reference;
- 0.15 s: the connection breaker is closed, connecting the converter to the grid;
- 0.25 s: the droop loop is enabled, and the PLL no longer generates the voltage reference;
- 0.45 s: a power step, either active (P_{set}) or reactive (Q_{set}), is applied, with the amplitude of 1 pu;

Active Power Step

Figures 3.16a and 3.16b show the dynamics of the active and reactive powers, respectively, after the 1 pu active power P_{set} step. There are no major differences between the controllers regarding the dynamics of \bar{P}_{meas} , besides that the PR-Gao controller has small oscillations and in the VPI controller these are almost non-existent.

Observing the reactive power, it can be seen that it has oscillations, but their amplitudes are smaller than 0.02 pu and their average value is close to 0.0 pu in steady-state. After the active power step there is a brief dynamic of reactive power, but with the amplitude lower than 0.05 pu.

It is noticeable that there is a steady-state error in the active power injected by the converter, which is less than 1 pu. This happens because in the droop controller there are no integrators, so the losses in the conversion and power transmission process will not be zero.

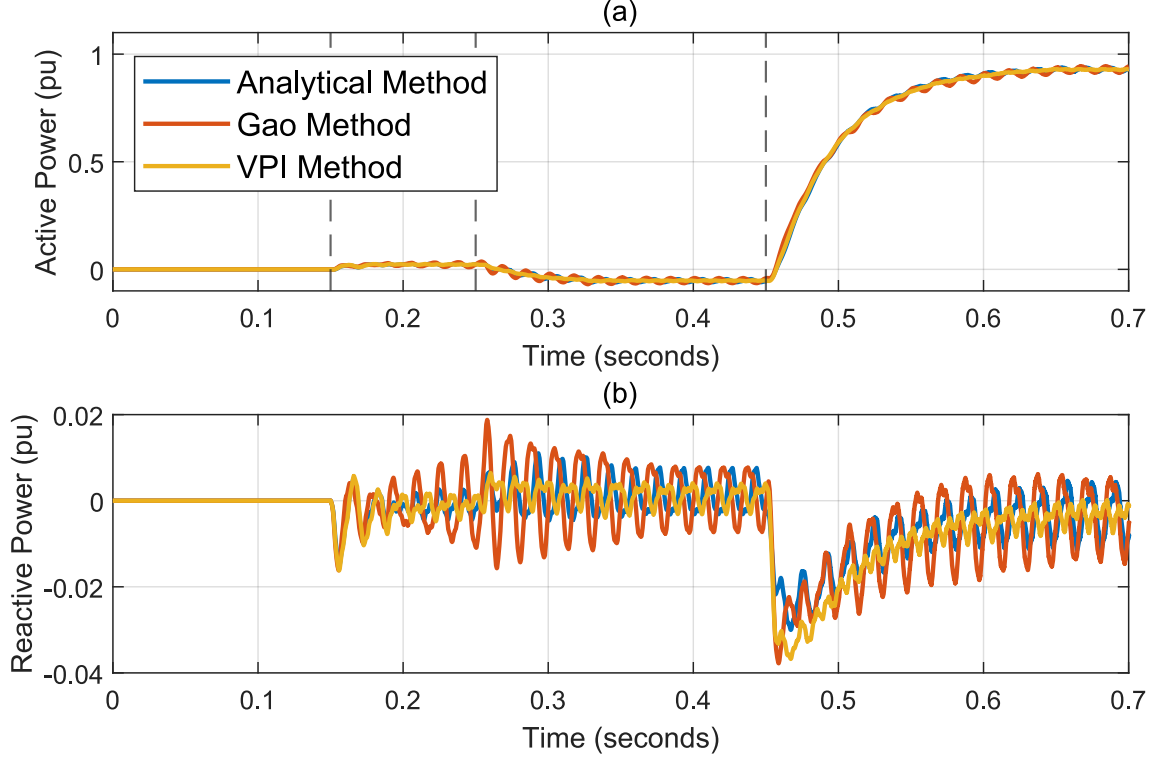


Figure 3.16: Active (a) and reactive (b) powers injected by the converter during the *Power Injection Test* with $P_{set} = 1.0$ pu.

The $|V_C|$ voltage profiles for the different controllers are illustrated in Figures 3.17a, with highlights for the moment that GCC starts to operate in 3.17b and for the P_{set} step in 3.17c. The major difference between the three controllers happens after the GCC controller is enabled, at 0.05 s, and the PR-Analytical controller has the highest overshoot among them. Another phenomenon that can be observed is a small voltage dynamic after P_{set} step in, Figure 3.17c. This happens because after the active power injection, there is a mismatch in the converter reactive power, which is controlled $Q_{set} = 0$ pu, where the reactive absorption in Figure 3.16b justifies this small voltage increase. However, the voltage oscillations seen in Figure 3.17c are less than 1%, meaning that the resonances have been properly damped.

Figure 3.18 illustrates the capacitor current when the converter is injecting $P_{meas} = 1.0$ pu. In blue, the $I_{C\alpha}$ current before the LPF filter, and in orange, after the filtering process. The high frequencies and noises make the system unstable when multiplied by $H_{int} = 4$. When they are removed, the capacitor current resembles a sinusoidal signal, and stability is reached.

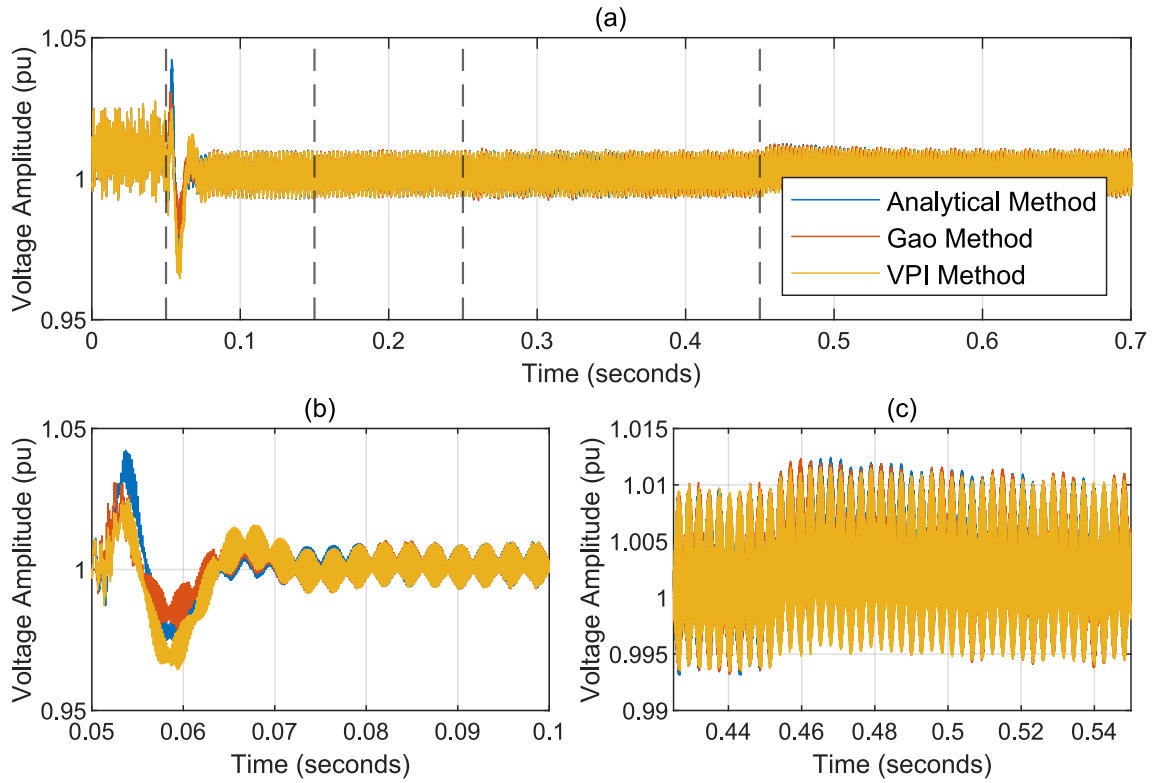


Figure 3.17: Comparison between $|V_C|$ dynamics with PR-Analytical in blue, PR-Gao in orange, and VPI in yellow during the *Power Injection Test* with $P_{set} = 1.0$ pu.

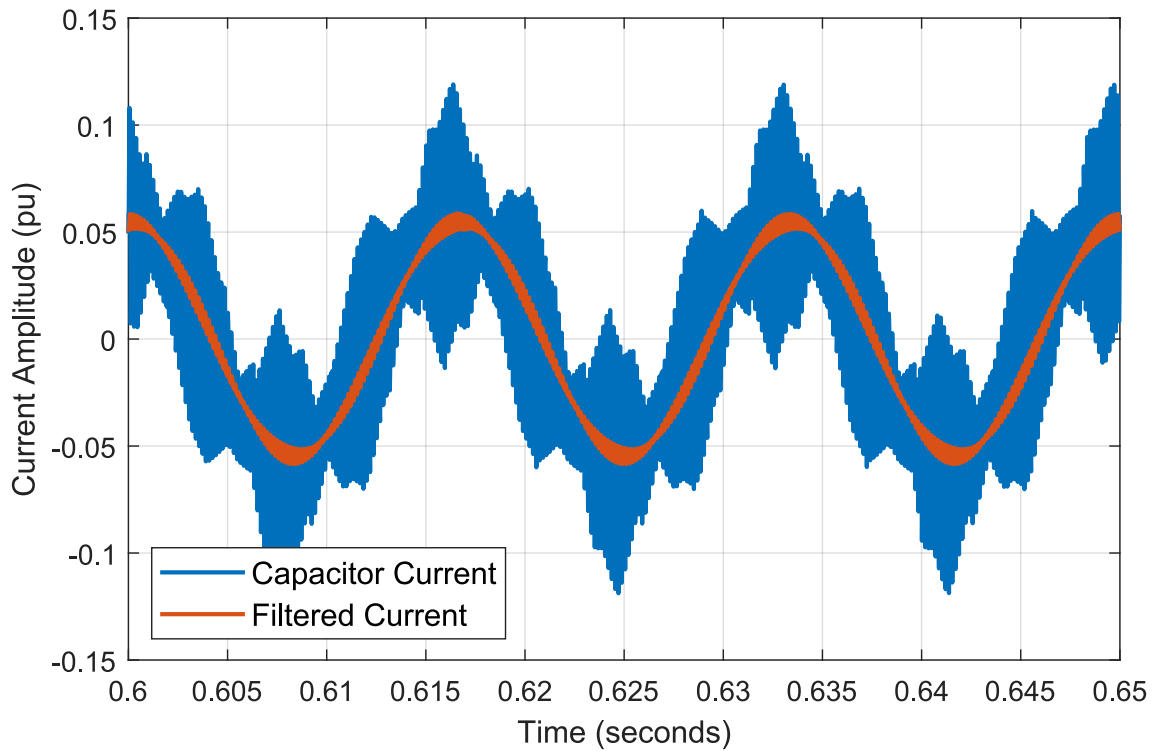


Figure 3.18: Unfiltered capacitor current (blue) and filtered capacitor current (orange).

Reactive Power Step

The same sequence of events is performed here, but the step is now applied for $Q_{set} = 1.0$ pu. Throughout the rest of the simulation, $P_{set} = 0$ pu. Similarly, Figures 3.19a and 3.19b show the dynamics of the active and reactive power injected by the converter.

After the step $Q_{set} = 1.0$ pu, the PR-Gao controller has the largest oscillation amplitude among the compared controllers, and also has the longest settling time, while the VPI controller has the fastest settling time.

Similar dynamic behavior can be observed when analyzing Q_{meas} in Figure 3.19b. However, none of the controllers in question were able to inject the total reference reactive power. In all cases, the reactive power injection limit is close to 0.5 pu, half of the desired Q_{set} . Due to the absence of an integrator in the reactive droop structure, the line impedance connecting the converter to the grid changes the operation point of this controller. Since V_C is being tracked by the single-loop voltage controller, the reactive power is influenced both for the line impedance and the V_C value. Thus, the change of the line impedance will also change the reactive power injected by the converter. This will be explored in Chapter 4.

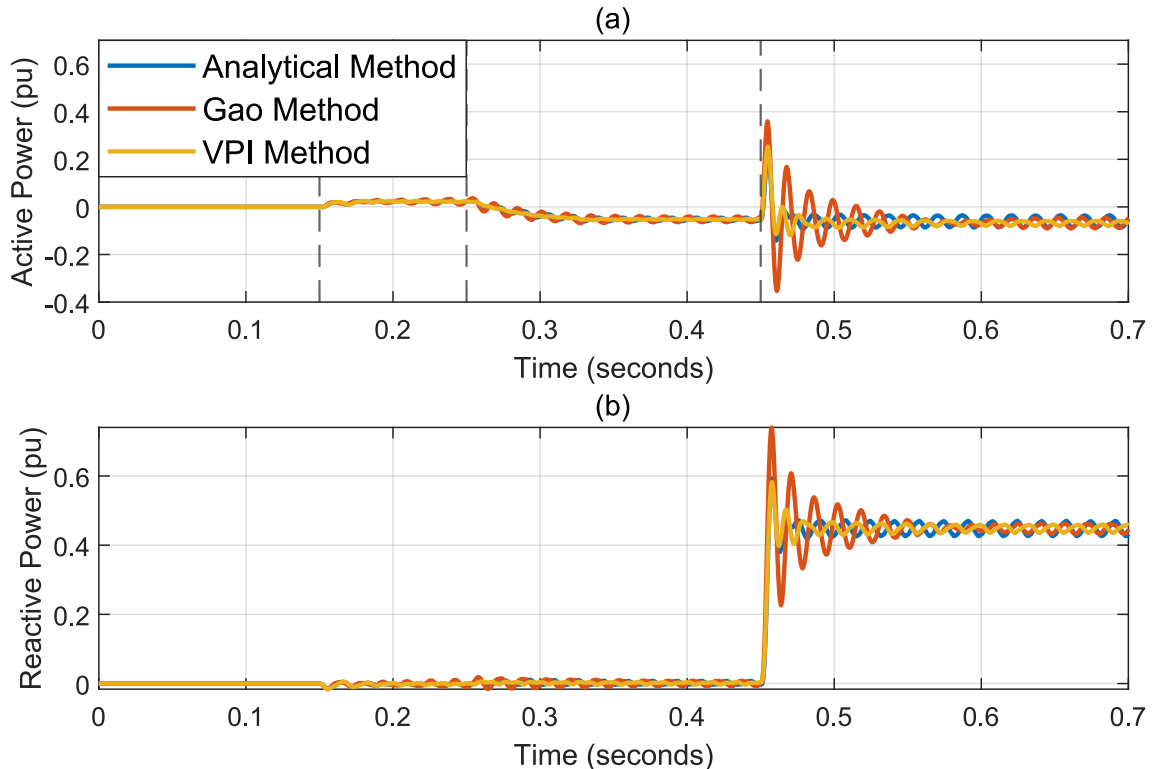


Figure 3.19: Active (a) and reactive (b) powers injected by the converter during the *Power Injection Test* with $Q_{set} = 1.0$ pu.

Figure 3.20a displays the behavior of $|V_C|$ during the simulation. After the Q_{set} step the droop controller acts, causing the voltage to be synthesized to increase to

1.04 pu in order to perform the reactive injection. It can be seen, in Figure 3.20b that there is still a controllability margin by the droop controller, since the 1.07 pu limit was not violated. Moreover, the PR-Gao controller has the largest oscillation after the reference step, while the PR-Analytical and VPI controllers have better damped oscillations.

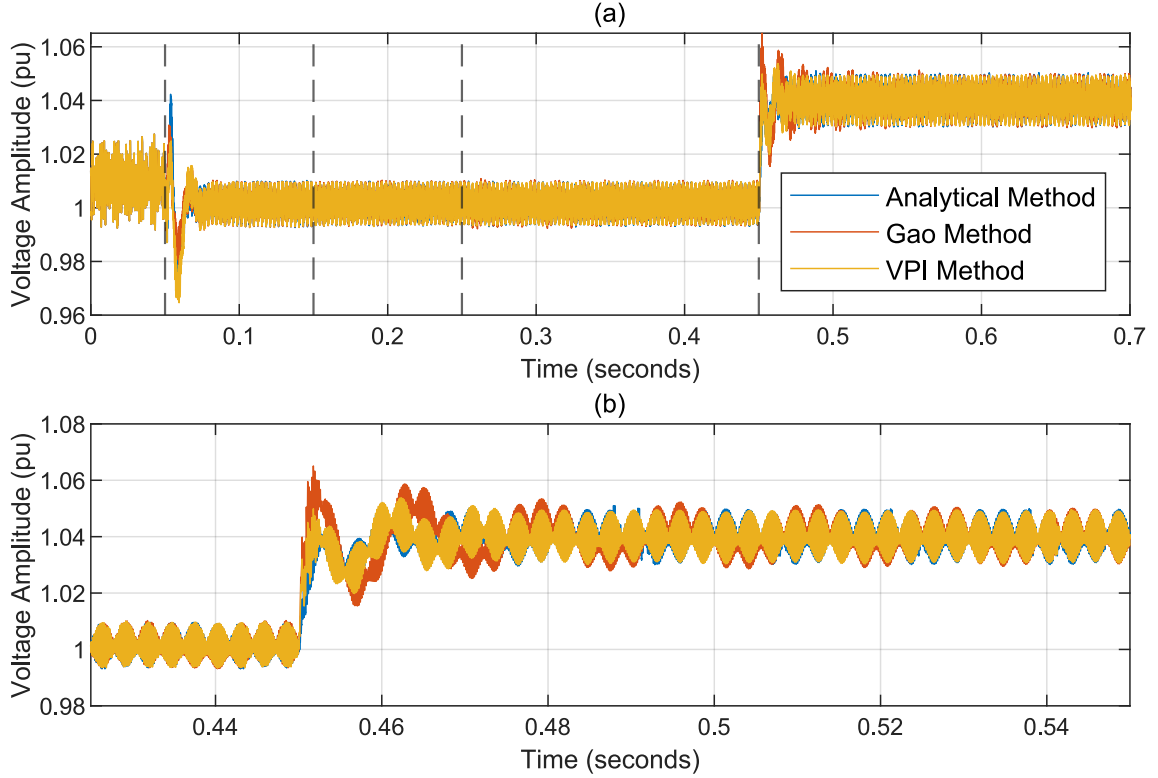


Figure 3.20: Comparison between $|V_C|$ dynamics with PR-Analytical in blue, PR-Gao in orange, and VPI in yellow during the *Power Injection Test* with $Q_{set} = 1.0$ pu. Figure (a) exhibits the whole simulation time, while (b) depicts the voltage dynamics after the reactive step.

3.4.3 Disturbance Rejection Tests

The objectives of the *Disturbance Rejection Tests* is to submit the converter and the designed controllers to the main disturbances they may experience. In this section, two types of disturbances will be analyzed: a 7% voltage sag; and a 0.3 Hz frequency step. These modifications were made by changing the system's AC source. All the disturbances are applied at 1.35 s, after the *Power Injection Test* with $P_{set} = 1.0$ pu is set up. In [26], the GFM-GCC-LCL converter was submitted to single and three-phase faults, and operation under harmonic and unbalanced grid. These disturbances will be studied later in this work, in Section 4.4, for sake of brevity, and since this disturbances are more relevant when the outer VI is present.

Voltage Sag

Figures 3.21a and 3.21b display the voltage $|V_C|$ and current I_2 after the voltage sag at 1.35 s, respectively. It is noticeable in Figure 3.21a that the PR-Analytical controller has the largest undershoot after the sag, reaching close to 0.92 pu in amplitude. Even so, this controller has a similar settling time as the VPI controller, which does not have a similar undershoot. The PR-Gao controller exhibits the same oscillatory behavior shown in the other tests, having a slower settling time when compared to the other two controllers.

Analyzing the phase a from I_2 current dynamics in Figure 3.21b, once again the PR-Gao controller has the largest overshoot and the longest settling time after the voltage disturbance. The PR-Analytical and VPI controllers have similar dynamics, with the PR-Analytical controller having a slightly lower overshoot. Even after the disturbance, the current waveform remains without the high frequency components from the filter resonance.

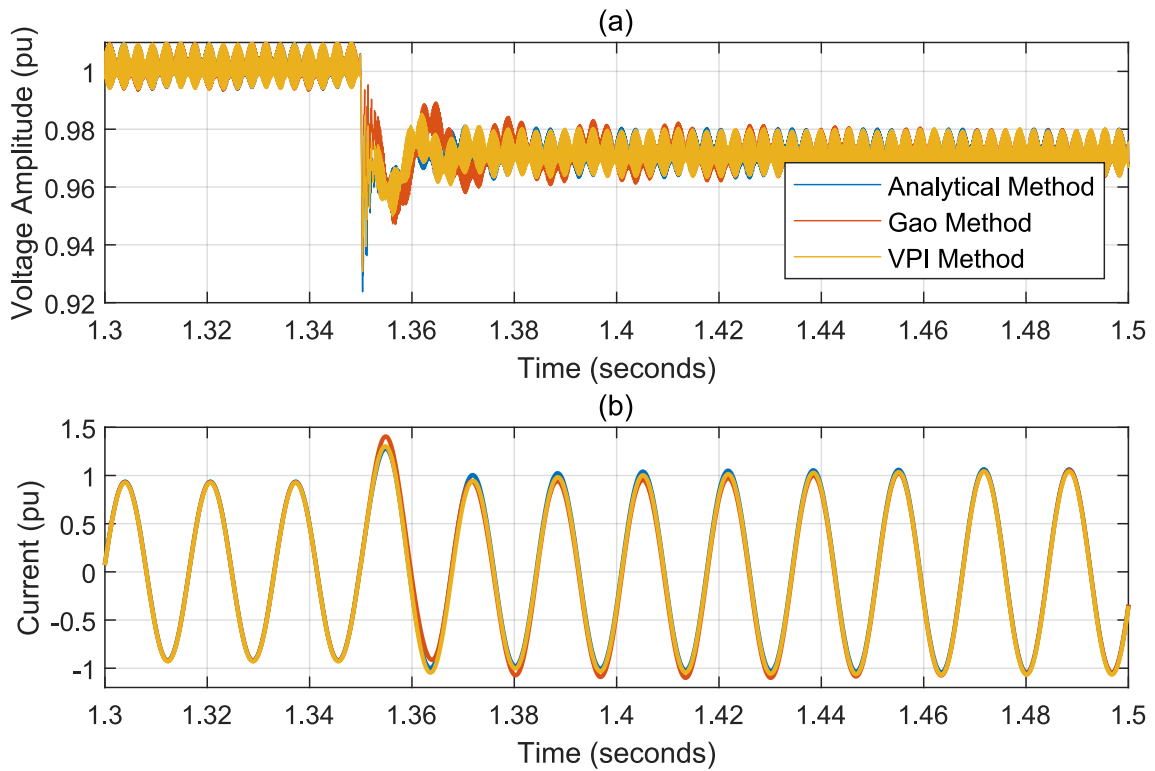


Figure 3.21: Voltage sag responses for the compared controllers, where (a) shows the voltage amplitude $|V_c|$ and (b) the phase a I_2 current.

The power dynamics \bar{P}_{meas} and \bar{Q}_{meas} are arranged in Figures 3.22a and 3.22b, respectively. In both cases, the PR-Gao controller has the highest oscillation and settling time among the compared controllers. In the \bar{P}_{meas} dynamics, this controller has consecutive oscillations where the amplitudes range from 1.2 to 0.6 pu, and could destabilize if it were connected in a real weak grid. A similar effect occurs with the

dynamics of \bar{Q}_{meas} .

Under ideal conditions, the 7% sag would cause the injection of 1.0 pu of reactive power, with $Q_{set} = 0.0$. However, it is observed that the reactive power in the steady-state is slightly larger than 0.4 pu.

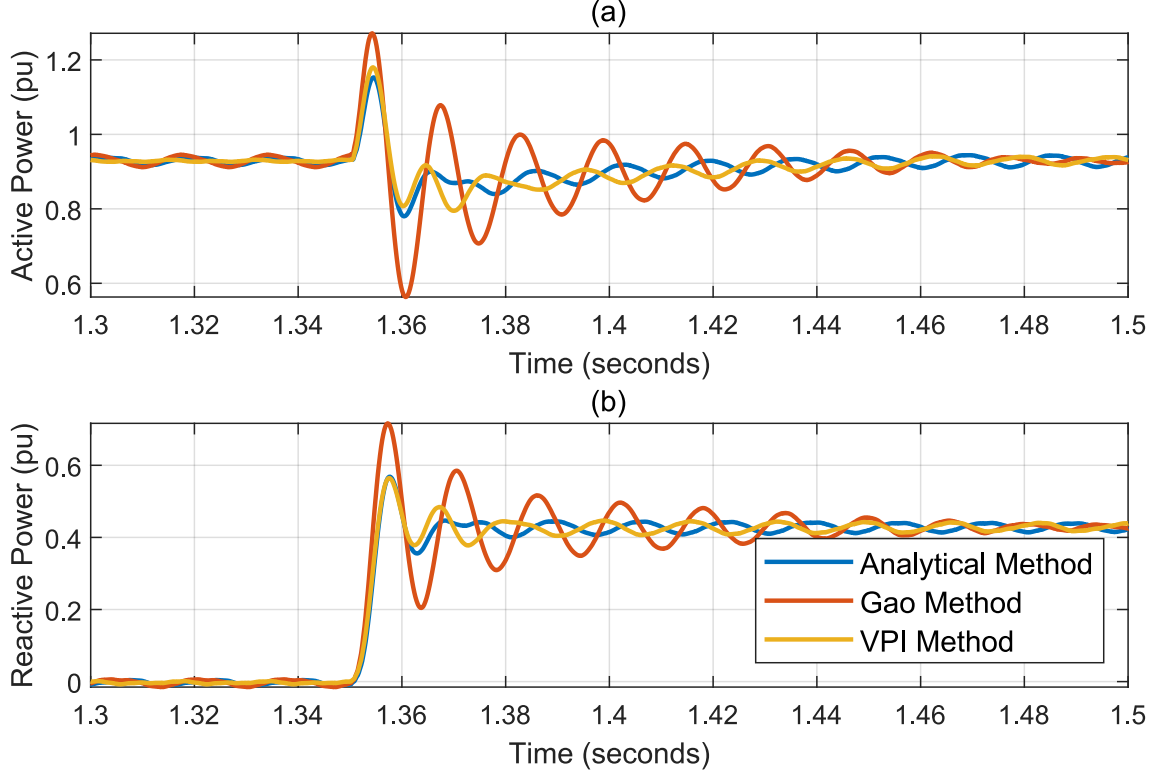


Figure 3.22: Active (a) and reactive (b) powers dynamics of each controller after the 7% voltage sag.

Frequency Step

The second *Disturbance Rejection Test* performed was to give a 0.3 Hz step at 1.35 s in the frequency of the grid equivalent, emulating a loss of load. According to the designed droop controller, with the converter following the reference of $P_{set} = 1.0$ pu, this step of 0.3 Hz will cause the converter to have to stop injecting active power, i.e. $\bar{P}_{meas} = 0.0$ pu. Figures 3.23a and 3.23b display the frequency and \bar{P}_{meas} behavior, respectively.

There are no major differences in the frequency and active power dynamics. As expected, the active power has adjusted to near zero. The value is not exactly zero because the droop controller has no integrators, so the converter is compensating for system losses, and this explains the negative power value. The frequency measurement is taken from the droop controller calculation, and therefore shows a little above 60.3 Hz.

Figures 3.24a and 3.24b display the dynamics of $|V_C|$ and I_2 after the frequency

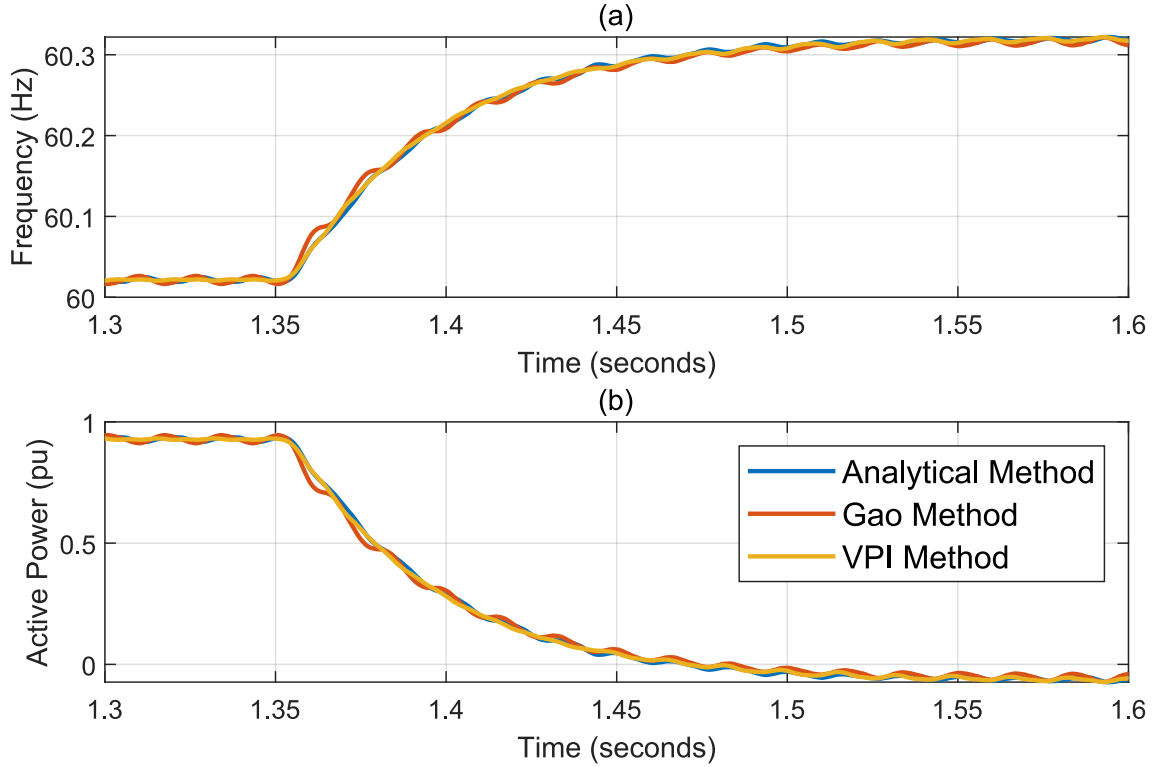


Figure 3.23: Frequency droop dynamics (a) for each compared controllers and active power injection responses (b) before and after the 0.3 Hz frequency step.

step. In both cases, there are no notable differences between the three controllers. After the disturbance, the controllers exhibit a small sinking smaller than 1%, showing no influence of the disturbance on voltage regulation, as illustrated in Figure 3.24a. The dynamics of the current I_2 , in Figure 3.24b, also shows no differences between the controllers in question.

3.5 Partial Remarks

The inner VI design was presented, with the goal of damping both the resonance of the LC filter – the controlled plant – and the converter’s intrinsic LCL filter. Since the control system uses a feedforward of the grid voltage, and disturbance rejection is improved due to this, the smallest possible value of H_{int} was chosen. This is because the choice of H_{int} is a trade-off between dynamic response and disturbance rejection.

The design of H_{int} also made it possible to calculate the voltage single-loop controller. With the damping of the filter resonance, the Analytical method found stable values for the controller. For the Gao and VPI methods, which require a first order transfer function for the cancellation of zero poles, the use of H_{int} allowed a feasible first order approximation for the system, enabling the proper use of these techniques.

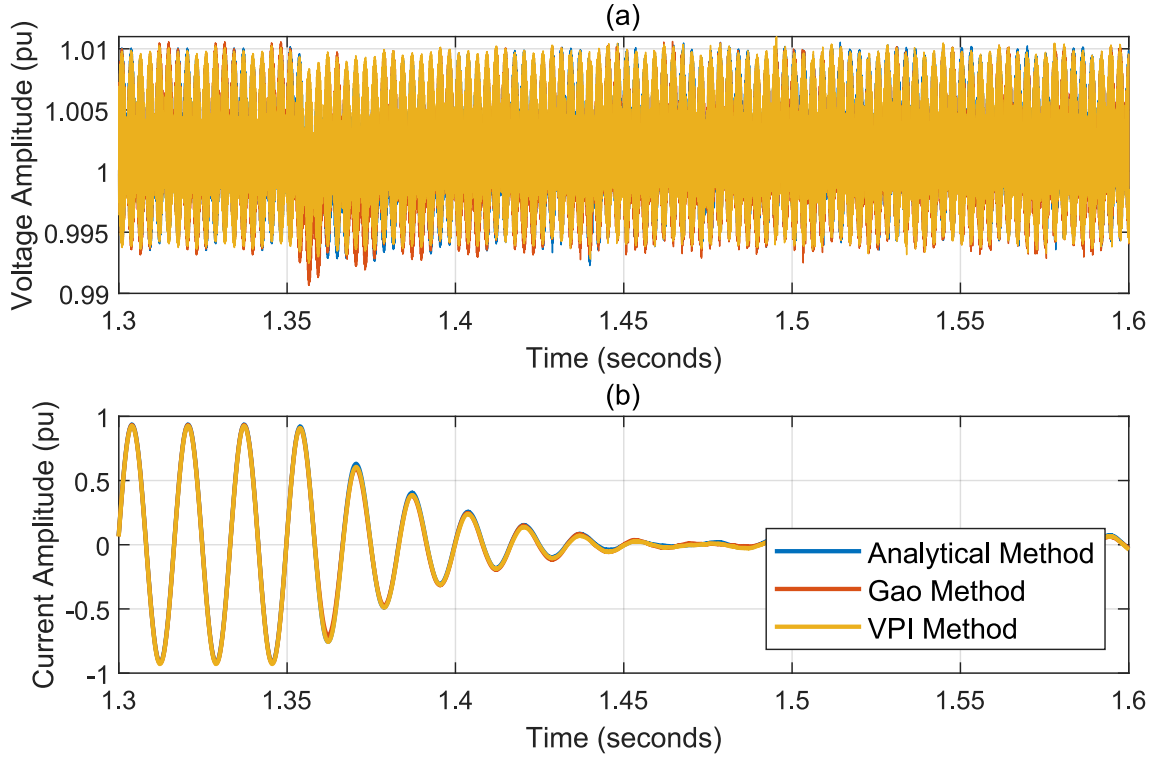


Figure 3.24: Frequency step responses for the compared controllers, where (a) shows the voltage amplitude $|V_c|$ and (b) the phase *a* current.

The controllers were then compared with each other. Although there are no overall differences between the controllers, a few points can be discussed. The first point is that none of the controllers had the projected settling time of 4 ms, having values greater than 20 ms. To contour this problem, in [113], it was proposed an additional resonant term is added to yield the desired response. In [110], the settling time problem was diminished by using complex variable resonant control with a proper pole-zero cancellation technique. The second one is that Gao's controller showed oscillatory behavior from the point of view of power dynamics, translating less intensely to voltage dynamics. Although the PR-Analytical and VPI controllers also had these oscillations, the PR-Gao had the largest of the amplitudes.

The main thing to discuss is the fact that the converter was not able to fully inject the required reactive when $Q_{set} = 1.0$ pu. As the reactive droop loop does not have a integral term in its controller, the line impedance will change the operation point of the $Q - V$ curve. In this way, as V_C is tracked by the single-loop controller, the reactive power injected by the converter will be that which results in the desired V_C voltage. The use of negative virtual inductance to reduce the total line inductance can be a solution to this problem. Therefore, the implementation and design of the outer VI in the next section will have this focus.

Chapter 4

Outer Virtual Impedance Design

A review of the different functions and implementations of Outer Virtual Impedance is provided. After that, the design methodology is explained as well as simulation results. Partial remarks are drawn from the discussion of the results.

4.1 Outer Virtual Impedance Literature Review

Unlike the inner VI, the outer VI has a wide range of functions and applications. They can be divided into four categories: active stabilization, power flow control, harmonic and unbalance compensation, and current limitation and fault-ride through capabilities [25]. Although the application used in this dissertation is to enhance the reactive power injection by the converter, which can be categorized in the power flow control group, a brief explanation of the other three groups is given. The power flow control application will be presented last because it will be the most in-depth.

Active stabilization involves damping subsynchronous oscillations that can be caused by PLL [114–117], voltage fluctuation in DC links [118], or active and reactive power control [119, 120]. To solve this problem, virtual resistors are typically used to increase the damping of these frequencies [121, 122].

The virtual resistor technique is also used for the attenuation of low-order harmonics, because the active filter in question behaves like a resistor [123]. For specific higher-order harmonics, the use of virtual inductances appears to be a solution [124, 125]. The use of virtual resistance and impedance structures also helps in sharing nonlinear loads by converters operating in parallel [126, 127].

Unbalance of three-phase voltages is a common phenomenon in distribution networks. The use of virtual resistors can also mitigate this problem, by using them only for negative sequence, responsible for the unbalance [128, 129].

A common method for current limiting is the use of adaptive virtual impedance [121, 130–132]. This type of structure modifies the value of the virtual impedance after fault detection. When the system is healthy, low values are used, so as not to hinder the injection of power, but after the fault detection the control increases the values of the virtual impedance in order to limit the current.

The use of virtual impedances for power flow control can be categorized in two ways: ensuring decoupling between active and reactive powers by manipulating the line impedance ratio X_L/R [121, 133, 134]; and improving power sharing between converters operating in parallel, especially reactive power [121, 135, 136]. Most often, the implementation of a virtual resistor with a virtual inductance is used.

Two main techniques are used to implement this combination of virtual inductance in series with the virtual resistor: the first is to apply using the form $R_v + sL_v$ – where R_v is the virtual resistor and L_v is the virtual inductance – which is a transfer function with derivative action, and sL_v [24]; and the form $R_v + j\omega L_v$ where the value of $j\omega L_v$ is constant for the entire frequency spectrum [60, 121]. Usually, the second technique is the most used because of the noise amplification problems due to the derivative action [60, 121].

4.2 Methodology

As seen in the reactive power injection and voltage sinking test results in Section 3.4, the studied converter is not able to inject the desired reactive power when $Q_{set} = 1.0$ pu. One possible solution is to reduce the line impedance in order to improve the reactive power injection. This requires the use of negative virtual impedance to reduce the total line impedance.

The use of negative virtual inductance and resistors has already been reported in the literature. Negative resistors are normally used to improve the X_L/R ratio of the line [121, 137]. The use of negative virtual inductance is associated with the context of flexible ac transmission systems (FACTS) [138, 139], but recently they have been used in the context of grid-connected converters [140]. In the context of power flow improvements, there are no publications or methodologies for design negative virtual inductance.

In [121], the same authors He and Li proposed a methodology for calculating positive virtual inductance for power flow and system stability improvement, and for decoupling the active and reactive powers. The study presents a simplified modeling, considering only the fundamental frequency of a grid-connected converter, and from this modeling the classical power flow equations are applied and virtual impedance is used to improve these injections. From the study of the eigenvalues of the power control loops, the only ones modeled in this study, the stability of the grid-connected and also islanded converter is studied. From these criteria, the virtual impedance is calculated and implemented in the form of $R_v + j\omega L_v$, where R_v is the virtual resistance and L_v the virtual inductance.

In this dissertation, He and Li's method will be applied in a modified form. The power flow study will be maintained with minor changes. However, the stability study and virtual impedance analysis will be modified. While in [121] only a modeling for fundamental frequency is considered, here the total output impedance of the converter $Z_{out}(s)$ will be analyzed, considering then the whole frequency spectrum of the GFM converter. Furthermore, the islanded operation will not be considered here. The implementation will be done in the form suggested by He and Li, i.e., $R_v + j\omega L_v$. Since the studied converter has an LCL filter, using a negative virtual impedance in the form $R_v + sL_v$ may deteriorate the filtering of the high frequencies. Since the implementation $R_v + j\omega L_v$ has an equal amplitude value for all frequencies, this deterioration will be smaller. In the following, the used method will be described.

4.2.1 Power Flow Analysis

The power flow analysis is done from the viewpoint of the fundamental frequency of 60 Hz, since this is the desirable frequency to transmit power. In this way, one can simplify the output impedance Z_{out} of the converter. This impedance is defined as:

$$Z_{out}(s) = Z_{cl}(s) + Z_{ext}(s) + L_2s + R_2 \quad (4.1)$$

Note that from the Bode diagram of $Z_{cl}(s)$ of all the controllers analyzed, in Figure 3.12, the magnitude value – at the fundamental frequency to which they are tuned – is less than -150 dB, i.e., ≈ 0 pu. This means that it can be neglected in the power flow analysis.

Similar analysis can be done for the resulting outer VI $Z_{ext}(s)$. As:

$$Z_{ext}(s) = H_{ext}(s)G_{cl}(s) = -(R_v + j\omega L_v)G_{cl}(s), \quad (4.2)$$

it can be seen that the impedance $Z_{ext}(s)$ depends on $G_{cl}(s)$. Analyzing its Bode diagram in Figure 3.11 at the fundamental frequency, $G_{cl}(s) \approx 0$ dB, i.e., ≈ 1.0 pu. Thus, for the power flow analysis, $Z_{ext} = -(R_v + j\omega L_v)$. The second filter inductance L_2 and its parasitic resistance R_2 can be rescripted from $R_2 + sL_2$ to $R_2 + j\omega L_2$. The same is true for the grid impedance, which can be rewritten as $R_g + j\omega L_g$. Thus, the connection impedance between the converter and the grid can be rewritten as:

$$Z_{line} = jX_2 + R_2 + jX_g + R_g - jX_v - R_v \quad (4.3)$$

In which X_2 , X_g and X_v are the inductive reactances of L_2 , L_g and L_v , respectively. From these definitions, the line admittance can be described using phasor notation, where Y is the admittance magnitude and ϕ is its phase:

$$Y \angle \phi = \frac{1}{R_{line} + jX_{line}} \quad (4.4)$$

With these definitions, the power flow equations can be calculated using:

$$\begin{cases} P = (V_{conv}V_{grid}Y \cos \theta - V_{grid}^2Y) \cos \theta - V_{conv}V_{grid}Y \sin \phi \sin \theta; & (4.5) \\ Q = (V_{grid}^2Y - V_{conv}V_{grid}Y \cos \theta) \sin \theta - V_{conv}V_{grid}Y \cos \phi \cos \theta & (4.6) \end{cases}$$

Where θ is the power angle from the converter voltage in relation to V_{grid} , which is the reference. All the elements in this equation are normalized so that the powers are in the per unit system. The maximum powers generated must be greater than

the powers P_{demand} and Q_{demand} demanded by the grid [121]. This occurs when θ and V_{conv} are at their maximum values θ_{max} and V_{max} . This is the first limit that must be respected.

The second limit involves the decoupling between active and reactive power. He and Li proposed the following relations in [121]:

$$\left\{ \begin{array}{l} |\partial P/\partial\theta| \geq K_{decouple} \geq |\partial Q/\partial\theta| \end{array} \right. \quad (4.7)$$

$$\left\{ \begin{array}{l} |\partial Q/\partial V_{conv}| \geq K_{decouple} \geq |\partial P/\partial V_{conv}| \end{array} \right. \quad (4.8)$$

$K_{decouple}$ is a decoupling coefficient, governing the relationship of the partial derivatives $\partial P/\partial\theta$, $\partial P/\partial V_{conv}$, $\partial Q/\partial V_{conv}$ and $\partial Q/\partial\theta$, defined as:

$$\left\{ \begin{array}{l} \partial P/\partial\theta = YV_{grid}V_{conv} \sin(\theta - \phi) \end{array} \right. \quad (4.9)$$

$$\left\{ \begin{array}{l} \partial P/\partial V_{conv} = 2YV_{conv} \cos\phi - YV_{grid} \cos(\theta - \phi) \end{array} \right. \quad (4.10)$$

$$\left\{ \begin{array}{l} \partial Q/\partial V_{conv} = -YV_{grid}V_{conv} \cos(\theta - \phi) \end{array} \right. \quad (4.11)$$

$$\left\{ \begin{array}{l} \partial Q/\partial\theta = -2YV_{conv} \cos\phi - YV_{grid} \sin(\theta - \phi) \end{array} \right. \quad (4.12)$$

The above partial derivatives represent the level of coupling between the variables. A high value of $|\partial P/\partial\theta|$ means that the active power P will suffer great influence from θ , as an example. Thus, the equations 4.7 and 4.8 say that to achieve the desired $P - f$ and $Q - V$ decoupling, $\partial P/\partial\theta$ and $\partial Q/\partial V_{conv}$ must be $K_{decouple}$ times greater than $\partial Q/\partial\theta$ and $\partial P/\partial V_{conv}$, respectively.

Although [121] provides these relationships, an in-depth analysis of $K_{decouple}$ was not presented, and it turns out to be an abstract relationship to understand. In [121], it is also cited that the X_L/R ratio of the connection must be greater than $K_{decouple}$. So the proposition of this dissertation is to use the X_L/R ratio as a constraint, instead of the above equations. Besides being more compact and simple, the electrical interpretation is easier to understand.

4.2.2 Impedance Analysis

As explained previously, the power flow analysis looks only at the converter-grid system from the grid frequency ω_{set} . This brings a number of limitations to the stability analysis. Outside the fundamental frequency, the output impedance of the converter $Z_{cl}(s)$ cannot be neglected, as well as the resulting impedance $Z_{ext}(s)$ changes, since $G_{cl}(s) \neq 1$ for different frequencies.

Other impacting effects of implementing $H_{ext}(s)$ also need to be presented and taken into consideration when analyzing stability. When using the implementation in the form $R_v + j\omega L_v$, it is not simple to apply the complex number j in onboard

microcontrollers. A possible solution is to use the $I_{2(\alpha\beta)}$ current coupling [60, 121], as illustrated in Figure 4.1.

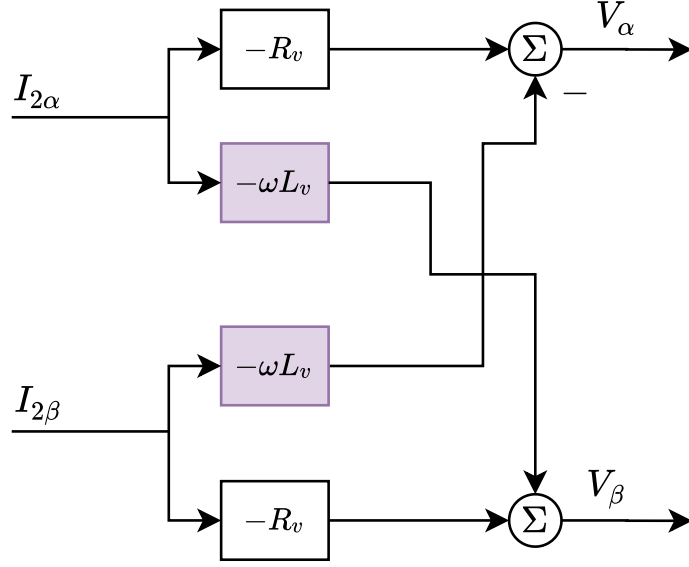


Figure 4.1: Virtual impedance implementation using current coupling technique.

This form of implementation creates coupling between the $\alpha\beta$ axes, i.e., effects that only occur in the α component now impact the β component, and vice versa. A very common example are controllers applied to dq axis, axes that are naturally coupled to each other, and that use decoupling feedforwards to remove this phenomenon. This changes the way the system is modeled and analyzed, and one way to deal with this is to use the concept of complex transfer functions [60, 116, 141].

Complex vector modeling is a consequence of transfer matrix modeling, used when a system is multiple-input and multiple-output (MIMO) . Through simplifications due to the symmetry of the mathematical model of the converter, we can simplify the MIMO model to a single-input and single-output (SISO) model. The general modeling of a transfer matrix on the $\alpha\beta$ axis is:

$$\underline{y}_{\alpha\beta} = G_{\alpha\beta}^m(s)\underline{u}_{\alpha\beta} \rightarrow \begin{bmatrix} y_\alpha \\ y_\beta \end{bmatrix} = \begin{bmatrix} G_{\alpha\alpha}(s) & G_{\alpha\beta}(s) \\ G_{\beta\alpha}(s) & G_{\beta\beta}(s) \end{bmatrix} \begin{bmatrix} u_\alpha \\ u_\beta \end{bmatrix} \quad (4.13)$$

Where $y_\alpha, y_\beta, u_\alpha, u_\beta$ are the outputs and inputs of the system in the α and β components. $G_{\alpha\alpha}(s)$ and $G_{\beta\beta}(s)$ are the self-transfer functions for the α and β components, while $G_{\beta\alpha}(s)$ $G_{\alpha\beta}(s)$ are the mutual transfer functions between the components. To transform from Transfer Matrix form to Complex Vector form, using the transformation:

$$\begin{cases} \underline{y}_{\alpha\beta\pm} = T\underline{y}_{\alpha\beta} & (4.14) \\ \underline{u}_{\alpha\beta\pm} = T\underline{u}_{\alpha\beta} & (4.15) \\ G_{\alpha\beta\pm}^m(s) = TG_{\alpha\beta}^m(s)T^{-1} & (4.16) \\ T = \begin{bmatrix} 1 & j \\ 1 & -j \end{bmatrix} & (4.17) \end{cases}$$

Thus, the generic complex vector form is:

$$\underline{y}_{\alpha\beta\pm} = G_{\alpha\beta\pm}^m(s)\underline{u}_{\alpha\beta\pm} \rightarrow \begin{bmatrix} y_{\alpha\beta+} \\ y_{\alpha\beta-} \end{bmatrix} = \begin{bmatrix} G_{\alpha\beta+}(s) & G_{\alpha\beta-}(s) \\ \overline{G}_{\alpha\beta-}(s) & \overline{G}_{\alpha\beta+}(s) \end{bmatrix} \begin{bmatrix} u_{\alpha\beta+} \\ u_{\alpha\beta-} \end{bmatrix}, \quad (4.18)$$

where:

$$\begin{cases} G_{\alpha\beta+}(s) = \frac{G_{\alpha\alpha}(s) + G_{\beta\beta}(s)}{2} + j\frac{G_{\beta\alpha}(s) - G_{\alpha\beta}(s)}{2} & (4.19) \\ G_{\alpha\beta-}(s) = \frac{G_{\alpha\alpha}(s) - G_{\beta\beta}(s)}{2} + j\frac{G_{\beta\alpha}(s) + G_{\alpha\beta}(s)}{2} & (4.20) \end{cases}$$

The inputs $\underline{u}_{\alpha\beta\pm}$ and outputs $\underline{y}_{\alpha\beta\pm}$ are now complex vectors in the form $u_{\alpha\beta+} = u_{\alpha} + ju_{\beta}$ and $u_{\alpha\beta-} = u_{\alpha} - ju_{\beta}$, being, respectively, the forward component and is the backward component. Note that the forward and backward components are not the positive and negative sequences. These sequences are represented when we analyze the frequency $\pm\omega$ into $u_{\alpha\beta+}(+j\omega)$ and $u_{\alpha\beta+}(-j\omega)$, which represent the positive and negative sequences, respectively. The matrix $G_{\alpha\beta\pm}^m(s)$ is composed of two independent elements $G_{\alpha\beta+}(s)$ and $G_{\alpha\beta-}(s)$, with $\overline{G}_{\alpha\beta+}(s)$ and $\overline{G}_{\alpha\beta-}(s)$ being its conjugate complexes.

The complex vector modeling above is still MIMO. In order to study the complex vector system as SISO, the symmetry assumption must be taken into consideration. If this condition is true, the elements of the main diagonal of the Transfer Matrix are equal and those of the secondary diagonal are negative of each other, which means:

$$\begin{cases} G_{\alpha\alpha}(s) = G_{\beta\beta}(s) = G_{\alpha}(s) & (4.21) \\ G_{\beta\alpha}(s) = -G_{\alpha\beta}(s) = G_{\beta}(s) & (4.22) \end{cases}$$

By applying this consideration in (4.19) and (4.20), we can simplify the Complex Vector model to:

$$\begin{cases} G_{\alpha\beta+}(s) = G_{\alpha}(s) + jG_{\beta}(s) & (4.23) \\ G_{\alpha\beta-}(s) = 0 & (4.24) \end{cases}$$

Thus,

$$\begin{cases} \underline{y}_{\alpha\beta+} = G_{\alpha\beta+}(s)\underline{u}_{\alpha\beta+} & (4.25) \\ \underline{y}_{\alpha\beta-} = \overline{G}_{\alpha\beta+}(s)\underline{u}_{\alpha\beta-} & (4.26) \end{cases}$$

The Complex Vector modeling described above is SISO, which makes it easier to analyze the impedance of the system. The symmetry argument is valid for the desired application in this work because the eigentransfer functions that model the control and the plant are the same for the axes $\alpha\beta$. This also configures that the modeled system is balanced and time invariant [141]. Besides that, the coupling between currents also respects the rule established in (4.22), since this coupling is performed from $\pm\omega L_v$, according to Figure 4.1.

This modeling can be applied to the analysis of the total output impedance of the $Z_{out}(s)$ converter. According to [60], the impedance can be modeled by a complex vector in a generic way as:

$$Z^m(s) = \begin{bmatrix} Z_+^m(s) & Z_-^m(s) \\ \overline{Z}_-^m(s) & \overline{Z}_+^m(s) \end{bmatrix} \quad (4.27)$$

Being:

$$\begin{cases} Z_+^m = Z_{out}(s) = Z_{cl}(s) + Z_{ext}(s) + L_2s + R_2 & (4.28) \\ Z_-^m = 0 & (4.29) \end{cases}$$

making it so that there is only a need to analyze Z_+^m , due to the impedance symmetry of the system. The tracking transfer function $G_{cl}(s)$ does not need to be analyzed in this way because the Outer VI does not affect the system's tracking transfer function, as mentioned in Section 2.2. However, due to the presence of cross-coupling because of $j\omega L_v$ and complex modeling, there is no symmetry for system response for positive and negative frequencies, since now the transfer functions do not have only real coefficients, but also complex ones, and that can generate asymmetric poles and zeros [60, 141, 142]. Therefore, Bode analysis must be performed for positive and negative frequencies. This technique is used heavily in [60].

4.3 Outer Virtual Impedance Design

Once the methodology is described in Section 4.2, the application for the case and the converter studied can be performed. Table 4.1 displays the input values for the power flow analysis. The units are in pu, according to the bases defined in Section 2.4.

Table 4.1: Input values for Outer VI design.

Input Parameters	
Maximum V_{conv} (pu)	1.07
Maximum θ ($^\circ$)	10
P_{demand} (pu)	1
Q_{demand} (pu)	1
Desired X_L/R	100
X_2 (pu)	0.0397
R_2 (pu)	0.0011
X_g (pu)	0.05
R_g (pu)	0.0025

From the input values, it is possible to calculate the maximum active and reactive powers – from equations (4.5) and (4.6) – that the converter is capable of injecting without the presence of $R_v + jX_v$. Under these conditions, the maximum active and reactive powers of the converter are:

$$P_{max} = 2.163\text{pu} \quad (4.30)$$

$$Q_{max} = 0.4368\text{pu} \quad (4.31)$$

As seen in the simulation results in Section 3.4, the converter does not have the capability to inject 1.0 pu of reactive power, and this fact is confirmed from the maximum active and reactive power calculations. As shown in Table 4.1, the desired active and reactive power demands are $P_{demand} = Q_{demand} = 1.0$. This value is desired so that the converter has the full ability to change its operating point given the needs of the grid to which it is connected. From this first constraint, some values can be taken for the impedance $R_v + jX_v$.

Since it is desired to reduce the value of the line impedance by $R_v + jX_v$, two vectors are constructed: R_{range} and X_{range} . They have total length of 20 values. Each of these vectors ranges from 0 to the total line value, R_{line} and X_{line} :

$$\begin{cases} R_{range} = [0, \dots, R_{line}] \rightarrow R_{line} = R_2 + R_g & (4.32) \\ X_{range} = [0, \dots, X_{line}] \rightarrow X_{line} = X_{L2} + X_g & (4.33) \end{cases}$$

With these vectors created, a mesh of 400 possible impedance values is also created. In it, each combination of R_{range} and X_{range} elements is represented. For each mesh combination, the maximum active and reactive power are calculated and compared to the desired values of P_{demand} and Q_{demand} . Combinations that have total power greater than the demanded ones are saved. Figures 4.2a and 4.2b display the regions Ω_P and Ω_Q where the combinations that meet the sole and exclusive constraint of P_{demand} and Q_{demand} , respectively. The red point in the impedance plane indicates the original line impedance without H_{ext} .

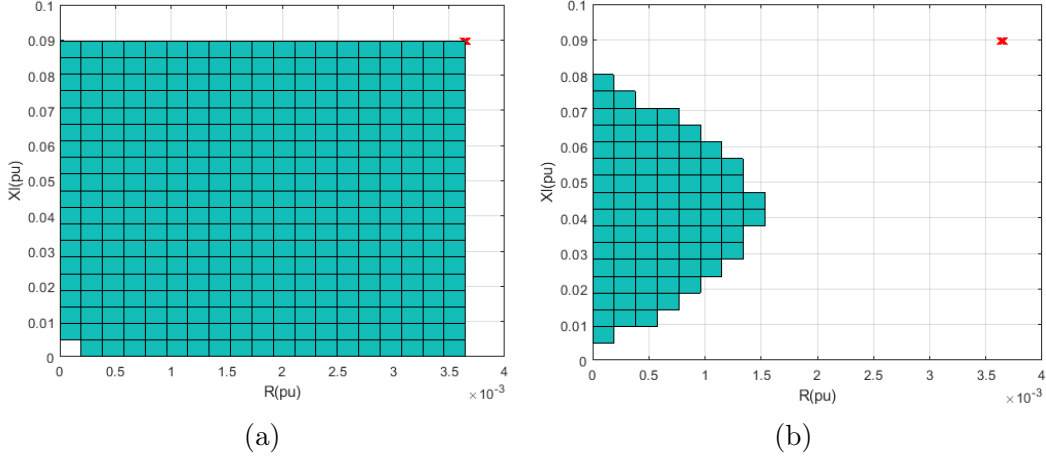


Figure 4.2: Area Ω_P where the maximum active power is bigger than P_{demand} (a), and area Ω_Q where the maximum reactive power is bigger than Q_{demand} (b).

As expected, the Ω_P area considers all points in its interior, since the highest possible line impedance, which is the one existing in the system, has maximum power greater than 1.0 pu. However, the Ω_Q area has a much larger restriction, where only the smallest impedance combination values allow such reactive injection greater than 1.0 pu.

The last constraint to be applied is related to the X_L/R ratio of the line. As seen in Table 4.1, the X_L/R ratio of the line is equal to 24.6043. In order for the system to be fully decoupled, a ratio equal to 100 is desired, a typical value for high voltage systems. Similarly, the combination of values that respect this constraint is then sought. Figure 4.3a displays the area Ω_{ratio} of values that this condition holds.

The Ω_{ratio} area illustrates the line impedance combinations that have $X_L/R \geq 100$. Notice that the accepted values are located in the region near the upper bound of X_{range} and lower bound of R_{range} . The Ω area of possible values is then obtained by making the intersection of the areas Ω_P , Ω_Q and Ω_{Ratio} , which are respectively the areas described by the above constraints. This area is illustrated in Figure 4.3b

$$\Omega = \Omega_P \cap \Omega_Q \cap \Omega_{Ratio} \quad (4.34)$$

The values contained in the Ω area are the total values of the line impedances that

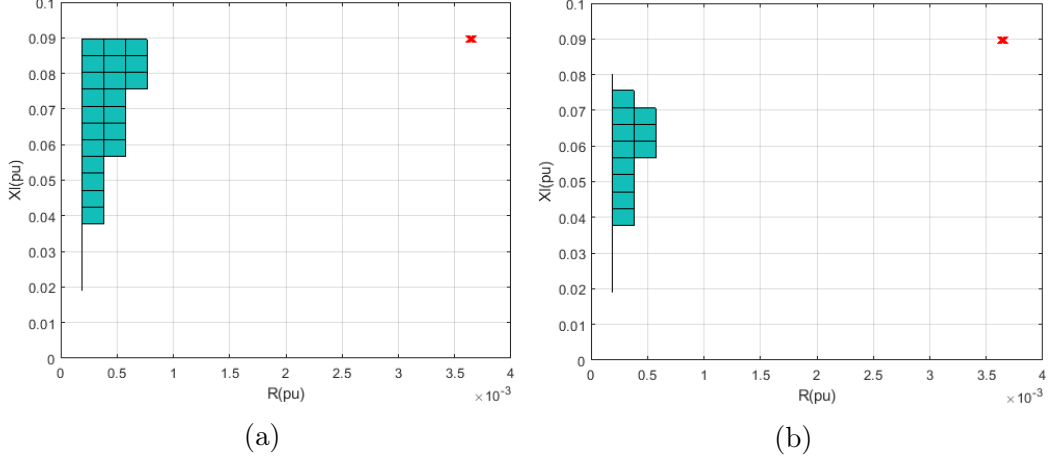


Figure 4.3: Area Ω_{ratio} where the line ratio is greater than 100 (a), and area Ω of possible values that satisfy the constraints.

respect the constraints. Notice that they are all smaller than the total impedance $R_{line} + jX_{line}$ without the Outer VI. To obtain the $R_v + jX_v$ values, each Ω element is subtracted from the total value $R_{line} + jX_{line}$. The result of this subtraction are the admissible $R_v + jX_v$ values. Of the 400 total combinations, only 27 values are valid. The 27 values are shown below.

$$\begin{aligned}
R_v + jX_v = \{ & \mathbf{-0.0035 - j0.0094}; -0.0033 - j0.0142; -0.0035 - j0.0142; \\
& -0.0031 - j0.0189; -0.0033 - j0.0189; -0.0035 - j0.0189; \\
& -0.0031 - j0.0236; -0.0033 - j0.0236; -0.0035 - j0.0236; \\
& -0.0031 - j0.0283; -0.0033 - j0.0283; -0.0035 - j0.0283; \\
& -0.0031 - j0.0331; -0.0033 - j0.0331; -0.0035 - j0.0331; \\
& -0.0033 - j0.0378; -0.0035 - j0.0378; -0.0033 - j0.0425; \\
& -0.0035 - j0.0425; -0.0033 - j0.0472; -0.0035 - j0.0472; \\
& -0.0033 - j0.0519; -0.0035 - j0.0519; -0.0035 - j0.0567; \\
& -0.0035 - j0.0614; -0.0035 - j0.0661; \mathbf{-0.0035 - j0.0708} \}
\end{aligned}$$

The above admissible values are sorted from the modulus $|Z_v| = \sqrt{R_v^2 + X_v^2}$ in an ascending order, i.e., the first value has the smallest $|Z_v|$, i.e., that will cause the smallest decrease in the final line impedance value. The bold impedance $-0.0035 - j0.0094$ pu and $-0.0035 - j0.0708$ pu are the minimum (H_{min}) and maximum (H_{max}) value respectively, and will be implemented in the simulation. The comparison and analysis of all the values and their Bode diagrams are shown in Appendix A.

Figures 4.4, 4.5 and 4.6 show the closed-loop $Z_{out}(s)$ poles and zeros for the PR-Analytical, PR-Gao, and VPI controllers, respectively. All the controllers have

similar behavior, as H_{ext} increases, the asymmetric poles move further and further apart, as shown in Figures 4.4b, 4.5b and 4.6b. In blue, orange and yellow are represented the values H_{min} , H_{med} , and H_{max} , respectively. As these poles move further and further apart, the greater the difference between the frequency response for positive and negative frequencies. Note that for the value H_{max} , in yellow, the asymmetric zero is a right-hand zero.

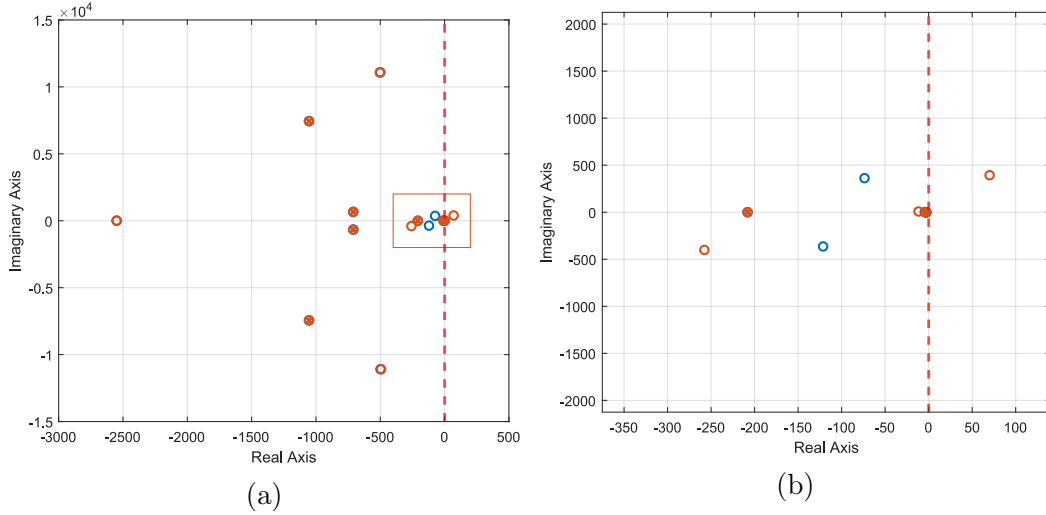


Figure 4.4: Closed-Loop poles and zeros from $Z_{cl}(s)$ for the PR-Analytical controller with H_{min} (blue), H_{max} (orange) (a). The zoom in the highlighted area is illustrated in (b)

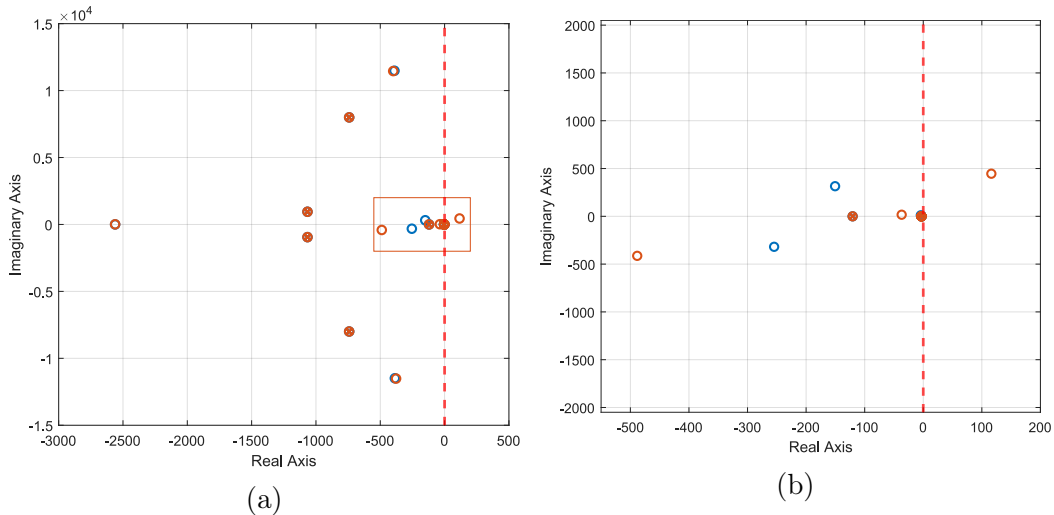


Figure 4.5: Closed-Loop poles and zeros from $Z_{cl}(s)$ for the PR-Gao controller with H_{min} (blue), H_{max} (orange) (a). The zoom in the highlighted area is illustrated in (b)

The comparison between the Bode diagrams of the PR-Analytical (blue), PR-Gao (orange), and VPI (yellow) controllers with the Outer VI H_{min} and H_{max} is done in Figures 4.7 and 4.8, respectively. Due to the existence of asymmetric zeros, an

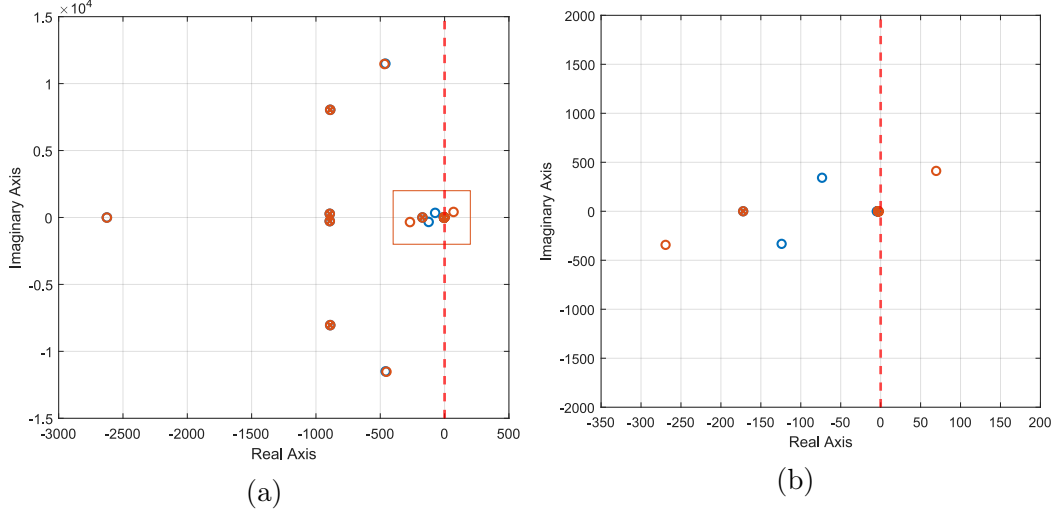


Figure 4.6: Closed-Loop poles and zeros from $Z_{cl}(s)$ for the VPI controller with H_{min} (blue), H_{max} (orange) (a). The zoom in the highlighted area is illustrated in (b)

analysis is required for both negative and positive frequencies, which are illustrated on the left and right of the figures, respectively.

For H_{min} , the VPI controller is the only one with resistive impedance at low frequencies, while the PR-Gao has mostly capacitive impedance due to its phase being close to -90° . This phenomenon is also carried for the larger value of H_{max} . The PR-Analytical controller, on the other hand, exhibits resistive and capacitive behavior as a consequence of its phase value of -45° , but at H_{max} Bode, its phase moves toward the -90° at low frequencies.

Near the fundamental frequency, where resonant controllers have minimum impedance, the presence of the inductance L_2 and the impedance H_{ext} becomes the main ones in power flow control, as seen previously. By analyzing the three Bodes with H_{min} and H_{max} , it can be seen that the converter has similar impedance at positive frequencies.

For the negative frequencies near the fundamental, this difference is not so evident and H_{min} has the lowest impedance for this frequency. Thus, the PR-Analytical, PR-Gao and VPI controllers with H_{min} have the lowest sensitivity for negative fundamental sequence.

At high frequencies, where the sL_2 impedance is dominant, all output impedances $Z_{out}(s)$ in all cases of H_{min} and H_{max} are inductive, and there is no modification due to the insertion of the Outer VI. This means that the sensitivity to harmonic and sideband oscillations are unchanged.

For both the positive and negative low frequencies, the PR-Gao controller has the highest impedance, and may then be more susceptible to unwanted DC components from the system. The VPI controller has the lowest impedance H_{max} , while the

PR-Analytical has the lowest for H_{min} .

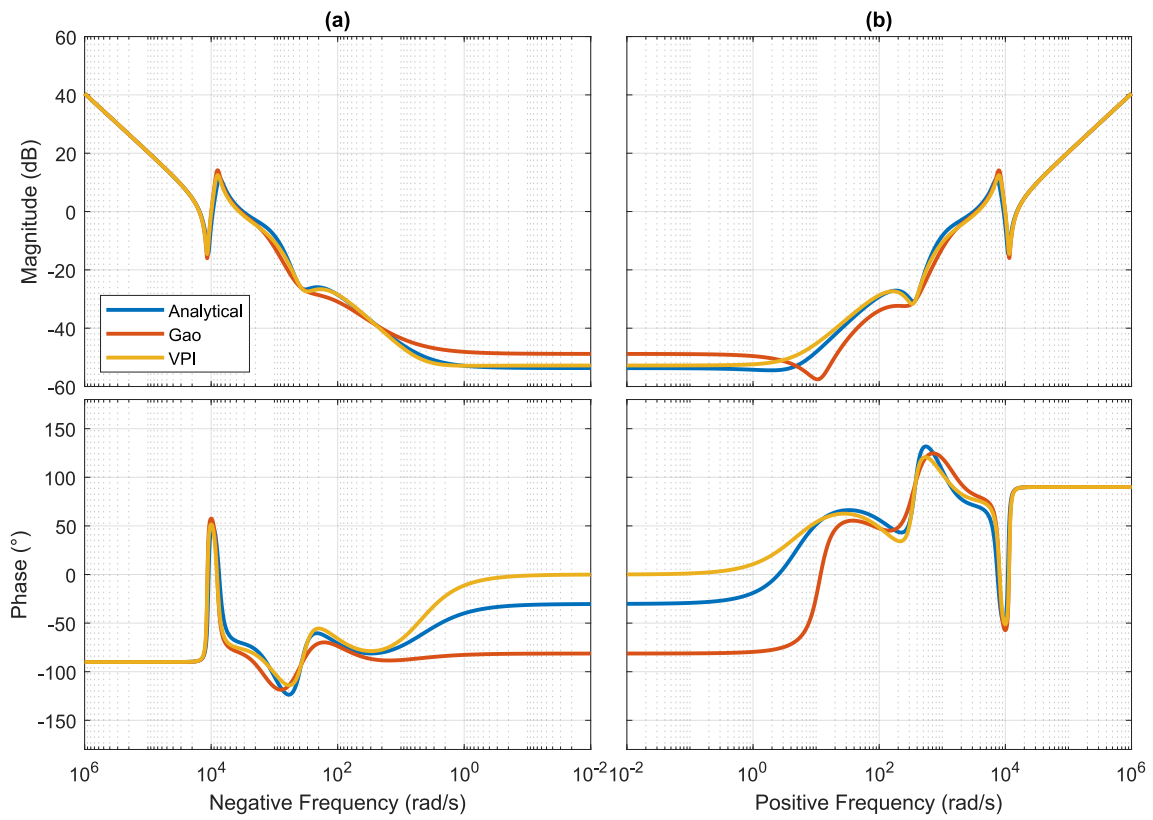


Figure 4.7: Bode diagram for negative (a) and positive (b) frequencies for $Z_{out}(s)$ with H_{min} .

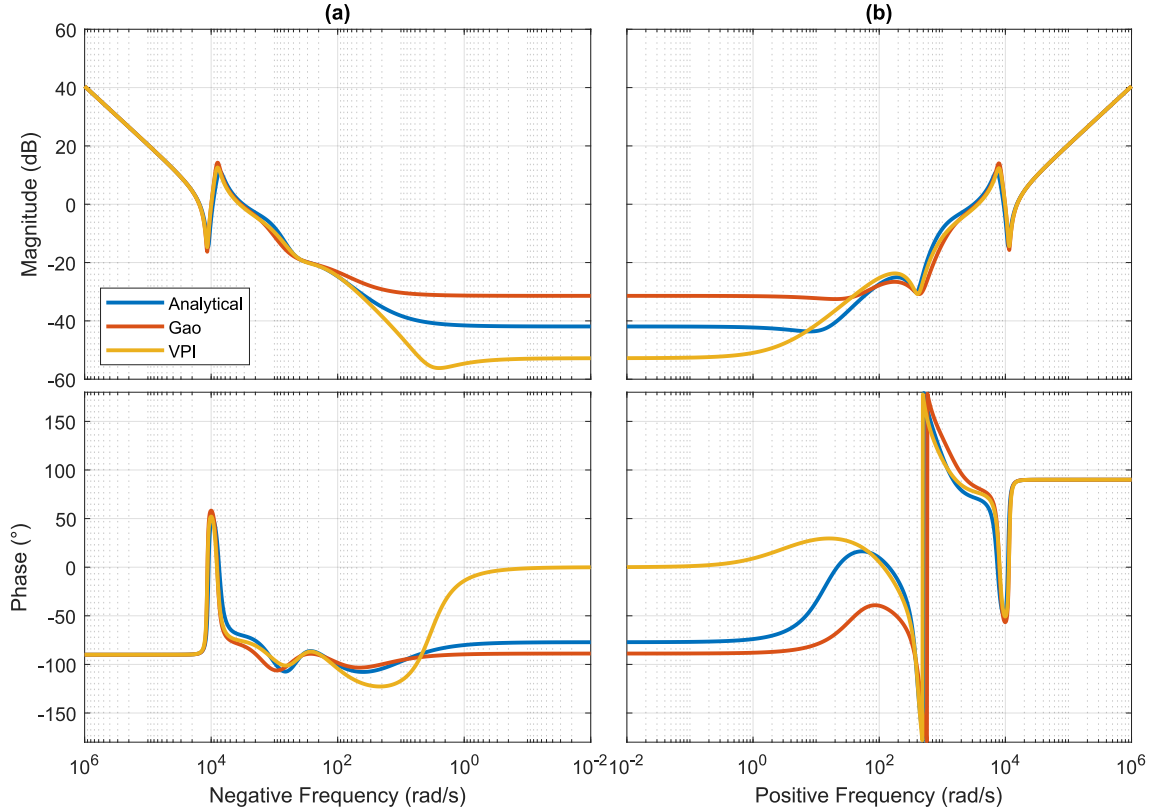


Figure 4.8: Bode diagram for negative (a) and positive (b) frequencies for $Z_{out}(s)$ with H_{min} .

4.4 Simulation Results

Simulation results with the H_{ext} implementation are presented here. As described in Section 2.2, the use of H_{ext} does not interfere with the tracking dynamics, so *Dynamic Test* will not be performed here. In addition, two new perturbations were added in *Disturbance Rejection Test*: operation with harmonic grid and with unbalanced grid. These disturbances were also done by changing the system's AC source. The purpose of inserting these tests is to check the impact of H_{ext} at different frequencies. The objective is to verify if the different impedance shapes due to the compared controllers will lead to distinct distortions in V_C , since there is no control structures to remove or mitigate the harmonic or unbalance disturbances.

4.4.1 Power Injection Test

The power injection test has the same objective as the one presented before, with only one more event added: at 0.85 s, the virtual impedance will be activated in the control, and the change in the power injection behavior will be verified.

Active Power Step

Here, the virtual impedance values H_{min} and H_{max} will be compared side by side. H_{min} is always at the left side, while H_{max} is always at the right side. Figures 4.9a and 4.9b show the insertion of H_{min} and H_{max} , respectively after the active power step $P_{set} = 1.0$ pu.

In Figure 4.9a the insertion of H_{min} does not cause much disturbance in the active power. However, in the reactive power, it can be seen that the average value of Q_{meas} goes from 0.0 to 0.05 pu. Furthermore, the PR-Gao controller has the highest transient oscillatory behavior, while the VPI controller has the lowest oscillation.

However, the insertion of H_{max} causes a large disturbance in the system powers, with the active powers P_{meas} exceeding 2.0 pu for the PR-Analytical and VPI controllers, and 3.0 pu for the PR-Gao controller, and the reactive powers Q_{meas} near -0.5 pu. These levels are unacceptable, and demonstrate that the need for the soft insertion of outer VI at higher values.

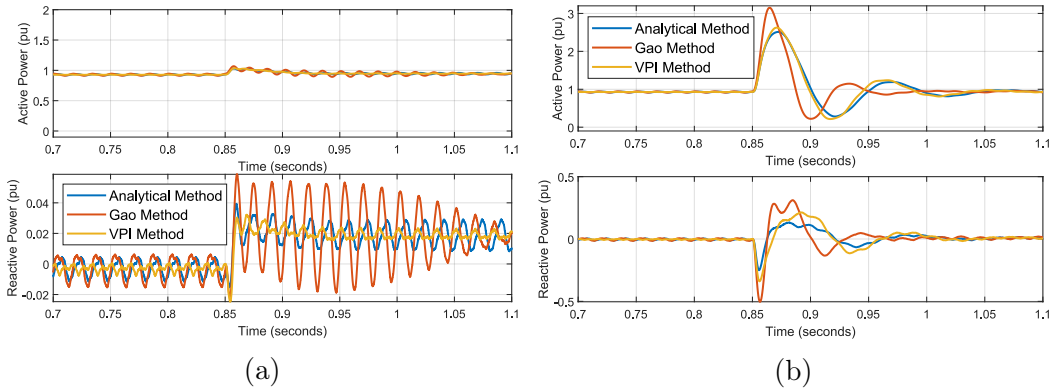


Figure 4.9: Active and reactive dynamics when $P_{set} = 1.0$ pu in steady-state and H_{min} (a) and H_{max} (b) are inserted.

Figures 4.10a and 4.10b present the dynamic response for $|V_C|$ after insertion of the outer VI. The small perturbations seen in the powers after insertion of H_{min} are also seen in $|V_C|$ for all controllers, in Figure 4.9a. However, when H_{max} is inserted, the large perturbations seen in both P_{meas} and Q_{meas} translate into only transients with a maximum amplitude of 2%. Again, the PR-Gao controller has the largest oscillations.

Since the purpose of the outer VI insertion is to reduce the line impedance and help in the reactive injection of the total converter, the modulation rates m_{abc} must be monitored, since a higher reactive injection may require a voltage increase that may lead the converter to over-modulation. Figures 4.11a, 4.11b and 4.11c display the three-phase modulation ratios sent to the PWM of the PR-Analytical, PR-Gao and VPI converters using H_{min} , respectively, while Figures 4.12a, 4.12b and 4.12c

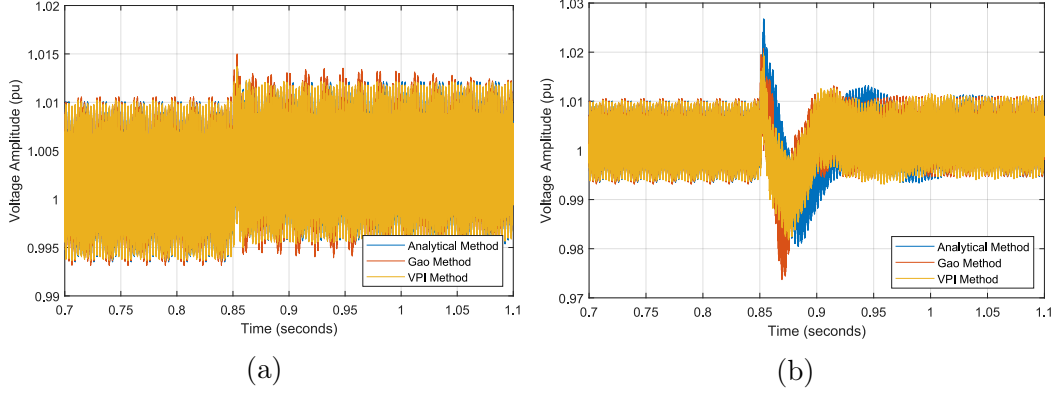


Figure 4.10: $|V_C|$ dynamics when $P_{set} = 1.0$ pu in steady-state and H_{min} (a) and H_{max} (b) are inserted.

for these same controllers using H_{max} . For all controllers and H_{min} and H_{ext} values, the converter is far from violating the 1.0 pu limit and entering the over-modulation region.

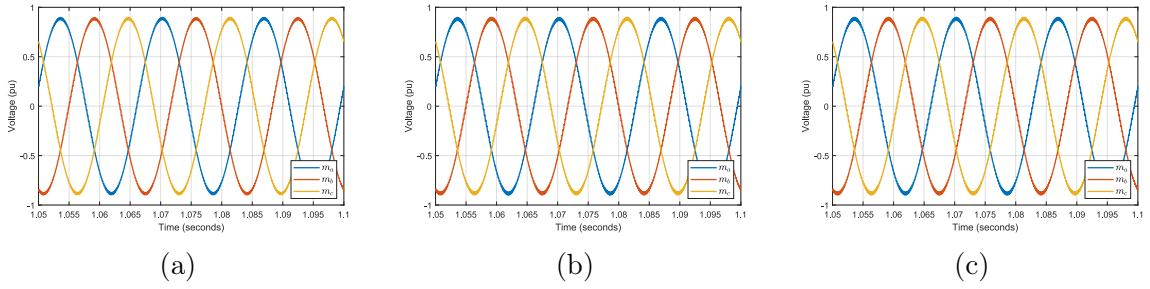


Figure 4.11: Three-phase modulation index m_{abc} with $P_{set} = 1.0$ pu after the insertion of H_{min} for the PR-Analytical (a), PR-Gao (b) and VPI (c) controllers.

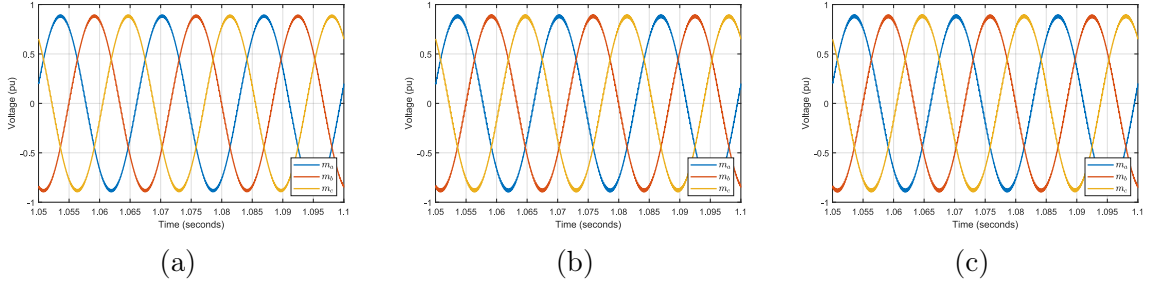


Figure 4.12: Three-phase modulation index m_{abc} with $P_{set} = 1.0$ pu after the insertion of H_{max} for the PR-Analytical (a), PR-Gao (b) and VPI (c) controllers.

Reactive Power Step

The same procedure performed for active power will be performed for reactive power. After the step of $Q_{set} = 1.0$ pu, the virtual impedance will be connected at 0.85 s. In this scenario, a greater impact is expected from the implementation of H_{ext} , whose main objective is to enhance reactive power injection. The dynamics

of the active and reactive powers for the outer VI H_{min} and H_{max} are laid out in Figures 4.13a and 4.13b, respectively.

Looking at Figure 4.13a, it can be seen that the insertion of H_{min} is not enough to have a significant improvement in reactive injection, where the average value changes from 0.45 pu to 0.48 pu. Therefore, this value did not meet the established design. However, the H_{max} value presents a higher injection of reactive power, changing from 0.45 pu to 0.8 pu, as illustrated in Figure 4.13b. It is observed, however, that in the steady-state the active power has a different behavior than before the insertion of H_{max} .

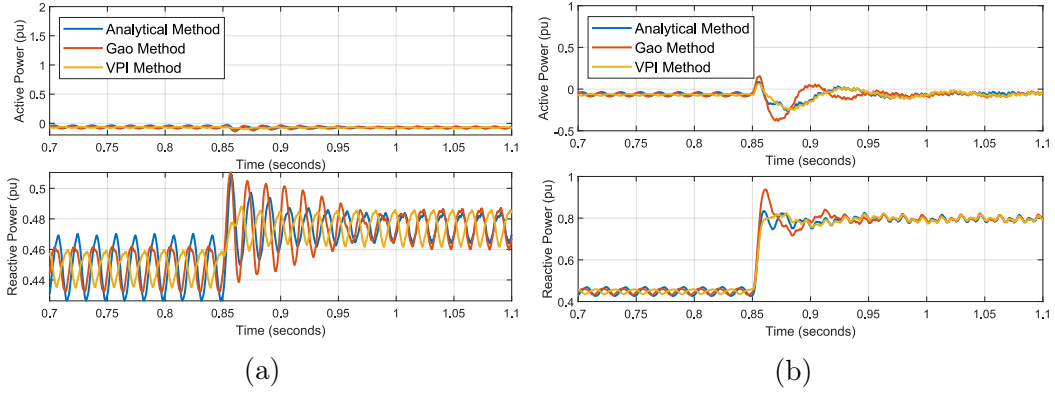


Figure 4.13: Active and reactive dynamics when $Q_{set} = 1.0$ pu in steady-state and H_{min} (a) and H_{max} (b) are inserted.

Analysis of the $|V_C|$ voltage profiles gives more information about the effects of H_{min} and H_{max} , respectively in Figures 4.14a and 4.14b. Due to the small modification in operating point caused by H_{min} , changes are also not observed in its stress profile $|V_C|$. However, when H_{max} is present, in addition to an increase in the amplitude value $|V_C|$ it is also noticeable that there is a change in behavior at high frequencies, having higher amplitude. This can identify a possible overmodulation.

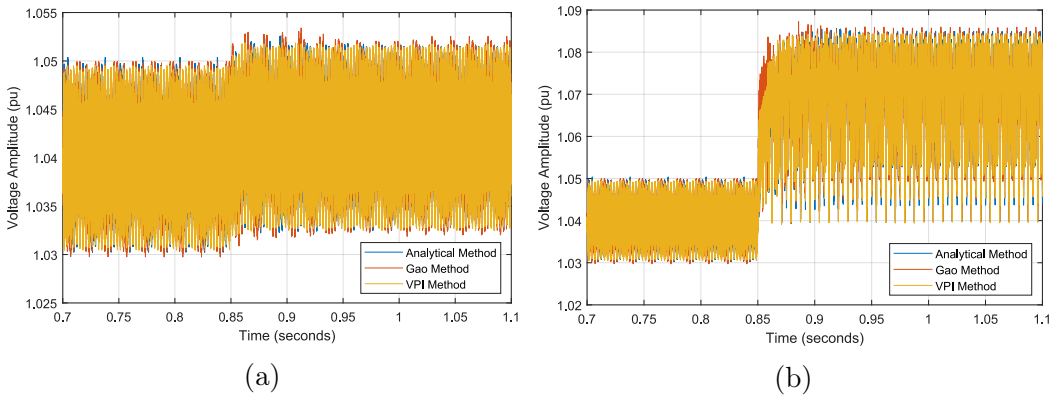


Figure 4.14: $|V_C|$ dynamics when $Q_{set} = 1.0$ pu in steady-state and H_{min} (a) and H_{max} (b) are inserted.

The modulation indexes m_{abc} for the PR-Analytical, PR-Gao and VPI controllers

with H_{min} are arranged in Figures 4.15a, 4.15b and 4.15c, as well as for these same controllers with H_{max} are illustrated in Figures 4.16a, 4.16b and 4.16c.

For the three controllers operating with H_{min} , it can be seen that the modulation rate is already close to the 1.0 pu amplitude limit. However, with the gain H_{max} , the converter over-modulates and the limiter of the controls acts. With this, it is possible to see the deformation of the reference sinusoidal signals for the PWM. This explains the change in the patterns observed in the steady-state in Q_{meas} and $|V_C|$. Furthermore, it shows that the converter reactive problem is a combination of the line impedance and the small excursion of the DC link voltage. The injection of third harmonic is a possible control solution, as it reduces the reference amplitude, thus, removing it from the over-modulation region.

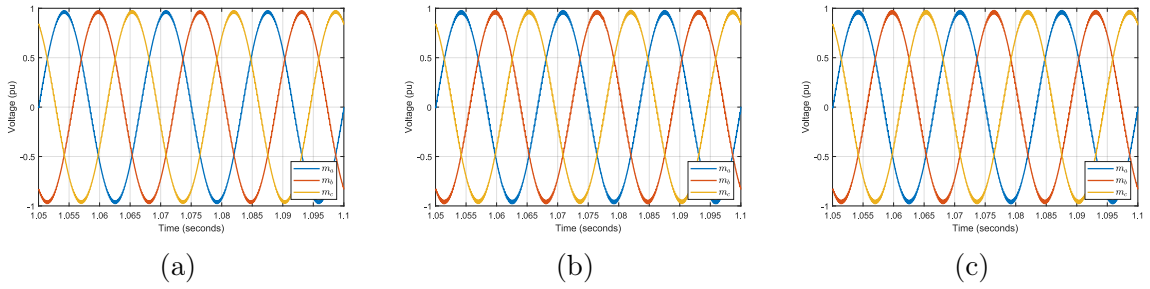


Figure 4.15: Three-phase modulation index m_{abc} with $Q_{set} = 1.0$ pu after the insertion of H_{min} for the PR-Analytical (a), PR-Gao (b) and VPI (c) controllers.

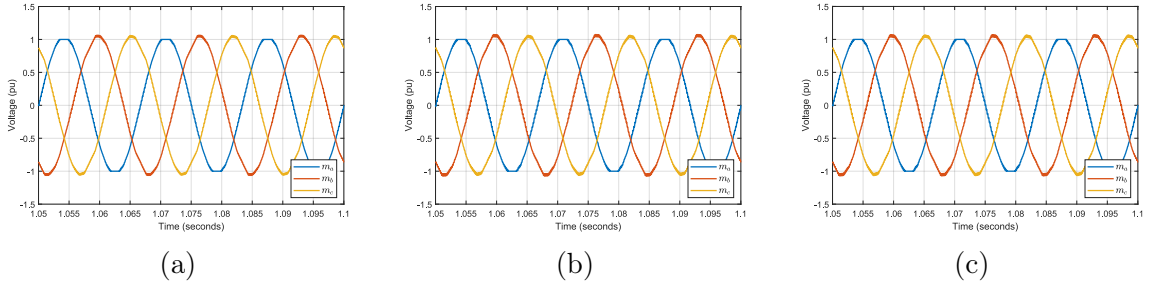


Figure 4.16: Three-phase modulation index m_{abc} with $Q_{set} = 1.0$ pu after the insertion of H_{max} for the PR-Analytical (a), PR-Gao (b) and VPI (c) controllers.

In Figures 4.16a, 4.16b and 4.16c, the resulting voltage signals are limited by a simple PSCAD limiter block, but in the $\alpha\beta$ reference frame. This results in only phase a , in blue, being cut, and phases b and c — orange and yellow, respectively — having a different signal.

4.4.2 Disturbance Rejection Tests

Disturbance Tests are performed with $P_{set} = 1.0$ pu and with the outer VI H_{min} and H_{max} already operating in the converter. From this, the disturbances are inserted into the simulation at 1.35 s.

Voltage Sag

The 7% V_{grid} voltage sag is applied at 1.35 s, and the $|V_C|$ and I_2 phase a current profiles of with the H_{min} and H_{max} gains are illustrated in Figures 4.17a and 4.17b, respectively.

The first discrepancy between H_{min} and H_{max} is that for the lower gain the converter is not able to hold at $|V_C = 1.0|$ pu, while for the higher gain the converter returns to its original operating point. Furthermore, the PR-Gao controller operating at H_{min} has slow dynamics to return to the steady-state. Note that for both the H_{min} and H_{max} gains there is a current peak right after the sink. This peak is due to the response of the power control, which injects reactive to maintain the voltage level of the converter.

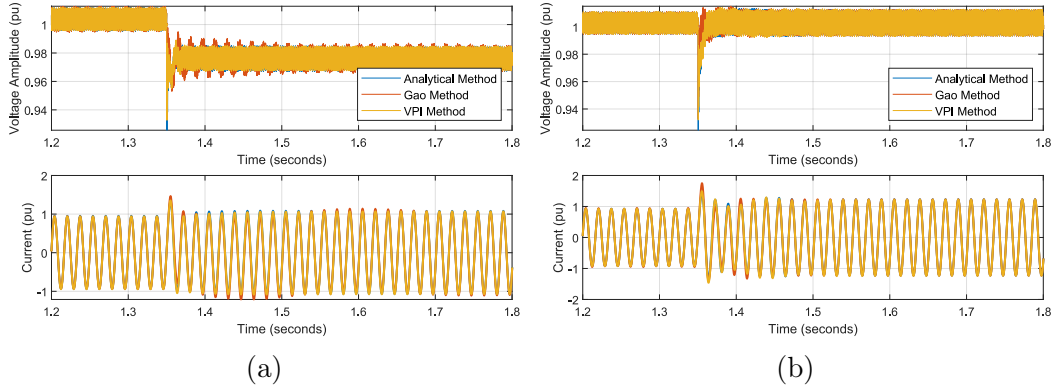


Figure 4.17: $|V_C|$ and I_2 phase a current dynamics when a 7% voltage sag is applied with H_{min} (a) and H_{max} (b).

As stated above, the current peak is due to power dynamics. For the gain H_{min} , in Figure 4.18a, in both active and reactive power the PR-Gao controller has oscillations, which justifies the oscillatory profile in $|V_C|$. Furthermore, the converter can only supply a little more than 0.4 pu of reactive, which justifies its voltage $|V_C|$ being below 1.0 pu in the steady-state.

However, the gain H_{max} is able to maintain its voltage $|V_C| = 1.0$ pu because its ability to inject reactive is greater. Note that the power $Q_{meas} = 0.8$ pu in the steady-state. Unlike the Reactive Test, there is no evidence of overmodulation because as the grid voltage has decreased, the control effort to inject such reactive is not large enough to destabilize the converter. However, again, the PR-Gao controller operating at H_{max} has power transients that can damage the equipment, since instantaneous $P_{meas} = 1.5$ pu and $Q_{meas} = 1.0$ pu. The PR-Analytical and VPI controllers despite having the same transients, are smoother and have lower amplitude when compared to the PR-Gao controller.

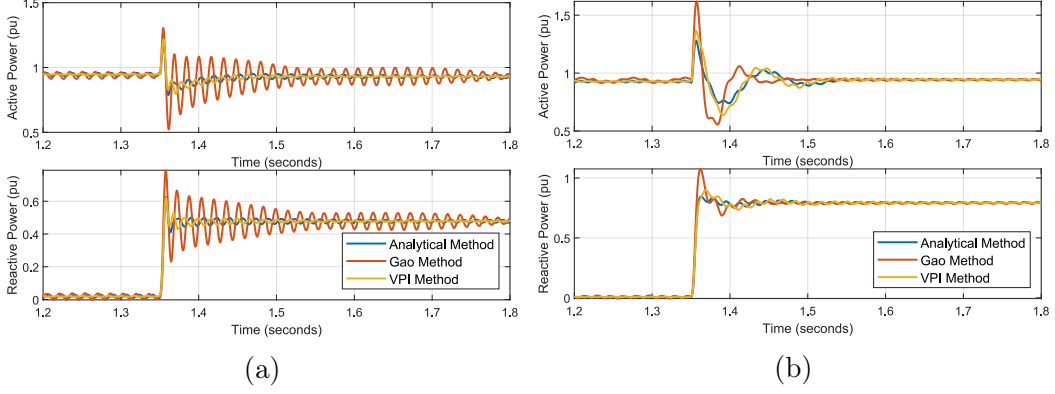


Figure 4.18: P_{meas} and Q_{meas} dynamics when a 7% voltage sag is applied with H_{min} (a) and H_{max} (b).

Frequency Step

The frequency step of 0.3 Hz is applied at 1.35 s. Figures 4.19a and 4.19b show the frequency calculated by the droop controller and the power injected by the converter with H_{min} and H_{max} , respectively.

The presence of outer VI H_{min} does not change the power and frequency dynamics of the converter, when compared to the cases presented in Section 3.4. However, the presence of H_{max} changes the dynamics from a damped system to a poorly damped response. In this case, the PR-Analytical and VPI controllers have the largest oscillation amplitudes and the longest settling time.

It is also important to mention that after the frequency step, the power of the controllers using H_{max} varies from 1.0 pu to -0.5 pu in a period of 50 ms. Such a power variation can cause instabilities in weaker networks, where the use of GFM converters is recommended.

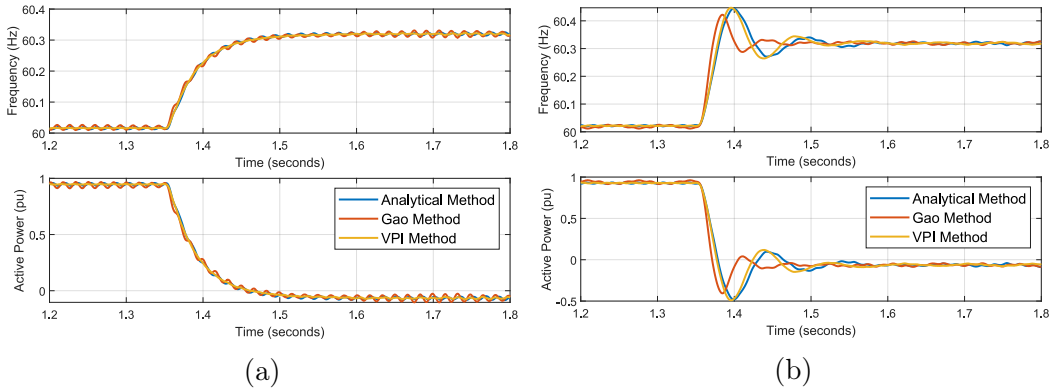


Figure 4.19: Frequency and P_{meas} after the 0.3 Hz frequency step with H_{min} (a) and H_{max} (b).

Figures 4.20a and 4.20b display the dynamics of $|V_C|$ and the current I_2 of phase a with H_{min} and H_{max} . Due to the power dynamics shown in Figure 4.19b, the

transient of the voltage $|V_C|$ using H_{max} is not as smooth compared to the gain H_{min} . This same dynamics presents itself in the current I_2 with H_{max} .

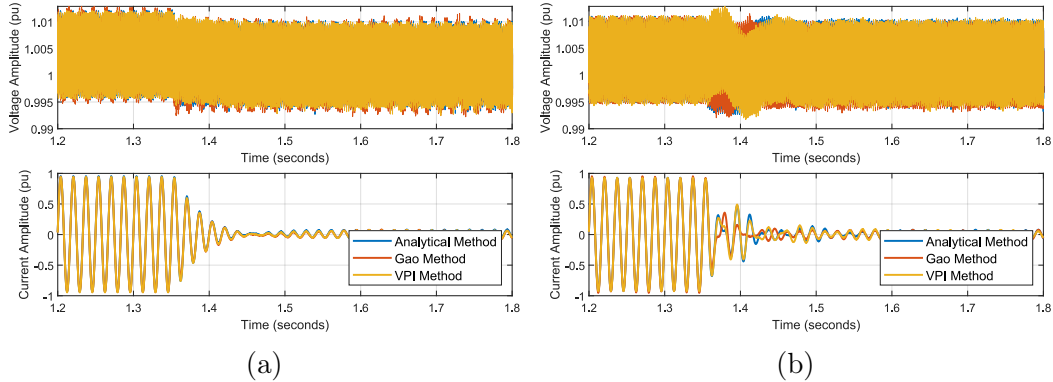


Figure 4.20: $|V_C|$ and I_2 phase a current dynamics the 0.3 Hz frequency step with H_{min} (a) and H_{max} (b).

Harmonic Grid

Here, the grid is modeled with the fundamental component and 10% of fifth and seventh harmonic voltage components. The disturbance is introduced at 1.35 s. The fifth and seventh harmonics were chosen because they are the closest to the fundamental frequency, and as explained earlier, at high frequencies the presence of the outer VI can be discarded. Figure 4.21 displays the waveform of the grid voltage before and after the harmonic distortion.

Figures 4.22a, 4.22b, and 4.22c display the three-phase voltage waveforms V_C , before and after the insertion of harmonics, for the PR-Analytical, PR-Gao and VPI controllers with H_{min} , respectively. Figures 4.23a, 4.23b, and 4.23c show the same voltages for the same controllers, but with H_{max} .

There are no major differences between the voltage forms for the three controllers, whether using H_{min} or H_{max} . This means that these harmonics are in the frequency region where the inductance L_2 is the largest impedance.

The powers P_{meas} injected by the converter with H_{min} and H_{max} after 1.35 s are shown in Figures 4.24a and 4.24b, respectively. With H_{min} , the first oscillation for all three controllers is fast, with the PR-Analytical and VPI controllers quickly returning to the steady-state. However, not only is the PR-Gao controller the slowest and most poorly damped, it also has the largest oscillation amplitude. A similar phenomenon occurs for the system with H_{max} , but the oscillations are now slower and the three controllers take longer to reach the steady-state. Again, PR-Gao has the worst dynamic performance.

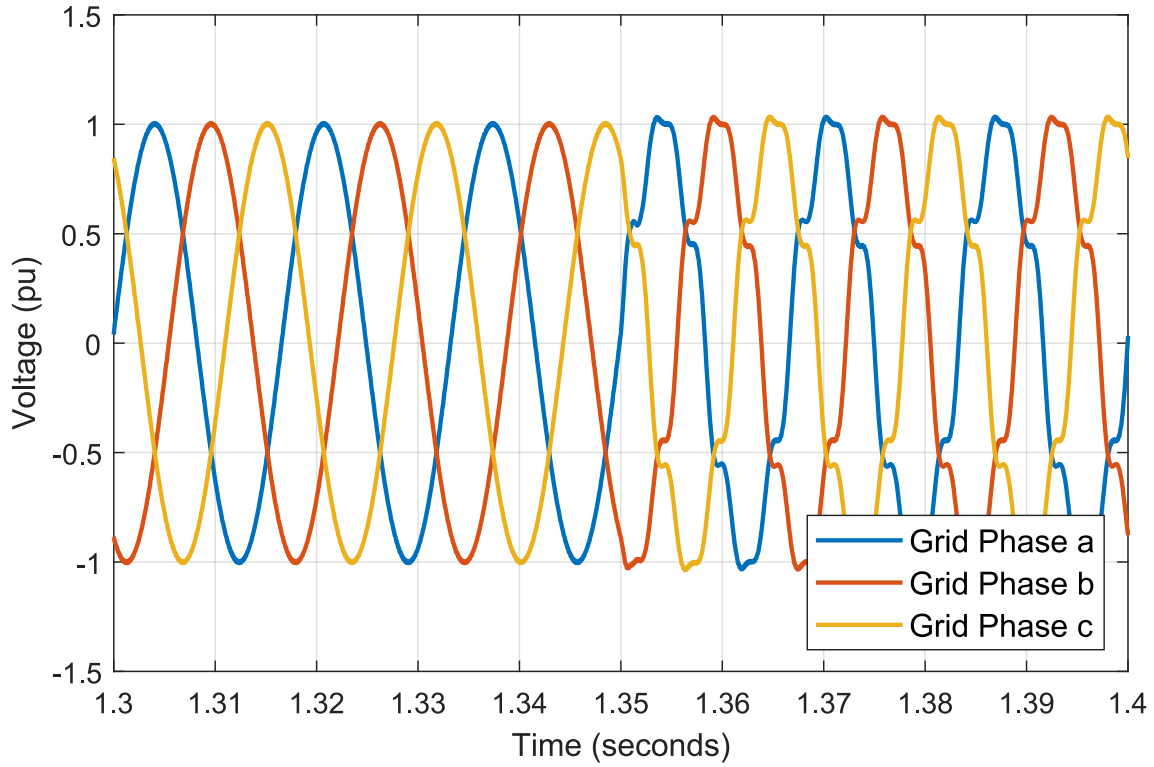


Figure 4.21: Grid voltage before and after the introduction of the harmonic distortion at 1.35 s.

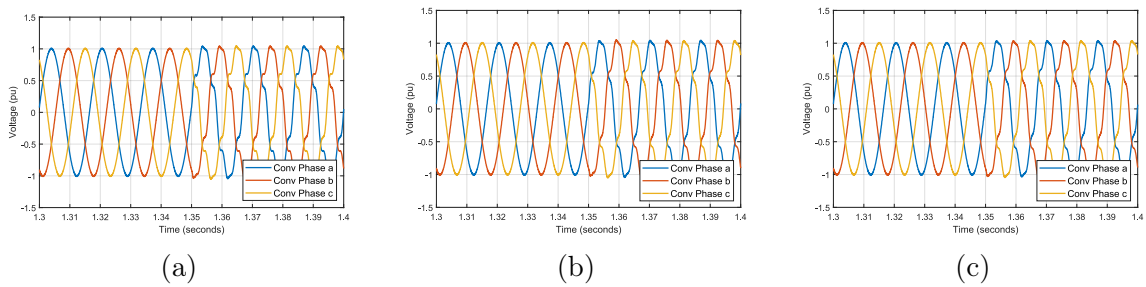


Figure 4.22: Three-phase converter voltages V_C before and after the fifth and seventh harmonic distortion addition for the PR-Analytical (a), PR-Gao (b) and VPI (c) controllers with H_{min} .

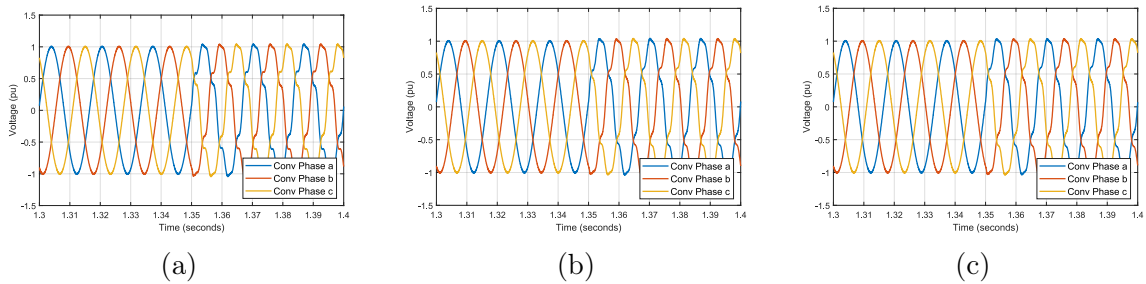


Figure 4.23: Three-phase converter voltages V_C before and after the fifth and seventh harmonic distortion addition for the PR-Analytical (a), PR-Gao (b) and VPI (c) controllers with H_{max} .

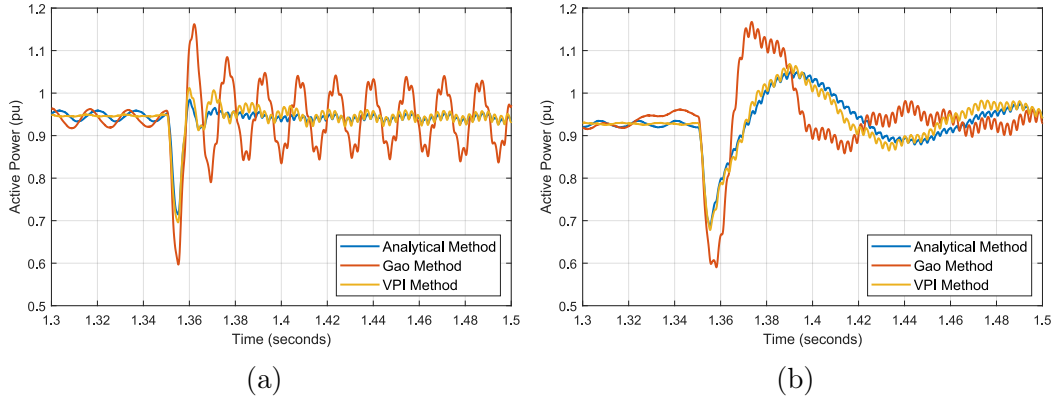


Figure 4.24: Injected active power after the voltage harmonics insertion for H_{min} (a) and H_{max} (b).

Unbalanced Grid

The objective of this test is to verify the dynamics of negative sequencing in converter control, since the use of H_{ext} makes the responses for positive and negative sequences asymmetric. To simulate the test condition, a 0.02 pu negative sequence acb disturbance is added in the grid-voltage source at 1.35 s. Figure 4.25 depicts the unbalanced grid voltage.

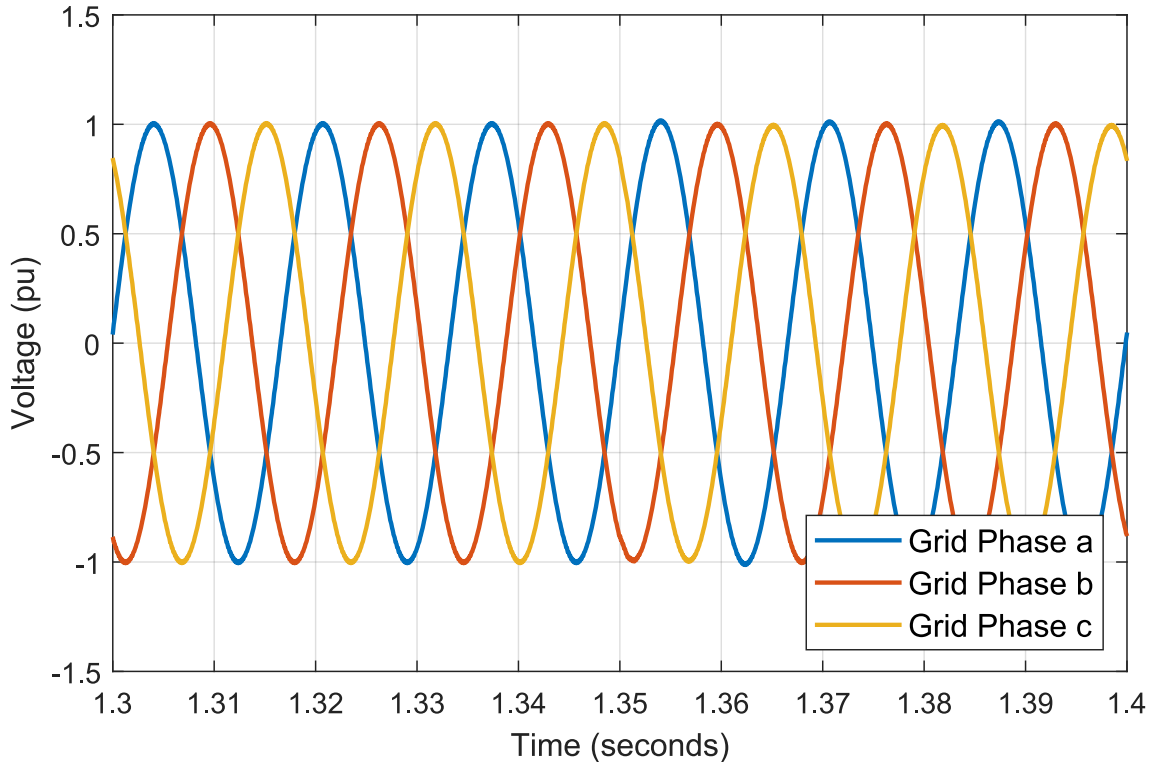


Figure 4.25: Grid voltage before and after the introduction of the harmonic distortion at 1.35 s.

As with harmonic operation, there are no notable differences between the three controllers using either H_{min} or H_{max} . Since there are no control structures to

remove the negative sequence, it remains at similar levels in all cases studied.

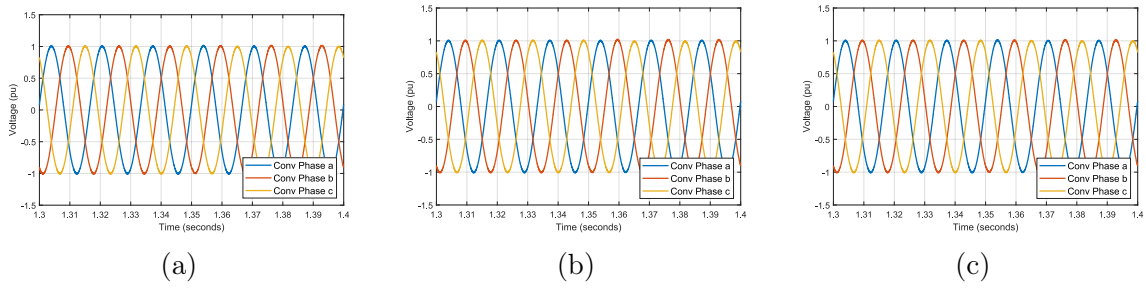


Figure 4.26: Three-phase converter voltages V_C before and after the fifth and seventh harmonic distortion addition for the PR-Analytical (a), PR-Gao (b) and VPI (c) controllers with H_{min} .

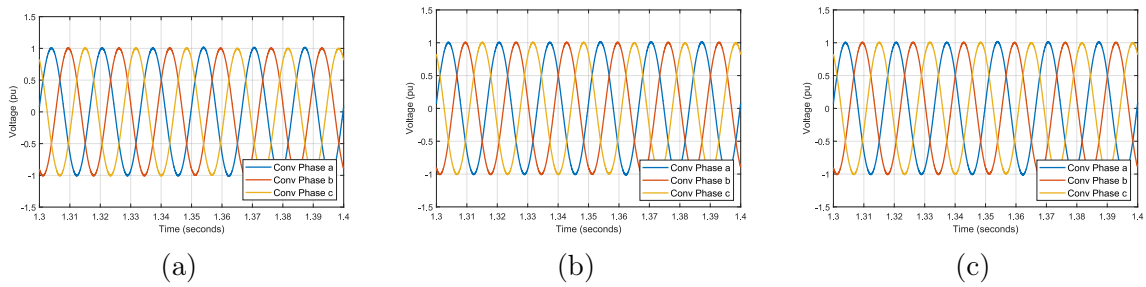


Figure 4.27: Three-phase converter voltages V_C before and after the negative sequence addition for the PR-Analytical (a), PR-Gao (b) and VPI (c) controllers with H_{max} .

In the P_{meas} power injected by the converter one notices greater differences with respect to the voltage profile. Figure 4.28a displays the power for the controllers compared to H_{min} . Again, the PR-Gao controller has the largest oscillations initially, however, all three controllers after the disturbance transient have oscillations that have a maximum of 1.2 pu to a minimum of 0.7. These oscillations are 120 Hz, a common oscillation frequency when voltage unbalances are present.

These oscillations are also present for controllers with H_{max} . However, these have the fastest transient, and the oscillation for all three controllers have a maximum of 1.05 pu to a minimum of 0.8.

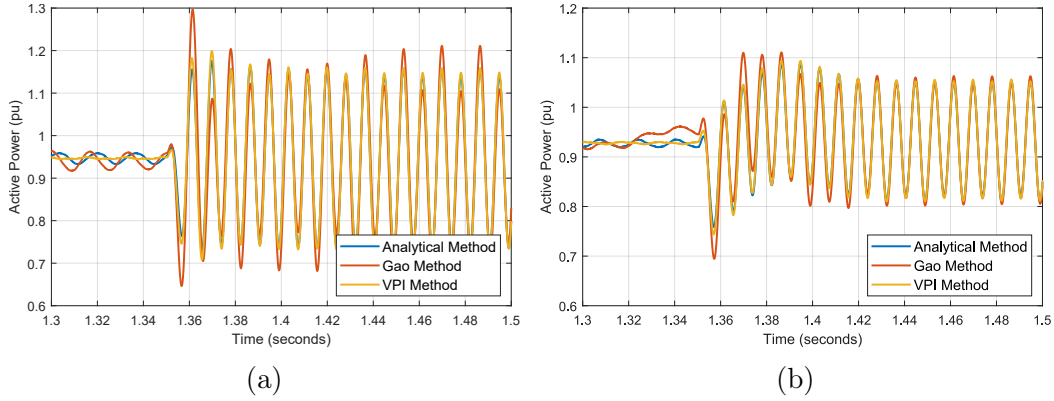


Figure 4.28: Injected active power after the voltage unbalance for H_{min} (a) and H_{max} (b).

4.5 Partial Remarks

The procedure based on the He and Li [121] method was presented, as well as the proposed modification for the resulting impedance analysis. In total, 27 values proved suitable to be implemented, but only the smallest and the largest of them were implemented in the simulation environment. The goal of the VI was to improve the reactive power injection of the converter.

The simulation showed that the minimum value H_{min} was not able to allow the desired reactive injection by the converter. The change was small when compared to the system without Outer VI. In addition, the PR-Gao controller showed a worsening in its transient behavior when using H_{min} . The PR-Analytical and VPI controllers showed changes in their dynamic behavior, but not drastic as PR-Gao.

The simulation with the maximum value H_{max} proved possible to improve the inverter reactive injection, but not in the desired totality. The maximum of 0.8 pu was reached, but as a drawback, the converter overmodulated due to the control effort. The dynamic performance of the controllers in the face of disturbances was also modified, and the PR-Gao controller has the worst dynamics. The PR-Analytical and VPI controllers had similar dynamics. The H_{max} value also provided a zero on the right-hand side, but its impact was not measured analytically or qualitatively. Further investigation of this phenomenon is needed.

Chapter 5

Conclusions

The present dissertation proposed the application of GCC to GFM converters that have LCL filters at their terminals, intending to expand the original work proposed by He and Li [24]. The mathematical model of the GCC-GFM-LCL application was presented, as well as the goals to be achieved in the sizing of its controllers and VI.

The inner VI design was primarily aimed at damping the intrinsic resonance of the LCL filter, in addition to the LC filter that is seen by the resonant controller. Both resonances were properly damped. As a consequence, the use of the inner VI also made it possible to better size the PR-Analytical, PR-Gao and VPI voltage single-loop controllers. The PR-Gao and VPI controllers need a first-order system for the cancellation of poles with zeros to be realized. The use of inner VI allowed the plant to be approximated by a first-order system and the design methods to be applied. The simulation results indicate that the damping technique is valid, and that the PR-Analytical and VPI controllers have the best dynamics in the simulated system.

However, two problems were pointed out during the simulation test. The first is that none of the controllers have the designed response time. This is a problem already presented in the literature, but barely explored and with few analyzed solutions. The second problem is the inverter's lack of reactive injection capacity. A hypothesis was raised: the high line-impedance that connects the converter to the grid for the desired reactive injection. The line-impedance hypothesis can be solved by using outer VI.

The outer VI design was based on improving the power flow of the converter, especially for reactive power. In addition, it was proposed to use the X_L/R ratio of the line as a constraint as well. From these constraints, the calculation of the outer VI was performed. The total of 27 values were calculated, however only two of them were chosen to be simulated. The impact of these gains on the output impedance of the converter was also performed, coming to the conclusion that when

using negative VI gains, the converter is more sensitive to disturbances.

The simulation results indicates that only the highest chosen value was able to significantly improve the converter's reactive injection, at the cost of the converter entering the over-modulation region. This indicates that the line impedance assumption is true. In addition, the power flow based calculation design did not prove true in the environment.

Improvements in this design are needed, such as including a constraint associated with the value of the DC link. Impedance analysis proved useful, however, only qualitative comparisons make it difficult to choose exactly which impedance to use. An analytical criterion is needed. Recently, the Nyquist stability criterion has been applied to the area of study known as impedance stability. However, this criterion has not been well defined and systematized yet for systems that have asymmetry in positive and negative frequencies.

This dissertation concludes its objectives by expanding the original GCC idea to GFM converters with LCL filters. As future work, improvements in the design and analysis methodologies of the outer VI are needed, as well as further studies in the implementation of the inner VI. However, the GCC controller and the use of VI are shown to be extremely flexible and applicable for different types of power electronics applications.

5.1 Future Works

In future work, experimental bench implementation is vital for the validation of the proposed control scheme. The experimental tests involve the development of the controller on embedded microcontrollers, and the need to discretize the resonant controllers and VI. This process involves the study of discretization techniques to maintain the correct controller operation, as well as the impacts of computational delay on the virtual impedance that were disregarded in this work.

The improvement in the power flow study is also necessary, as there were inconsistencies with the simulation. Modification to more robust models that take into account the full dynamics of the converter, not just the fundamental frequency, is a possibility for improvement. In this way, the sizing of the outer VI would take into account all frequencies during its design process.

Impedance stability applications are also needed. This stability criterion relates the output impedance of the converter to the impedance of the system to which it is connected, and from the analysis by Nyquist diagrams, it is possible to verify the final stability of the system. From the Nyquist study, it is also possible to obtain stability metrics, such as gain and phase margins, in addition to the compact metric of the sensitivity function. It is then possible to relate the sizing of the outer VI to

these stability metrics in order to optimize its operation.

Other applications of outer VI can also be studied for the GCC-GFM-LCL scheme, such as adaptive current limiting, to work in conjunction with inner VI.

References

- [1] *California State Profile and Energy Estimates*. Energy Report Available at: <https://www.eia.gov/state/analysis.php?sid=CA>, U.S. Energy Information Administration, 2021. Accessed: 2021-10-01.
- [2] ADMINISTRATION, U. E. I. *Texas State Profile and Energy Estimates*. Energy Report Available at: <https://www.eia.gov/state/analysis.php?sid=TX>, U.S. Energy Information Administration, 2021. Accessed: 2021-10-01.
- [3] AGENCY, I. E. “German 2020 - Energy Policy Review”, *International Energy Agency Report*, 2020.
- [4] AGENCY, I. E. “Energy Policies of IEA Countries - Denmark 2017 Review”, *International Energy Agency Report*, 2017.
- [5] *China Analysis*. Energy Report Available at: <https://www.eia.gov/state/analysis.php?sid=CA>, U.S. Energy Information Administration, 2021. Accessed: 2021-10-06.
- [6] *China Energy Transition Status Report 2021*. Energy Report Available at: <https://www.eia.gov/state/analysis.php?sid=CA>, Deutschland-China Energiepartnerschaft, 2021. Accessed: 2022-05-19.
- [7] ZHANG, J., DANIELA, A., FANG, Y., et al. “Review on China’s renewable energy and future projections”, *International Journal of Smart Grid and Clean Energy*, v. 7, n. 3, pp. 218–224, 2018.
- [8] *Plano Decenal de Expansão de Energia 2030*. Ministério de Minas e Energia - Secretária de Planejamento e Desenvolvimento Energético Disponível em: < <https://www.epe.gov.br/pt/publicacoes-dados-abertos/publicacoes/Plano-Decenal-de-Expansao-de-Energia-2030>, Ministério de Minas e Energia, Empresa de Pesquisa Energética, Brasília, Brasil, 2020. Accessed: 2021-10-01.

- [9] BOSE, B. K. “Global energy scenario and impact of power electronics in 21st century”, *IEEE Transactions on Industrial Electronics*, v. 60, n. 7, pp. 2638–2651, 2012.
- [10] VRANA, T., TORRES-OLGUIN, R., LIU, B., et al. “The North Sea Super Grid - a technical perspective”. In: *9th IET International Conference on AC and DC Power Transmission (ACDC 2010)*, pp. 1–5, 2010. doi: 10.1049/cp.2010.0992.
- [11] KHAN, A., HOSSEINZADEHTAHER, M., SHADMAND, M. B., et al. “On the stability of the power electronics-dominated grid: A new energy paradigm”, *IEEE Industrial Electronics Magazine*, v. 14, n. 4, pp. 65–78, 2020.
- [12] DOKUS, M., MERTENS, A., SARSTEDT, M. “On the stability of converter-dominated power systems: Impedance-based analysis”. In: *2020 International Conference on Smart Grids and Energy Systems (SGES)*, pp. 105–110. IEEE, 2020.
- [13] FU, X., SUN, J., HUANG, M., et al. “Large-signal stability of grid-forming and grid-following controls in voltage source converter: A comparative study”, *IEEE Transactions on Power Electronics*, v. 36, n. 7, pp. 7832–7840, 2020.
- [14] PATTABIRAMAN, D., LASSETER, R., JAHNS, T. “Comparison of grid following and grid forming control for a high inverter penetration power system”. In: *2018 IEEE Power & Energy Society General Meeting (PESGM)*, pp. 1–5. IEEE, 2018.
- [15] ROSSO, R., ENGELKEN, S., LISERRE, M. “Robust stability investigation of the interactions among grid-forming and grid-following converters”, *IEEE Journal of Emerging and Selected Topics in Power Electronics*, v. 8, n. 2, pp. 991–1003, 2019.
- [16] DONG, D., WEN, B., BOROYEVICH, D., et al. “Analysis of phase-locked loop low-frequency stability in three-phase grid-connected power converters considering impedance interactions”, *IEEE Transactions on Industrial Electronics*, v. 62, n. 1, pp. 310–321, 2014.
- [17] YANG, C., HUANG, L., XIN, H., et al. “Placing grid-forming converters to enhance small signal stability of PLL-integrated power systems”, *IEEE Transactions on Power Systems*, v. 36, n. 4, pp. 3563–3573, 2020.

- [18] RATHNAYAKE, D. B., AKRAMI, M., PHURAILATPAM, C., et al. “Grid Forming Inverter Modeling, Control, and Applications”, *IEEE Access*, 2021.
- [19] ROSSO, R., WANG, X., LISERRE, M., et al. “Grid-forming converters: control approaches, grid-synchronization, and future trends-A review”, *IEEE Open Journal of Industry Applications*, 2021.
- [20] ROSSO, R., CASSOLI, J., BUTICCHI, G., et al. “Robust stability analysis of LCL filter based synchronverter under different grid conditions”, *IEEE Transactions on Power Electronics*, v. 34, n. 6, pp. 5842–5853, 2018.
- [21] ROSSO, R., ENGELKEN, S., LISERRE, M. “Robust stability analysis of synchronverters operating in parallel”, *IEEE Transactions on Power Electronics*, v. 34, n. 11, pp. 11309–11319, 2019.
- [22] LIAO, Y., WANG, X., LIU, F., et al. “Sub-synchronous control interaction in grid-forming VSCs with droop control”. In: *2019 4th IEEE Workshop on the Electronic Grid (eGRID)*, pp. 1–6. IEEE, 2019.
- [23] WANG, X., TAUL, M. G., WU, H., et al. “Grid-synchronization stability of converter-based resources—An overview”, *IEEE Open Journal of Industry Applications*, v. 1, pp. 115–134, 2020.
- [24] HE, J., LI, Y. W. “Generalized closed-loop control schemes with embedded virtual impedances for voltage source converters with LC or LCL filters”, *IEEE Transactions on Power Electronics*, v. 27, n. 4, pp. 1850–1861, 2011.
- [25] WANG, X., LI, Y. W., BLAABJERG, F., et al. “Virtual-impedance-based control for voltage-source and current-source converters”, *IEEE Transactions on Power Electronics*, v. 30, n. 12, pp. 7019–7037, 2014.
- [26] ALVES, F. A., TRICARICO, T. C., DE OLIVEIRA, D. S., et al. “A Procedure to Design Damping Virtual Impedance on Grid-Forming Voltage Source Converters with LCL Filters”, *Journal of Control, Automation and Electrical Systems*, pp. 1–18, 2022.
- [27] ALVES, F. A., COSTA, T. F., LAURINDO, B. M., et al. “Comparative study of different values of inertia for islanded systems”. In: *Congresso Brasileiro de Automática-CBA*, v. 2, 2020.
- [28] ALVES, F. A., COSTA, T. F., LAURINDO, B. M., et al. “Comparative Study of Different Values of Inertia for Islanded Systems with Energy Storage

- Systems”, *Journal of Control, Automation and Electrical Systems*, v. 33, n. 1, pp. 241–254, 2022.
- [29] NEVES, M. S., ALVES, F. A., AREDES, M. A., et al. “A Virtual DC Machine Control Strategy with Nonlinear Behavior to Enhance Power Sharing and Voltage Regulation in DC Microgrids”. In: *2021 IEEE Fourth International Conference on DC Microgrids (ICDCM)*, pp. 1–8. IEEE, 2021.
- [30] TRICARICO, T., COSTA, J. A., ALVES, F. A., et al. “A New Control Solution Using FCS-MPC For a Bidirectional Interleaved Converter Operating as a DC Power-flow Interface”, *Brazilian Journal of Power Electronics*, v. 27, n. 1, pp. 1–10, 2022.
- [31] DE OLIVEIRA, D. D. S., LEAL, G. C. B., DA COSTA, J. A. V., et al. “Ferroresonance and Self-excitation Phenomena in Subsea Power Systems Considering Voltage Control Dynamics and Cable Constructive Parameters”, *Journal of Control, Automation and Electrical Systems*, pp. 1–16, 2022.
- [32] DE OLIVEIRA, D. D. S., DE SOUZA, M. J. A., LEAL, G. C. B., et al. “Probabilistic assessment of the vsc-hvdc contribution in voltage stability applied to a hybrid dc-multi-infeed scenario”. In: *IECON 2020 the 46th annual conference of the IEEE industrial electronics society*, pp. 1684–1691. IEEE, 2020.
- [33] ZHANG, H., XIANG, W., LIN, W., et al. “Grid forming converters in renewable energy sources dominated power grid: control strategy, stability, application, and challenges”, *Journal of Modern Power Systems and Clean Energy*, v. 9, n. 6, pp. 1239–1256, 2021.
- [34] TAYYEBI, A., GROSS, D., ANTA, A., et al. “Frequency stability of synchronous machines and grid-forming power converters”, *IEEE Journal of Emerging and Selected Topics in Power Electronics*, v. 8, n. 2, pp. 1004–1018, 2020.
- [35] ROCABERT, J., LUNA, A., BLAABJERG, F., et al. “Control of power converters in AC microgrids”, *IEEE transactions on power electronics*, v. 27, n. 11, pp. 4734–4749, 2012.
- [36] CHANDORKAR, M. C., DIVAN, D. M., ADAPA, R. “Control of parallel connected inverters in standalone AC supply systems”, *IEEE transactions on industry applications*, v. 29, n. 1, pp. 136–143, 1993.

- [37] DE BRABANDERE, K., BOLSENS, B., VAN DEN KEYBUS, J., et al. “A voltage and frequency droop control method for parallel inverters”, *IEEE Transactions on power electronics*, v. 22, n. 4, pp. 1107–1115, 2007.
- [38] D’ARCO, S., SUUL, J. A. “Virtual synchronous machines—Classification of implementations and analysis of equivalence to droop controllers for microgrids”. In: *2013 IEEE Grenoble Conference*, pp. 1–7. IEEE, 2013.
- [39] AKAGI, H., WATANABE, E. H., AREDES, M. *Instantaneous power theory and applications to power conditioning*. John Wiley & Sons, 2017.
- [40] ENGLER, A. “Applicability of droops in low voltage grids”, *International Journal of Distributed Energy Resources*, v. 1, n. 1, pp. 1–6, 2005.
- [41] VANDOORN, T. L., DE KOONING, J. D., MEERSMAN, B., et al. “Automatic power-sharing modification of P/V droop controllers in low-voltage resistive microgrids”, *IEEE Transactions on Power Delivery*, v. 27, n. 4, pp. 2318–2325, 2012.
- [42] ZHONG, Q.-C., ZENG, Y. “Universal droop control of inverters with different types of output impedance”, *IEEE access*, v. 4, pp. 702–712, 2016.
- [43] BECK, H.-P., HESSE, R. “Virtual synchronous machine”. In: *2007 9th International Conference on Electrical Power Quality and Utilisation*, pp. 1–6. IEEE, 2007.
- [44] CHEN, Y., HESSE, R., TURSCHNER, D., et al. “Comparison of methods for implementing virtual synchronous machine on inverters”. In: *International conference on renewable energies and power quality*, v. 1, pp. 414–424, 2012.
- [45] ZHONG, Q.-C., WEISS, G. “Synchronverters: Inverters that mimic synchronous generators”, *IEEE transactions on industrial electronics*, v. 58, n. 4, pp. 1259–1267, 2010.
- [46] ALVES, F. “ESTUDO DE CONTROLES DE DIVISÃO DE CARGA PARA INVERSORES CONECTADOS EM PARALELO EM MICRORREDE”. Universidade Federal do Rio de Janeiro, 2019.
- [47] REMON, D., CANTARELLAS, A. M., RAKHSHANI, E., et al. “An active power synchronization control loop for grid-connected converters”. In: *2014 IEEE PES General Meeting/ Conference & Exposition*, pp. 1–5. IEEE, 2014.

- [48] RODRIGUEZ, P., CITRO, C., CANDELA, J. I., et al. “Flexible grid connection and islanding of SPC-based PV power converters”, *IEEE Transactions on Industry Applications*, v. 54, n. 3, pp. 2690–2702, 2018.
- [49] ROSSO, R., ENGELKEN, S., LISERRE, M. “A generalized formulation of active power synchronization based control algorithms for grid connected converters”. In: *IECON 2018-44th Annual Conference of the IEEE Industrial Electronics Society*, pp. 883–888. IEEE, 2018.
- [50] LIU, J., MIURA, Y., ISE, T. “Comparison of dynamic characteristics between virtual synchronous generator and droop control in inverter-based distributed generators”, *IEEE Transactions on Power Electronics*, v. 31, n. 5, pp. 3600–3611, 2015.
- [51] YOUNG, H. A., MARIN, V. A., PESCE, C., et al. “Simple finite-control-set model predictive control of grid-forming inverters with LCL filters”, *IEEE Access*, v. 8, pp. 81246–81256, 2020.
- [52] CHHOR, J., LAMMERSMANN, B. “Predictive voltage control for grid-forming power converters with virtual output impedance”. In: *IECON 2021-47th Annual Conference of the IEEE Industrial Electronics Society*, pp. 1–7. IEEE, 2021.
- [53] JOHNSON, B. B., DHOPLÉ, S. V., HAMADEH, A. O., et al. “Synchronization of parallel single-phase inverters with virtual oscillator control”, *IEEE Transactions on Power Electronics*, v. 29, n. 11, pp. 6124–6138, 2013.
- [54] JOHNSON, B. B., DHOPLÉ, S. V., CALE, J. L., et al. “Oscillator-based inverter control for islanded three-phase microgrids”, *IEEE Journal of Photovoltaics*, v. 4, n. 1, pp. 387–395, 2013.
- [55] JOHNSON, B. B., SINHA, M., AINSWORTH, N. G., et al. “Synthesizing virtual oscillators to control islanded inverters”, *IEEE Transactions on Power Electronics*, v. 31, n. 8, pp. 6002–6015, 2015.
- [56] SINHA, M., DÖRFLER, F., JOHNSON, B. B., et al. “Uncovering droop control laws embedded within the nonlinear dynamics of van der pol oscillators”, *IEEE Transactions on Control of Network Systems*, v. 4, n. 2, pp. 347–358, 2015.
- [57] OOI, B.-T., WANG, X. “Voltage angle lock loop control of the boost type PWM converter for HVDC application”, *IEEE Transactions on Power Electronics*, v. 5, n. 2, pp. 229–235, 1990.

- [58] WANG, X., LOH, P. C., BLAABJERG, F. “Stability analysis and controller synthesis for single-loop voltage-controlled VSIs”, *IEEE Transactions on Power Electronics*, v. 32, n. 9, pp. 7394–7404, 2017.
- [59] LOH, P. C., HOLMES, D. G. “Analysis of multiloop control strategies for LC/CL/LCL-filtered voltage-source and current-source inverters”, *IEEE Transactions on Industry Applications*, v. 41, n. 2, pp. 644–654, 2005.
- [60] LI, Y., GU, Y., ZHU, Y., et al. “Impedance circuit model of grid-forming inverter: Visualizing control algorithms as circuit elements”, *IEEE Transactions on Power Electronics*, v. 36, n. 3, pp. 3377–3395, 2020.
- [61] TANG, Y., FANG, J., LI, X., et al. “Reshaping quadrature-axis impedance of three-phase grid-connected converters for low-frequency stability improvement”. In: *2018 International Power Electronics Conference (IPEC-Niigata 2018-ECCE Asia)*, pp. 3910–3915. IEEE, 2018.
- [62] FANG, J., LI, X., LI, H., et al. “Stability improvement for three-phase grid-connected converters through impedance reshaping in quadrature-axis”, *IEEE Transactions on Power Electronics*, v. 33, n. 10, pp. 8365–8375, 2017.
- [63] YANG, D., RUAN, X., WU, H. “Impedance shaping of the grid-connected inverter with LCL filter to improve its adaptability to the weak grid condition”, *IEEE Transactions on Power Electronics*, v. 29, n. 11, pp. 5795–5805, 2014.
- [64] LIN, Z., CHEN, Z., YAJUAN, L., et al. “Phase-reshaping strategy for enhancing grid-connected inverter robustness to grid impedance”, *IET Power Electronics*, v. 11, n. 8, pp. 1434–1443, 2018.
- [65] ZMOOD, D. N., HOLMES, D. G. “Stationary frame current regulation of PWM inverters with zero steady-state error”, *IEEE Transactions on power electronics*, v. 18, n. 3, pp. 814–822, 2003.
- [66] GAO, Z. “Scaling and bandwidth-parameterization based controller tuning”. In: *Proceedings of the American control conference*, v. 6, pp. 4989–4996, 2006.
- [67] PAN-ON, J., SANGTUNGTONG, W. “Design Equation for Directly Computing Two Gains of PR Controller”. In: *2019 IEEE 2nd International Conference on Power and Energy Applications (ICPEA)*, pp. 119–123. IEEE, 2019.

- [68] LASCU, C., ASIMINOAEI, L., BOLDEA, I., et al. “High performance current controller for selective harmonic compensation in active power filters”, *IEEE Transactions on Power electronics*, v. 22, n. 5, pp. 1826–1835, 2007.
- [69] LASCU, C., ASIMINOAEI, L., BOLDEA, I., et al. “Frequency response analysis of current controllers for selective harmonic compensation in active power filters”, *IEEE Transactions on Industrial Electronics*, v. 56, n. 2, pp. 337–347, 2008.
- [70] BERES, R., WANG, X., BLAABJERG, F., et al. “Comparative evaluation of passive damping topologies for parallel grid-connected converters with LCL filters”. In: *2014 International Power Electronics Conference (IPEC-Hiroshima 2014-ECCE ASIA)*, pp. 3320–3327. IEEE, 2014.
- [71] PENA-ALZOLA, R., LISERRE, M., BLAABJERG, F., et al. “Analysis of the passive damping losses in LCL-filter-based grid converters”, *IEEE Transactions on Power Electronics*, v. 28, n. 6, pp. 2642–2646, 2012.
- [72] GABE, I. J., MONTAGNER, V. F., PINHEIRO, H. “Design and implementation of a robust current controller for VSI connected to the grid through an LCL filter”, *IEEE Transactions on Power Electronics*, v. 24, n. 6, pp. 1444–1452, 2009.
- [73] ROCKHILL, A., LISERRE, M., TEODORESCU, R., et al. “Grid-filter design for a multimegawatt medium-voltage voltage-source inverter”, *IEEE Transactions on Industrial Electronics*, v. 58, n. 4, pp. 1205–1217, 2010.
- [74] HAN, Y., YANG, M., LI, H., et al. “Modeling and stability analysis of LCL-type grid-connected inverters: a comprehensive overview”, *IEEE Access*, v. 7, pp. 114975–115001, 2019.
- [75] GOMES, C. C., CUPERTINO, A. F., PEREIRA, H. A. “Damping techniques for grid-connected voltage source converters based on LCL filter: An overview”, *Renewable and Sustainable Energy Reviews*, v. 81, pp. 116–135, 2018.
- [76] PENA-ALZOLA, R., LISERRE, M., BLAABJERG, F., et al. “A self-commissioning notch filter for active damping in a three-phase LCL-filter-based grid-tie converter”, *IEEE Transactions on Power Electronics*, v. 29, n. 12, pp. 6754–6761, 2014.
- [77] DANNEHL, J., LISERRE, M., FUCHS, F. W. “Filter-based active damping of voltage source converters with LCL filter”, *IEEE Transactions on Industrial Electronics*, v. 58, n. 8, pp. 3623–3633, 2010.

- [78] YAO, W., YANG, Y., ZHANG, X., et al. “Design and analysis of robust active damping for LCL filters using digital notch filters”, *IEEE Transactions on Power Electronics*, v. 32, n. 3, pp. 2360–2375, 2016.
- [79] LISERRE, M., DELL’AQUILA, A., BLAABJERG, F. “Genetic algorithm-based design of the active damping for an LCL-filter three-phase active rectifier”, *IEEE Transactions on Power Electronics*, v. 19, n. 1, pp. 76–86, 2004.
- [80] ROLDÁN-PÉREZ, J., BUENO, E. J., PENA-ALZOLA, R., et al. “All-pass-filter-based active damping for VSCs with LCL filters connected to weak grids”, *IEEE Transactions on Power Electronics*, v. 33, n. 11, pp. 9890–9901, 2018.
- [81] LIU, T., LIU, J., LIU, Z., et al. “A study of virtual resistor-based active damping alternatives for LCL resonance in grid-connected voltage source inverters”, *IEEE Transactions on Power Electronics*, v. 35, n. 1, pp. 247–262, 2019.
- [82] GUAN, Y., WANG, Y., XIE, Y., et al. “The dual-current control strategy of grid-connected inverter with LCL filter”, *IEEE Transactions on Power Electronics*, v. 34, n. 6, pp. 5940–5952, 2018.
- [83] SHEN, G., ZHU, X., ZHANG, J., et al. “A new feedback method for PR current control of LCL-filter-based grid-connected inverter”, *IEEE Transactions on Industrial Electronics*, v. 57, n. 6, pp. 2033–2041, 2010.
- [84] HE, N., XU, D., ZHU, Y., et al. “Weighted average current control in a three-phase grid inverter with an LCL filter”, *IEEE Transactions on Power Electronics*, v. 28, n. 6, pp. 2785–2797, 2012.
- [85] WANG, X., BLAABJERG, F., LOH, P. C. “Grid-current-feedback active damping for LCL resonance in grid-connected voltage-source converters”, *IEEE Transactions on Power Electronics*, v. 31, n. 1, pp. 213–223, 2015.
- [86] XU, J., XIE, S., TANG, T. “Active damping-based control for grid-connected LCL-filtered inverter with injected grid current feedback only”, *IEEE Transactions on Industrial Electronics*, v. 61, n. 9, pp. 4746–4758, 2013.
- [87] HE, Y., WANG, X., RUAN, X., et al. “Capacitor-current proportional-integral positive feedback active damping for LCL-type grid-connected inverter to achieve high robustness against grid impedance variation”, *IEEE Transactions on Power Electronics*, v. 34, n. 12, pp. 12423–12436, 2019.

- [88] WANG, X., BLAABJERG, F., LOH, P. C. “Virtual RC damping of LCL-filtered voltage source converters with extended selective harmonic compensation”, *IEEE Transactions on Power Electronics*, v. 30, n. 9, pp. 4726–4737, 2014.
- [89] CHEN, H.-C., CHENG, P.-T., WANG, X., et al. “A passivity-based stability analysis of the active damping technique in the offshore wind farm applications”, *IEEE Transactions on Industry Applications*, v. 54, n. 5, pp. 5074–5082, 2018.
- [90] MALINOWSKI, M., BERNET, S. “A simple voltage sensorless active damping scheme for three-phase PWM converters with an *LCL* filter”, *IEEE Transactions on Industrial Electronics*, v. 55, n. 4, pp. 1876–1880, 2008.
- [91] PEÑA-ALZOLA, R., LISERRE, M., BLAABJERG, F., et al. “Systematic design of the lead-lag network method for active damping in LCL-filter based three phase converters”, *IEEE Transactions on Industrial Informatics*, v. 10, n. 1, pp. 43–52, 2013.
- [92] NIE, C., WANG, Y., LEI, W., et al. “An enhanced control strategy for multiparalleled grid-connected single-phase converters with load harmonic current compensation capability”, *IEEE Transactions on Industrial Electronics*, v. 65, n. 7, pp. 5623–5633, 2017.
- [93] XIN, Z., LOH, P. C., WANG, X., et al. “Highly accurate derivatives for LCL-filtered grid converter with capacitor voltage active damping”, *IEEE Transactions on Power Electronics*, v. 31, n. 5, pp. 3612–3625, 2015.
- [94] LISERRE, M., DELL’AQUILA, A., BLAABJERG, F. “Stability improvements of an LCL-filter based three-phase active rectifier”. In: *2002 IEEE 33rd Annual IEEE Power Electronics Specialists Conference. Proceedings (Cat. No. 02CH37289)*, v. 3, pp. 1195–1201. IEEE, 2002.
- [95] PENA-ALZOLA, R., LISERRE, M., BLAABJERG, F., et al. “LCL-filter design for robust active damping in grid-connected converters”, *IEEE Transactions on Industrial Informatics*, v. 10, n. 4, pp. 2192–2203, 2014.
- [96] DANNEHL, J., FUCHS, F. W., HANSEN, S., et al. “Investigation of active damping approaches for PI-based current control of grid-connected pulse width modulation converters with LCL filters”, *IEEE Transactions on Industry Applications*, v. 46, n. 4, pp. 1509–1517, 2010.

- [97] TWINING, E., HOLMES, D. G. “Grid current regulation of a three-phase voltage source inverter with an LCL input filter”, *IEEE transactions on power electronics*, v. 18, n. 3, pp. 888–895, 2003.
- [98] BAO, C., RUAN, X., WANG, X., et al. “Step-by-step controller design for LCL-type grid-connected inverter with capacitor–current–feedback active-damping”, *IEEE Transactions on Power Electronics*, v. 29, n. 3, pp. 1239–1253, 2013.
- [99] ZHOU, L., ZHOU, X., CHEN, Y., et al. “Inverter-current-feedback resonance-suppression method for LCL-type DG system to reduce resonance-frequency offset and grid-inductance effect”, *IEEE Transactions on Industrial Electronics*, v. 65, n. 9, pp. 7036–7048, 2018.
- [100] HOLMES, D. G., LIPO, T. A., MCGRATH, B. P., et al. “Optimized design of stationary frame three phase AC current regulators”, *IEEE transactions on power electronics*, v. 24, n. 11, pp. 2417–2426, 2009.
- [101] ZOU, C., LIU, B., DUAN, S., et al. “Influence of delay on system stability and delay optimization of grid-connected inverters with LCL filter”, *IEEE Transactions on Industrial Informatics*, v. 10, n. 3, pp. 1775–1784, 2014.
- [102] NUSSBAUMER, T., HELDWEIN, M. L., GONG, G., et al. “Comparison of prediction techniques to compensate time delays caused by digital control of a three-phase buck-type PWM rectifier system”, *IEEE transactions on industrial electronics*, v. 55, n. 2, pp. 791–799, 2008.
- [103] JUDEWICZ, M. G., GONZÁLEZ, S. A., FISCHER, J. R., et al. “Inverter-side current control of grid-connected voltage source inverters with LCL filter based on generalized predictive control”, *IEEE Journal of Emerging and Selected Topics in Power Electronics*, v. 6, n. 4, pp. 1732–1743, 2018.
- [104] BIBIAN, S., JIN, H. “Time delay compensation of digital control for DC switchmode power supplies using prediction techniques”, *IEEE Transactions on power electronics*, v. 15, n. 5, pp. 835–842, 2000.
- [105] WAN, Z., XIONG, J., LEI, J., et al. “Analyze and reduce the impact of sampling delay on LCL converter with capacitor current feedback active damping”. In: *2015 IEEE 11th International Conference on Power Electronics and Drive Systems*, pp. 539–545. IEEE, 2015.
- [106] LI, X., FANG, J., TANG, Y., et al. “Capacitor-voltage feedforward with full delay compensation to improve weak grids adaptability of LCL-filtered grid-

- connected converters for distributed generation systems”, *IEEE Transactions on Power Electronics*, v. 33, n. 1, pp. 749–764, 2017.
- [107] YANG, L., YANG, J. “A robust dual-loop current control method with a delay-compensation control link for LCL-type shunt active power filters”, *IEEE Transactions on Power Electronics*, v. 34, n. 7, pp. 6183–6199, 2018.
- [108] CHEN, C., XIONG, J., WAN, Z., et al. “A time delay compensation method based on area equivalence for active damping of an LCL-type converter”, *IEEE Transactions on Power Electronics*, v. 32, n. 1, pp. 762–772, 2016.
- [109] PAN, D., RUAN, X., BAO, C., et al. “Optimized controller design for LCL-type grid-connected inverter to achieve high robustness against grid-impedance variation”, *IEEE Transactions on Industrial Electronics*, v. 62, n. 3, pp. 1537–1547, 2014.
- [110] QUAN, X. “Improved dynamic response design for proportional resonant control applied to three-phase grid-forming inverter”, *IEEE Transactions on Industrial Electronics*, v. 68, n. 10, pp. 9919–9930, 2020.
- [111] OGATA, K. *Modern control engineering*. Prentice hall, 2010.
- [112] ANEEL. “Procedimentos de Distribuição de Energia Elétrica no Sistema Elétrico Nacional: Módulo 8 – Qualidade da Energia Elétrica”, *Agência Nacional de Energia Elétrica*, 2021.
- [113] KUPERMAN, A. “Proportional-resonant current controllers design based on desired transient performance”, *IEEE Transactions on Power Electronics*, v. 30, n. 10, pp. 5341–5345, 2015.
- [114] HARNEFORS, L., BONGIORNO, M., LUNDBERG, S. “Input-admittance calculation and shaping for controlled voltage-source converters”, *IEEE transactions on industrial electronics*, v. 54, n. 6, pp. 3323–3334, 2007.
- [115] CESPEDES, M., SUN, J. “Impedance modeling and analysis of grid-connected voltage-source converters”, *IEEE Transactions on Power Electronics*, v. 29, n. 3, pp. 1254–1261, 2013.
- [116] WANG, X., BLAABJERG, F. “Harmonic stability in power electronic-based power systems: Concept, modeling, and analysis”, *IEEE Transactions on Smart Grid*, v. 10, n. 3, pp. 2858–2870, 2018.
- [117] LIAO, Y., WANG, X. “Impedance-based stability analysis for interconnected converter systems with open-loop RHP poles”, *IEEE Transactions on Power Electronics*, v. 35, n. 4, pp. 4388–4397, 2019.

- [118] MESSO, T., JOKIPII, J., PUUKKO, J., et al. “Determining the value of DC-link capacitance to ensure stable operation of a three-phase photovoltaic inverter”, *IEEE Transactions on Power Electronics*, v. 29, n. 2, pp. 665–673, 2013.
- [119] ALAWASA, K. M., MOHAMED, Y. A.-R. I., XU, W. “Active mitigation of subsynchronous interactions between PWM voltage-source converters and power networks”, *IEEE Transactions on Power Electronics*, v. 29, n. 1, pp. 121–134, 2013.
- [120] LAZZARIN, T. B., BAUER, G. A., BARBI, I. “A control strategy for parallel operation of single-phase voltage source inverters: analysis, design and experimental results”, *IEEE Transactions on Industrial Electronics*, v. 60, n. 6, pp. 2194–2204, 2012.
- [121] HE, J., LI, Y. W. “Analysis, design, and implementation of virtual impedance for power electronics interfaced distributed generation”, *IEEE Transactions on Industry Applications*, v. 47, n. 6, pp. 2525–2538, 2011.
- [122] TAO, Y., LIU, Q., DENG, Y., et al. “Analysis and mitigation of inverter output impedance impacts for distributed energy resource interface”, *IEEE Transactions on Power Electronics*, v. 30, n. 7, pp. 3563–3576, 2014.
- [123] AKAGI, H., FUJITA, H., WADA, K. “A shunt active filter based on voltage detection for harmonic termination of a radial power distribution line”, *IEEE Transactions on Industry Applications*, v. 35, n. 3, pp. 638–645, 1999.
- [124] WANG, X., BLAABJERG, F., CHEN, Z. “Synthesis of variable harmonic impedance in inverter-interfaced distributed generation unit for harmonic damping throughout a distribution network”, *IEEE transactions on Industry Applications*, v. 48, n. 4, pp. 1407–1417, 2012.
- [125] WANG, X., BLAABJERG, F., CHEN, Z. “Autonomous control of inverter-interfaced distributed generation units for harmonic current filtering and resonance damping in an islanded microgrid”, *IEEE Transactions on Industry Applications*, v. 50, n. 1, pp. 452–461, 2013.
- [126] BORUP, U., BLAABJERG, F., ENJETI, P. N. “Sharing of nonlinear load in parallel-connected three-phase converters”, *IEEE Transactions on Industry Applications*, v. 37, n. 6, pp. 1817–1823, 2001.

- [127] DE, D., RAMANARAYANAN, V. “Decentralized parallel operation of inverters sharing unbalanced and nonlinear loads”, *IEEE Transactions on Power Electronics*, v. 25, n. 12, pp. 3015–3025, 2010.
- [128] CHENG, P.-T., CHEN, C.-A., LEE, T.-L., et al. “A cooperative imbalance compensation method for distributed-generation interface converters”, *IEEE Transactions on Industry Applications*, v. 45, n. 2, pp. 805–815, 2009.
- [129] WANG, X., BLAABJERG, F., CHEN, Z. “An improved design of virtual output impedance loop for droop-controlled parallel three-phase voltage source inverters”. In: *2012 IEEE Energy Conversion Congress and Exposition (ECCE)*, pp. 2466–2473. IEEE, 2012.
- [130] PAQUETTE, A. D., DIVAN, D. M. “Virtual impedance current limiting for inverters in microgrids with synchronous generators”, *IEEE Transactions on Industry Applications*, v. 51, n. 2, pp. 1630–1638, 2014.
- [131] VILATHGAMUWA, D. M., LOH, P. C., LI, Y. “Protection of microgrids during utility voltage sags”, *IEEE Transactions on Industrial Electronics*, v. 53, n. 5, pp. 1427–1436, 2006.
- [132] QORIA, T., GRUSON, F., COLAS, F., et al. “Current limiting algorithms and transient stability analysis of grid-forming VSCs”, *Electric Power Systems Research*, v. 189, pp. 106726, 2020.
- [133] GUAN, Y., GUERRERO, J. M., ZHAO, X., et al. “A new way of controlling parallel-connected inverters by using synchronous-reference-frame virtual impedance loop—Part I: Control principle”, *IEEE Transactions on Power Electronics*, v. 31, n. 6, pp. 4576–4593, 2015.
- [134] SUUL, J. A., MOLINAS, M., RODRÍGUEZ, P. “Exploring the range of impedance conditioning by virtual inductance for grid connected voltage source converters”. In: *2012 3rd IEEE PES Innovative Smart Grid Technologies Europe (ISGT Europe)*, pp. 1–9. IEEE, 2012.
- [135] MAHMOOD, H., MICHAELSON, D., JIANG, J. “Accurate reactive power sharing in an islanded microgrid using adaptive virtual impedances”, *IEEE Transactions on Power Electronics*, v. 30, n. 3, pp. 1605–1617, 2014.
- [136] GUERRERO, J. M., DE VICUNA, L. G., MATAS, J., et al. “Output impedance design of parallel-connected UPS inverters with wireless load-sharing control”, *IEEE Transactions on industrial electronics*, v. 52, n. 4, pp. 1126–1135, 2005.

- [137] HOU, G., XING, F., YANG, Y., et al. “Virtual negative impedance droop method for parallel inverters in microgrids”. In: *2015 IEEE 10th Conference on Industrial Electronics and Applications (ICIEA)*, pp. 1009–1013. IEEE, 2015.
- [138] FUNATO, H., KAWAMURA, A., KAMIYAMA, K. “Realization of negative inductance using variable active-passive reactance (VAPAR)”, *IEEE transactions on power electronics*, v. 12, n. 4, pp. 589–596, 1997.
- [139] DRANGA, O., FUNATO, H., OGASAWARA, S., et al. “Investigating stability of power configuration including virtual negative inductance”. In: *2004 IEEE 35th Annual Power Electronics Specialists Conference (IEEE Cat. No. 04CH37551)*, v. 4, pp. 2703–2707. IEEE, 2004.
- [140] HE, Y., LAI, C.-T., CHUNG, S.-H., et al. “Use of series negative impedance to cancel the effect of equivalent grid impedance on the grid-connected inverter stability in the DPGS”. In: *2018 IEEE Applied Power Electronics Conference and Exposition (APEC)*, pp. 2368–2373. IEEE, 2018.
- [141] HARNEFORS, L. “Modeling of three-phase dynamic systems using complex transfer functions and transfer matrices”, *IEEE Transactions on Industrial Electronics*, v. 54, n. 4, pp. 2239–2248, 2007.
- [142] BRIZ, F., DEGNER, M. W., LORENZ, R. D. “Analysis and design of current regulators using complex vectors”, *IEEE Transactions on Industry Applications*, v. 36, n. 3, pp. 817–825, 2000.

Appendix A

Bode Comparison for all of Outer Virtual Impedance

Figures A.1, A.2 and A.3 depict the comparison of the Bode diagrams for PR-Analytical, PR-Gao and VPI controllers with all the 27 calculated H_{ext} values. Color blue is for the lowest value, and as it turns red it goes to the biggest values. In all cases, as the value of H_{ext} is increased, the lower the sensitivity of the converter at low frequencies, since there is no difference at high frequencies.

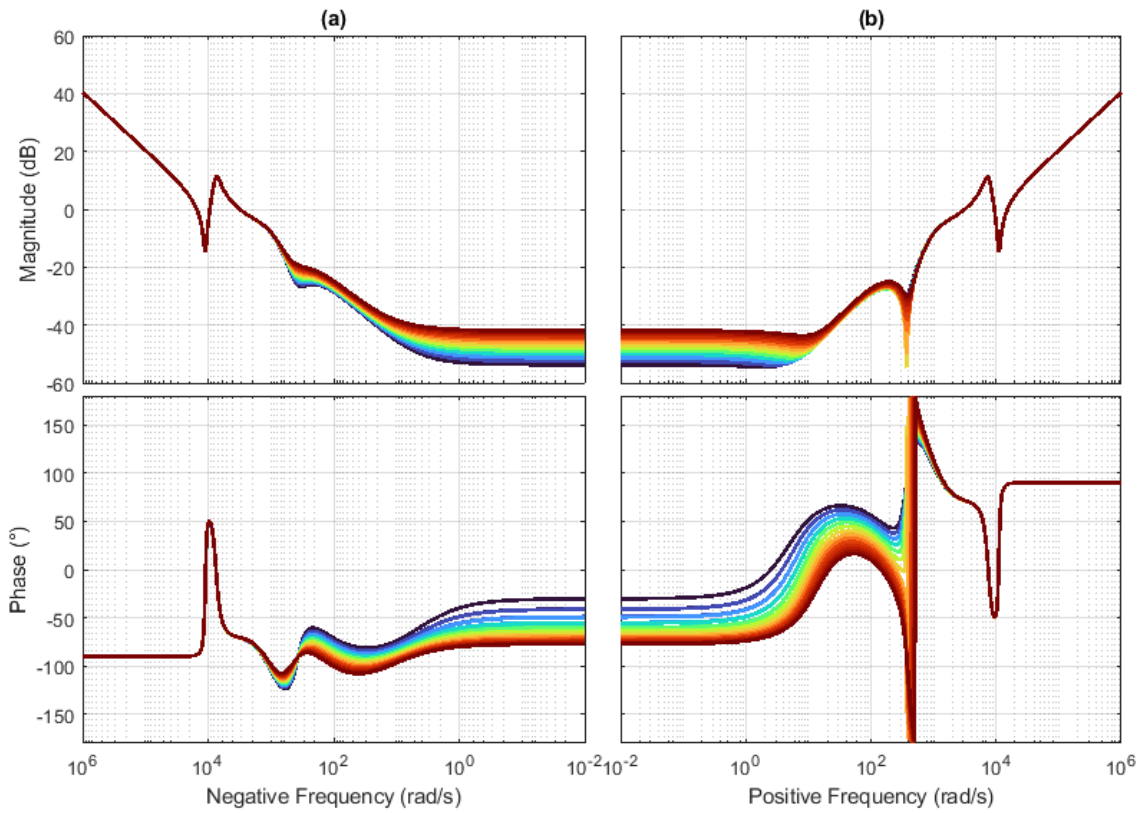


Figure A.1: Bode plot of the $Z_{out}(s)$ for the 27 calculated values of $R_v + j\omega L_v$ with PR-Analytical controller. The blue color means the minimum Z_v , while the red color means the maximum $|Z_v|$ value.

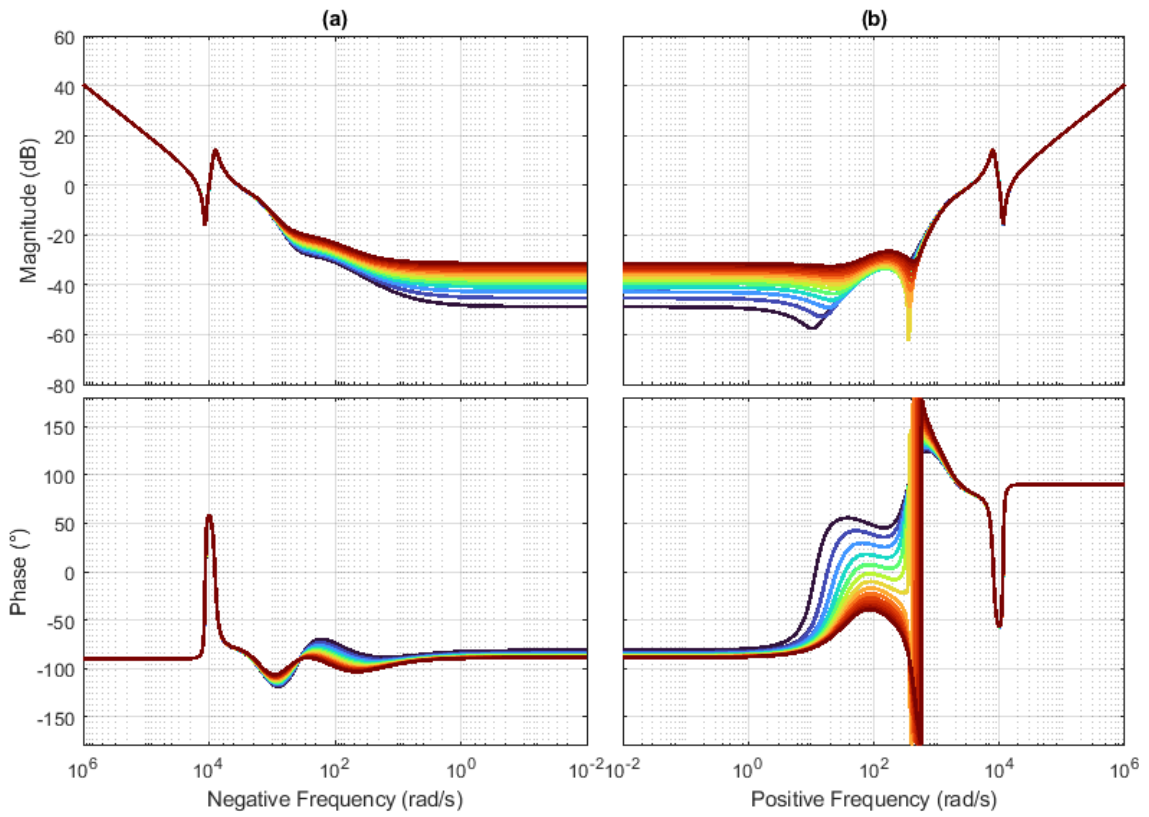


Figure A.2: Bode plot of the $Z_{out}(s)$ for the 27 calculated values of $R_v + j\omega L_v$ with PR-Gao controller. The blue color means the minimum Z_v , while the red color means the maximum $|Z_v|$ value.

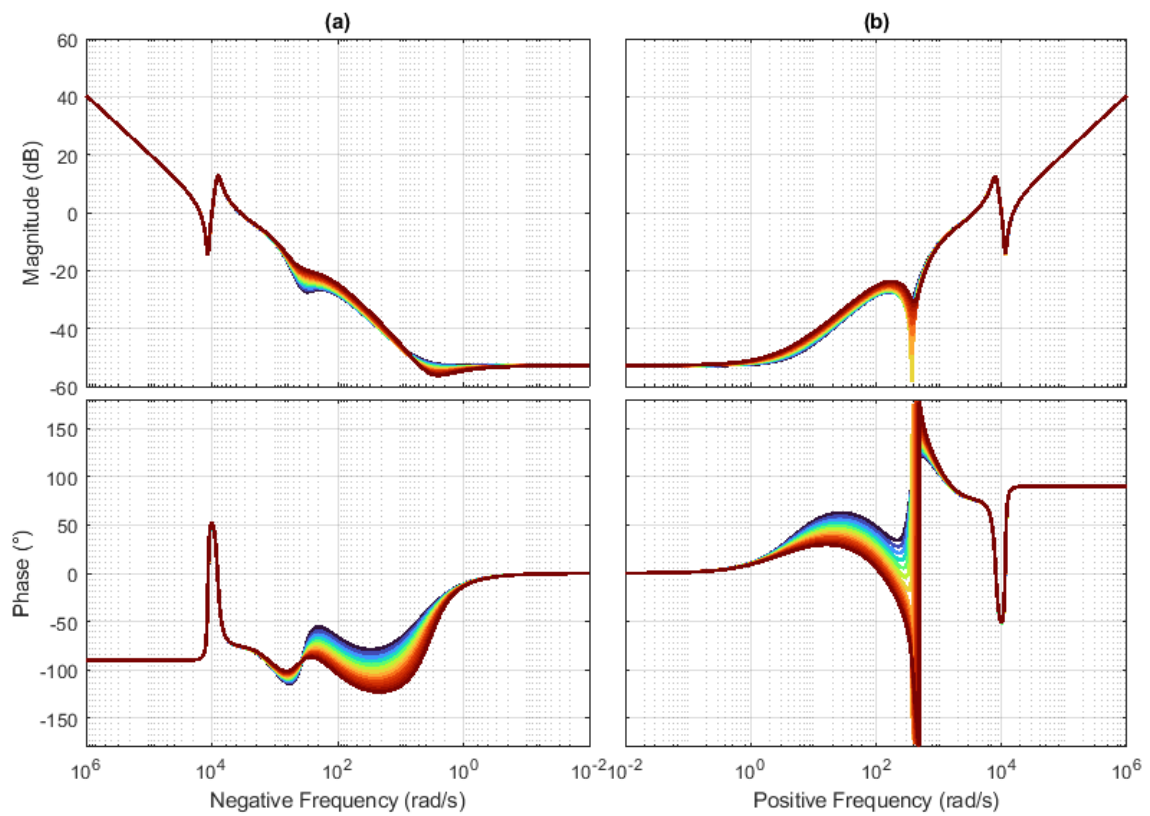


Figure A.3: Bode plot of the $Z_{out}(s)$ for the 27 calculated values of $R_v + j\omega L_v$ with VPI controller. The blue color means the minimum Z_v , while the red color means the maximum $|Z_v|$ value.